HELLENIC REPUBLIC
National and Kapodistrian
University of Athens

NATIONAL AND KAPODISTRIAN UNIVERSITY OF ATHENS

SCHOOL OF SCIENCES

DEPARTMENT OF CHEMISTRY

PhD THESIS

Studies of Peripheral Heavy-ion Reactions with the MAGNEX Spectrometer for the Production of Neutron-rich Isotopes

STERGIOS KOULOURIS

CHEMIST

ATHENS

MARCH 2025

PhD Thesis

Studies of Peripheral Heavy-ion Reactions with the MAGNEX Spectrometer for the Production of Neutron-rich Isotopes

STERGIOS KOULOURIS

R.No: 2014

SUPERVISOR:

Georgios A. Souliotis, Professor, National and Kapodistrian University of Athens

THREE-MEMBER SUPERVISORY COMMITTEE:

Georgios A. Souliotis, Professor, National and Kapodistrian University of Athens

Francesco Cappuzello, Professor, University of Catania

Martin Veselsky, Principal Investigator, Czech Technical University

SEVEN-MEMBER EXAMINATION COMMITTEE

Georgios A. Souliotis, Professor, National and Kapodistrian University of Athens

Francesco Cappuzello, Professor, University of Catania Francesco Cappuzello

Martin Veselsky, Principal Investigator, Czech Technical University

Efstathios Stiliaris, Professor, National and Kapodistrian University of Athens

Andreas Koutselos, Professor, National and Kapodistrian University of Athens

Demeter Tzeli, Associate Professor, National and Kapodistrian University of Athens

Anthoula Papageorgiou, Assistant Professor, National and Kapodistrian University of Athens

EXAMINATION DATE 26/02/2025

Abstract

Peripheral reactions of medium-mass nuclei in the Fermi energy regime (10-30 MeV/nucleon) offer a promising pathway for producing exotic neutron-rich isotopes and probing intricate reaction mechanisms. The work of this thesis constitutes a systematic study of peripheral reactions of medium-mass nuclei in the Fermi energy regime, focusing on the reaction of ^{70}Zn (15 MeV/nucleon) + ^{64}Ni using the MAGNEX spectrometer. MAGNEX through its advanced ray-reconstruction methods allowed for the precise determination of ejectiles with respect to the atomic number Z, the mass number A, the momentum per nucleon p/A and the reaction angle θ_{lab}. The experimental p/A, angular, production cross sections, and excitation energy distributions for several multinucleon transfer channels were extracted and studied in detail, along with comparisons to theoretical models and kinematic calculations. This work indicated the dominance of direct reaction mechanisms at low excitation energy (below about 20 MeV) and the appearance of more complicated processes (beyond independent nucleon exchange) at higher excitation energy. Comparative analyses with the DIT, CoMD, and GEMINI models indicated an overall satisfactory description and underscored their limitations in certain reaction channels, highlighting the need for further developments and the integration of direct reaction codes in the context of this research direction.

This work not only deepens our understanding of peripheral heavy-ion reactions, but also outlines the pivotal role of the MAGNEX magnetic spectrometer in modern nuclear research. Its state-of-the-art design and high-resolution capabilities pave the way for future studies aimed at optimizing the production of exotic nuclei and exploring the underlying dynamics of nuclear reactions.

SUBJECT AREA: Nuclear Physics
KEYWORDS: Heavy Ion Reactions, Large Acceptance Spectrometer, Neutron Rich Isotopes, Multinucleon Transfer, Momentum and Angular Distributions

Περίληψη

Οι περιφερειακές αντιδράσεις πυρήνων μέσης μάζας στην περιοχή ενεργειών Fermi (10-30 MeV/νουκλεόνιο) προσφέρουν μια υποσχόμενη οδό για την παραγωγή εξωτικών ισοτόπων πλουσίων σε νετρόνια και τη διερεύνηση πολύπλοκων μηχανισμών αντίδρασης. Η διατριβή αποτελεί μια συστηματική μελέτη των περιφερειακών αντιδράσεων πυρήνων μέσης μάζας στην περιοχή ενεργειών Fermi, εστιάζοντας στην αντίδραση ^{70}Zn (15 MeV/nucleon) + ^{64}Ni χρησιμοποιώντας το φασματόμετρο MAGNEX. Το MAGNEX, μέσω προηγμένων μεθόδων ανακατασκευής τροχιών, επέτρεψε τον ακριβή προσδιορισμό των θραυσμάτων ως προς τον ατομικό αριθμό Z, τον μαζικό αριθμό A, την ορμή ανά νουκλεόνιο p/A και τη γωνία θ_{lab}. Από τα πειραματικά δεδομένα, εξήχθησαν και μελετήθηκαν σε βάθος οι κατανομές της p/A, οι γωνιακές κατανομές, οι ενεργές διατομές παραγωγής και οι κατανομές της ενέργειας διεγέρσεως για διάφορα κανάλια πολλαπλής μεταφοράς νουκλεονίων, σε συνδυασμό με θεωρητικούς υπολογισμούς και κινηματική ανάλυση. Αυτή η εργασία ανέδειξε την κυριαρχία των άμεσων μηχανισμών αντίδρασης σε χαμηλές ενέργειες διεγέρσεως (κάτω από περίπου 20 MeV), ενώ σε υψηλότερες ενέργειες διεγέρσεως παρατηρήθηκαν πιο σύνθετες διαδικασίες πέραν της ανεξάρτητης ανταλλαγής νουκλεονίων. Οι συγκριτικές αναλύσεις με τα μοντέλα DIT, CoMD και GEMINI ανέδειξαν ικανοποιητική περιγραφή αλλά και περιορισμούς τους σε ορισμένα κανάλια αντίδρασης, υπογραμμίζοντας την ανάγκη περαιτέρω ανάπτυξης των μοντέλων και ενσωμάτωσης κωδίκων άμεσων αντιδράσεων στο πλαίσιο αυτής της ερευνητικής κατεύθυνσης.

Αυτή η εργασία δεν εμβαθύνει μόνο στην κατανόηση των περιφερειακών αντιδράσεων βαρέων ιόντων, αλλά επίσης αναδεικνύει τον καθοριστικό ρόλο του φασματόμετρου MAGNEX στη σύγχρονη πυρηνική έρευνα. Ο πρωτοποριακός του σχεδιασμός και η υψηλή ανάλυση που προσφέρει ανοίγουν νέες προοπτικές για μελλοντικές μελέτες που στοχεύουν στη βελτιστοποίηση της παραγωγής εξωτικών πυρήνων και στη διερεύνηση της δυναμικής των πυρηνικών αντιδράσεων.

ΘΕΜΑΤΙΚΗ ΠΕΡΙΟΧΗ: Πυρηνική Φυσική

ΛΕΞΕΙΣ ΚΛΕΙΔΙΑ: Αντιδράσεις Βαρέων Ιόντων, Φασματόμετρο Μεγάλης Αποδοχής, Ισότοπα Πλούσια σε Νετρόνια, Πολλαπλή Μεταφορά Νουκλεονίων, Γωνιακές Κατανομές και Κατανομές Ορμής

Acknowledgments

The journey through academia and the pursuit of the PhD is one of growth, perseverance, and transformation. More than just research and scholarship, it demands resilience—balancing intellectual challenges with professional commitments, continuously adapting, and pushing forward. Beyond the academic milestones, the greatest rewards are not just degrees or titles. The true value emerges in the wisdom gained, the refinement of critical thinking, and the personal evolution that comes with every challenge. The future holds endless possibilities, and one thing remains certain: the knowledge acquired, the insights gained, and the mindset shaped through this journey are lasting achievements that no one can take away. That is the true measure of success.

Η σκέψη είναι φως· όποιος την κρατά αναμμένη δε χάνεται ποτέ στο σκοτάδι.
Thought is light; whoever keeps it lit is never lost in darkness.

With that in mind, I would like to express my deepest gratitude to those who have supported me throughout this journey. My profound thanks go to my parents, Ioannis and Olympia, for their unwavering support, endless patience, and unconditional love. Their belief in me, even in the most difficult moments, gave me the strength to keep moving forward. Their presence was not only reassuring, but also a constant pillar of encouragement and resilience.

I also extend my heartfelt thanks to my brother, Konstantinos, whose support has been constant. His strength, understanding, and steady presence provided reassurance at every step. Alongside him, Melina has also been a trusted companion throughout this journey, reminding me that no challenge is faced alone.

At the heart of my family, a guiding force throughout this journey has been my beloved Anthi. She is a source of growth, a true embodiment of love—one that runs deep, revealing itself not just in words, but in the kindness and actions that truly define it. A love that doesn't just uplift but inspires—to become a better person, not by expectation, but by encouraging one to be the person they truly wish to be. She is a beacon of light, offering unwavering support and quiet strength, always keeping me on the right path. When I found myself caught in hesitation and uncertainty, questioning my own course like Stepan Trofimovich Verkhovensky, she was there—understanding, and unshaken.

My sincere gratitude goes to my advisor, Professor Georgios A. Souliotis, who has been a guiding presence in my academic journey since my undergraduate thesis in 2018. From my BSc to my MSc and ultimately through this PhD, he has been more than an advisor—a mentor, a quiet force, and a relentless pursuer of knowledge. A man who works tirelessly, driven by the desire to spark minds and create opportunities, he has continuously supported me, providing insights, expertise, and the direction needed to navigate and complete this journey. His dedication to his students and his field has been both inspiring and transformative.

I am grateful to Professor Pakou, whose expertise and guidance have been an enduring source of inspiration. Her advice and support not only strengthened this thesis but also pushed me to grow and reach my fullest potential.

I also extend my sincere thanks to the MAGNEX group, and in particular to Professor Cappuzzello, for the invaluable opportunity to work with a state-of-the-art spectrometer such as MAGNEX and to actively participate in an experiment—an experience that significantly enriched my research journey.

Finally, my heartfelt appreciation goes to my labmates of our Nuclear Chemistry Group, each of whom has been a companion on this path. A special mention to Olga, whose presence and camaraderie have made this journey even more meaningful. The bonds formed in the lab will remain far beyond this thesis—lasting connections built through shared challenges and aspirations.

Contents

List of Figures

List of Tables

Chapter 1
Introduction

Nuclear physics, as an independent field of science, was established in the dusk of the 19th century and more specifically in 1896 with the discovery of radioactivity by Henri Becquerel. This observation, along with other significant events of the 20th century, such as the identification of the electron by J.J. Thomson the very next year, the development of quantum theory in the 1920s, the discovery of the neutron in 1932 by Chadwick and the semi-empirical Bethe-Weizsacker formula in 1935, lead this nascent field into a remarkable flourishing. This interdisciplinary field of science, widely considered today as one of the most important for modern basic research, is in an abiding search for answers to questions that concern nuclear structure, cosmology, astrophysics, the synthesis of chemical elements, as well as the production of energy. An impressive achievement has been the synthesis, identification and study of the properties of about one half of the theoretically estimated 7000 bound nuclei. Over the last 85 years, the number of known nuclides increased by more than a factor of ten, resulting in ≤ 3500 presently known isotopes of 118 elements, with the exact number being 3352 according to a recent contribution [1]. The advent of novel reaction types along with the development of powerful accelerators and experimental techniques for separation and identification of reaction products has led to this considerable progress. Model predictions indicate that still about 4000 further nuclides are waiting for their discovery [2, 3]. The vastest unexplored territory is located on the neutron-rich side in the upper half of the chart of nuclides. For the last few decades, fragmentation, fission, and fusion reactions have been the traditional approaches to produce exotic nuclei in the laboratory [4, 5, 6, 7]. In fact, the capabilities of these processes have effectively determined the present limits of the nuclide chart. The minimum accessible cross-sections currently reach approximately 1 pb for each of the three types of reactions, based on the current

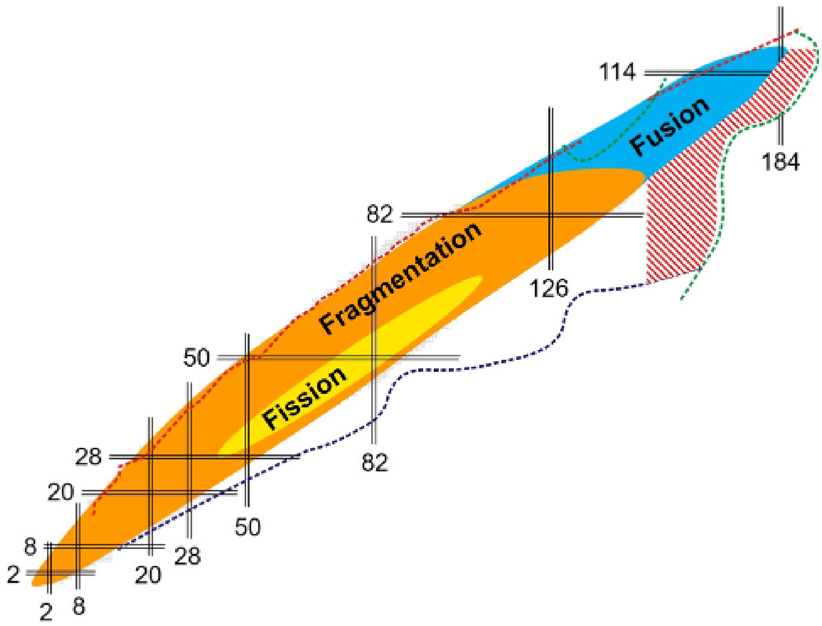

Figure 1.1: This representation of the chart of nuclides illustrates the typical regions where the conventional routes of fusion, fission and fragmentation contribute. The blank area corresponds to neutron-rich nuclides that have not been discovered yet, while the red-white hatched region remains inaccessible through standard reaction mechanisms. [2].

beam intensities and target thicknesses suitable for these processes. Expanding the nuclide chart could be facilitated by increasing beam intensities. Emerging advanced facilities worldwide aim to provide beam currents that are 10 to 100 times higher, targeting the production of nuclei at sub-picobarn cross-sections [2]. The access to these nuclei is presently limited by available beam intensities and/or the lack of appropriate pathways for their production and identification. The latter concerns particularly the production of new neutron-rich isotopes of transuranium and superheavy elements, as well as neutron-rich nuclei below Pb, which are expected to participate in the astrophysical r-process.

The r-process, or rapid neutron capture process, is responsible for half of the abundance of the nuclides heavier than iron [8]. According to the r-process canonical model (CAR, Canonical r-process model) [9], events characterized by high density or flow of neutrons ($N_n \geq 10^{20} neutrons/cm^3$), high temperatures ($T \geq 10^9 K$) and especially short times of irradiation with neutrons (of the order of a few seconds) are capable of justifying the abundance of r-nuclides in the solar system. However, these conditions imply the existence of nuclei deep enough in the neutron-rich side of the valley of nuclear stability, where the typical neutron separation energies are of the order of $2-3\ MeV$ [10]. These conditions are met by astrophysical events such as supernova explosions and neutron star mergers [11]. The nuclei produced by the r-process in these events depend on the composition of material ejected by the merger [12] and the properties of the progenitor neutron stars, including their equation of state [13].

In general, nuclear fusion reactions constitute the main energy source during stellar hydrostatic burning which allow the stars' long life-times of millions to billions of years. While gravity serves as the primary energy source in explosive stellar events such as supernovae or neutron star mergers, nuclear reactions, particularly those involving short-lived nuclides, play a crucial role in shaping the dynamics of these events and in the formation of elements throughout the Universe [14]. One of the main challenges of the research community is determining the rate at which nuclear reactions occur in these environments. During hydrostatic burning, the stellar temperature is much smaller than the Coulomb barrier of the fusing nuclei. This makes it usually impossible to determine the cross sections at the most effective energies in stars in the laboratory. As a result, laboratory data obtained at higher energies need to be extrapolated. Studying the properties of short-lived nuclides requires their production at Radioactive Ion Beam (RIB) facilities. This capability has significantly advanced our astrophysical understanding in recent years. Additionally, nuclear reaction rates are often altered in the extreme conditions of stellar environments, such as high temperatures and densities. These changes necessitate theoretical modeling, which has also made remarkable progress recently, driven by improved computational power and the development of innovative theoretical methods [15].

Due to the aforementioned extreme conditions prevailing in these astrophysical events, high energy γ-ray photons are produced which are responsible for the so-called photodisintegration. It is a process where nuclei emit particles such as neutrons due to their irradiation by these high-energy photons. During the r-process, starting from a relatively light nucleus in the region of Fe, rapid neutron capture takes place, leading to nuclei with neutron excess. The process stops when the produced nucleus is rather short-lived that it undergoes β-decay before it can capture further neutrons. This is the last phase of the process, the so-called freeze-out.

For the last few decades, fragmentation, fission and fusion reactions have been the traditional approaches to produce such exotic nuclei in the laboratory [4, 2, 5, 6]. The efficient production of neutron-rich nuclides constitutes a central issue in current and future facilities worldwide. Towards this direction, the development of modern magnetic spectrometers with large acceptance in momentum and solid angle has been pivotal. Examples of such devices are the following: PRISMA at INFN/LNL [16, 17], VAMOS at GANIL [18, 19, 20], and MAGNEX at INFL/LNS [21, 22, 23].

To move further toward neutron-rich nuclides, along with proton-stripping in the context of fragmentation, it is necessary to pick up neutrons from the target nucleus. The increase of beam intensities is a main goal in accelerator laboratories worldwide, but to reach new neutron-rich nuclei, also new ways for their production are required. Two main approaches include the application of multinucleon transfer (MNT) reactions and deep-inelastic reactions between heavy ions at lower energies, namely near and above the Coulomb barrier, as well as with the use of radioactive ion beams (RIBs) [5, 24].

The MNT reactions are characterized by the sequential exchange of nucleons between the projectile and the target and have been recently extensively used to access neutron-rich nuclei [25, 26, 27, 28, 29, 30, 31]. Concomitantly, multinucleon transfer reactions have been used to study the reaction mechanisms that lead to the production of these exotic nuclei (e.g., [32, 33]). Thus, one can follow the evolution of the mechanism from quasielastic and direct processes to deep inelastic collisions characterized by high energy dissipation. We note that quasielastic processes include possible nucleon-pair transfer and thus, may elucidate the nucleon-nucleon correlations at energies around the Coulomb barrier [34, 35].

Nuclear reactions, in parallel with chemical reactions, can occur via different reaction mechanisms. The nature of these mechanisms depends on two key parameters of the reaction: the kinetic energy of the projectile and the impact parameter of the collision. It is therefore necessary to follow a brief categorization of the nuclear reactions based on these two parameters [36].

Nuclear reactions can be divided into three main categories, regarding beam energy, in the following: low energy reactions (<20 MeV/nucleon), intermediate energy (about 20-200 MeV/nucleon) and high energy (>200 MeV/nucleon). Based on the impact parameter, which is a measure of the closeness of the two participants of the nuclear reaction, the reactions are distinguished as follows:

1. Distant Reactions: This category concerns Rutherford scattering and inelastic Coulomb scattering.

2. Peripheral/Grazing Reactions: In the field of low-energy reactions, direct nucleon transfer takes place and/or incomplete fusion. In intermediate energies, projectile fragmentation and/or multinucleon transfer mostly dominate this energy regime. When the overlap between the projectile and target is very large, further dissipative events occur, such as deep inelastic collisions. In deep inelastic scattering, the colliding nuclei touch, partially amalgamate, exchange substantial amounts of energy and mass, rotate as a partially fused complex, and then reseparate under the influence of their mutual Coulomb repulsion before forming a compound nucleus.

3. Central Reactions: At low energies, head-on collisions lead to fusion of the reacting nuclei, which can lead to the formation of a compound nucleus or a "quasi-fusion" event in which there is substantial mass and energy exchange between the projectile and target nuclei without the "true amnesia" characteristic of compound nucleus formation [37].

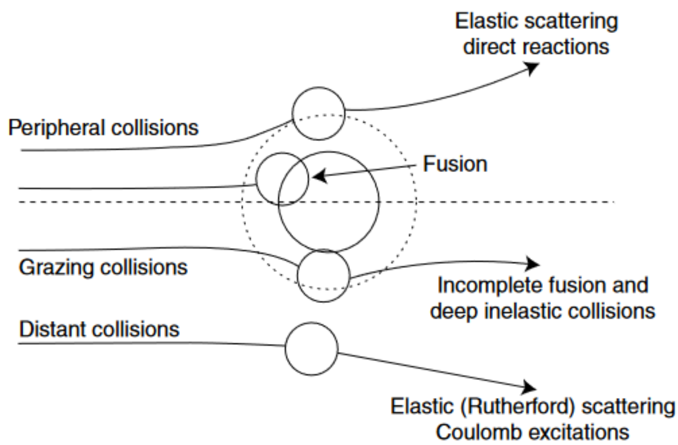

Figure 1.2: Schematic representation of the various reaction types based upon impact parameter [36].

Multinucleon transfer (MNT) occurs in deep inelastic binary reactions at energies around the Coulomb barrier [38, 39]. The first step of multinucleon trarnsfer reactions is the formation of a dinuclear system (DNS) after the capture of projectile and target nucleus due to the nuclear force [38, 40]. After capture, the DNS is trapped in a minimum of the nucleus-nucleus potential, followed by an exchange of mass (charge) and energy between the reaction partners. The livetimes of such dinuclear systems are typically on the order of 10^{-21}–$10^{-20}s$ and depend on several parameters like the atomic number (Z), mass number (A), isospin asymmetry (N/Z), excitation energy or angular momentum of the DNS.

Figure 1.3: Scheme depicting the formation and interaction of the projectile-target dinuclear system [38]. During the interaction, the dinuclear system evolves by continuous redistribution of nucleons, excitation energy and angular momentum between the nuclei before it finally decays.

If the dinuclear system successfully overcomes the fusion barrier, it leads into a Compound Nucleus (CN), achieving full statistical equilibrium. The CN releases its excess energy by emitting nucleons, gamma rays, or by undergoing fission. Alternatively, the DNS may decay prior to CN formation (Quasi-Fission event, QF). Before decay, extensive exchange of neutrons and protons between nuclei occurs, resulting in a variety of reaction products that differ from the original projectile and target nuclei. The excitation energy of the interacting dinuclear system is distributed between the resulting Projectile-Like and Target-Like nuclei. In collisions with i.e. non-zero impact parameter, the DNS can also rotate about its center of mass. This exact rotation can explain the broad angular distributions of the reaction products. The formation of the dinuclear system is usually accompanied by strong dissipation of kinetic energy which is mainly transformed into internal excitation of the system [2]. Upon scission of the dinuclear system, the initially excited primary fragments are emitted, which subsequently de-excite through mostly nucleon and/or γ-ray emission. The final products in their ground state are called secondary fragments.

Along the lines of other concurrent studies as referenced above, our research group has investigated heavy-ion peripheral collisions at energies of $15-25$ MeV/nucleon in order to access nuclides with high neutron excess. Initially, these studies involved 25 MeV/nucleon ^{86}Kr-induced reactions [41, 42, 43, 44] and, subsequently, 15 MeV/nucleon ^{86}Kr-induced [45, 46, 47] and ^{40}Ar-induced reactions [48, 49]. The aforementioned experiments were performed with the MARS recoil separator [50] at the Cyclotron Institute of Texas A&M University. These studies indicated the limitations of a 0-degree separator to access the very neutron-rich fragments produced at angles around the grazing angle. Thus, for efficient collection and study of these fragments, the use of a large acceptance spectrometer is indispensable, as in the case of reactions near the Coulomb barrier.

In the energy range of $15-25$ MeV/nucleon, the velocities of the ejectiles are higher and the angular distributions are narrower, compared to the Coulomb barrier reactions, leading to efficient collection and identification. Moreover, from a nuclear dynamics point of view, this energy regime differs from the regime near and above the Coulomb barrier, where a broad range of studies have already been performed and vividly continue. In the Fermi energy regime, the velocities of the reaction partners become comparable to the nucleon Fermi velocities, and the interaction time is shorter. This results in partial restriction of available phase space for nucleon transfer that takes place in this regime [51, 52], compared to the Coulomb barrier reactions and implies the evolution of the reaction mechanism favoring faster and/or more dissipative dynamical processes. Guided by these observations, we initiated a project to produce, identify, and measure the distributions of projectile-like fragments with the MAGNEX large-acceptance spectrometer at INFN-LNS from the reaction of ^{70}Zn+^{64}Ni at 15 MeV/nucleon. We note that the design of MAGNEX is optimized for charged particle spectroscopy, aiming at good energy and angular resolution and the ability to measure absolute cross sections for rare channels of interest [21, 22]. In the present study, we relied on the performance of MAGNEX for reactions involving medium-mass heavy ions where the Z resolution appeared limited. As presented in a recent contribution [53], a detailed procedure to reconstruct the atomic number Z of the ejectiles along with their ionic charge states employing measurements of the energy loss, residual energy, and time of flight has been developed. This identification procedure will be thoroughly presented within a following section of this dissertation. Subsequently, the momentum and angular distributions of the ejectiles, and their production cross sections were obtained. These experimental results alongside comparisons to theoretical calculations and will be thoroughly presented along the lines of this thesis.

This work constitutes one of the very few high-resolution mass-spectrometric studies in the energy range of $15-25$ MeV/nucleon, providing complete characterization of medium-mass ejectiles in terms of Z, A, velocity, and angle. A similar mass-spectrometric study in this energy range, presented in [54, 55, 56], concerned ejectiles from the reaction of 18 MeV/nucleon ^{86}Kr with ^{208}Pb. We expect that the complete interpretation of the present data, along with detailed theoretical calculations and comparisons with previous work, will shed light on the evolution of the reaction mechanisms. Thus, our study will provide a bridge between the detailed studies of multinucleon transfer near and above the Coulomb barrier [25, 26], and the large body of high-energy (fragmentation) reactions characterized by an abrasion-ablation mechanism [4].

The present work is organized as follows: In Chapter 2, a description of the experimental setup and the measurements are presented. In Chapter 3, the data analysis is described with emphasis on the identification of projectile-like fragments and extraction of their distributions. In Chapter 4, a description of the theoretical model framework is presented. Two dynamical models were used: the phenomenological deep-inelastic transfer (DIT) model and the microscopic constrained molecular dynamics model (CoMD). In Chapter 5, the results on experimental distributions with emphasis on the neutron-rich nuclides are discussed along with comparisons to calculations. Finally, in Chapter 6, a discussion and conclusions are given.

Furthermore, we explore in Appendix A the supplementary reaction of ^{70}Zn with ^{27}Al at 15 MeV/nucleon, offering insights that complement the main reaction studied in this work, namely ^{70}Zn (15 MeV/nucleon)+^{64}Ni. While in Appendix B, we present additional material for the Zn + Ni reaction, including detailed momentum and angular distributions for various reaction channels, which provide a broader context for the results discussed in the main chapters.

Chapter 2
Experimental Setup

2.1 Introduction

The use of magnetic spectrometers in nuclear physics research has been pivotal, providing an invaluable tool in the efforts to study charged particles produced in nuclear reactions. These instruments rapidly became indispensable in conventional nuclear physics laboratories due to their advantages over other detection techniques. Specifically, they offer a strong selection of the reaction products, depending on their momentum over charge ratio (p/q), that enables a significant reduction of the experimental background; thus, leading to an effective detection of particles at very forward angles. Another significant advantage is the capability to offer exceptional mass, momentum and angular resolution, paving the way to detailed spectroscopy studies.

However, the use of traditional magnetic spectrometers has been challenged over the years due to their inherently limited acceptance. This is a limitation arising mainly from aberrations in the optical designs of the magnets. To alleviate these limitations, innovative solutions were employed such as the use of correcting lenses and high-order ray-reconstruction techniques. The subsequent inclusion of major technological upgrades such as multipole lenses and gas filled focal plane detectors, especially multi-wire proportional counters of many kinds, further advanced magnetic spectrometry, allowing for higher resolution and more effective aberration corrections [57].

The advent of computational tools like COSY INFINITY [58] and differential algebra techniques proved to be a turning point in the field of magnetic spectroscopy, as these tools enabled the reconstruction of particle trajectory. To give an overview of the reconstruction technique, in standard ion optics [59], the motion of a beam of charged particles under the influence of magnetic fields is described via a phase space representation. The initial phase space vector $Q_i \equiv (\theta_i, Y_i, \phi_i, \delta)$ defined at the target point, is connected to the final one $Q_f \equiv (X_f, \theta_f, Y_f, \phi_f)$ by a nonlinear transport map characteristic of the spectrometer's optical system, as follows:

$$G : Q_i \to Q_f \tag{2.1}$$

In the aforementioned vectors, θ_i and ϕ_i represent the horizontal and vertical angles, respectively, Y_i the vertical position coordinate and $\delta = (p - p_0)/p_0$ the fractional momentum deviation, with p being the ion momentum and p_0 the reference one. The final parameters X_f, θ_f, Y_f, ϕ_f are the horizontal and vertical coordinates and angles of the ions in a plane normal to the reference trajectory. Eq. 2.1 can be mathematically inverted to reconstruct the initial momentum vector from the measured parameters at the focal plane, as follows:

$$G^{-1} : Q_f \to Q_i \tag{2.2}$$

However, this process is complicated for nonlinear aberrations, which can ultimately lead to degradation of the resolution if not properly corrected. For this reason, a reliable method of solving the nonlinear transport equations was developed at Michigan State University for the S800 spectrometer of NSCL and implemented in programs like COSY INFINITY. This technique employs differential algebra to calculate high-order transport matrices, avoiding the computationally expensive ray-tracing procedures traditionally used. Furthermore, it ensures that the magnetic fields are accurately described, even when derived from interpolated datasets [60, 61]. A high accuracy is also needed for the several geometrical quantities defining the spectrometer layout. This is achieved via accurate measurements and alignments of all the elements of the spectrometer. By combining high-resolution focal plane detection with this mathematical framework, the initial phase space parameters can be reconstructed with high accuracy, enhancing the spectrometer's performance in large-acceptance experiments.

This approach has been impactful in instruments like MAGNEX, where the use of high-order ray-reconstruction techniques allows for up to 10^{th}-order aberration correction. The method not only compensates for distortions, but also enables a detailed understanding of ion transport efficiency at different locations across the spectrometer. This procedure would be challenging to achieve with purely experimental techniques due to the difficulty of installing detectors along the ion trajectory [62].

The capability offered by these advancements to perform large-acceptance measurements while maintaining high resolution has opened new pathways in heavy-ion physics, the production of exotic nuclei, as well as the study of rare reaction mechanisms. Modern magnetic spectrometers, such as MAGNEX, have been designed with large angular and momentum acceptances to accommodate the demands of contemporary nuclear physics experiments. These include studies involving low-intensity radioactive ion beams, suppressed reaction channels, and rare processes like Double Charge-Exchange (DCE) reactions, which are essential for investigating nuclear matrix elements relevant to neutrinoless double-beta decay [63].

This chapter provides a detailed overview of the experimental setup and measurement techniques employed to investigate medium mass ejectiles in heavy-ion reactions at the Fermi energy domain ($\sim$ 10–30 MeV/nucleon) using the large acceptance spectrometer MAGNEX at INFN-LNS. The experiment, proposed by us and approved by the Program Advisory Committee (PAC), was performed at the Istituto Nazionale di Fisica Nucleare - Laboratori Nazionali del Sud (INFN-LNS) in Catania, Italy. The work focuses on peripheral collisions of medium-mass heavy ions, with the goal of obtaining high-resolution measurements of ejectile distributions. In this chapter we outline the design and operation of the experimental apparatus, the configuration of the spectrometer, and the procedures followed for data acquisition and analysis.

2.2 MAGNEX Spectrometer and Measurements

MAGNEX is a large-acceptance magnetic spectrometer installed at the INFN-LNS laboratory in Catania. It is a high-acceptance device which makes use of both the advantages of the traditional magnetic spectrometry and those of a large angular and momentum acceptance detector. The spectrometer is composed of two large aperture magnets, manufactured by Danfysik A/S, namely a quadrupole followed by a 55° dipole and a Focal Plane Detector (FPD), built in collaboration with GANIL, for the detection of the emitted ions. A schematic view of the apparatus is shown in Fig. 2.1 [21].

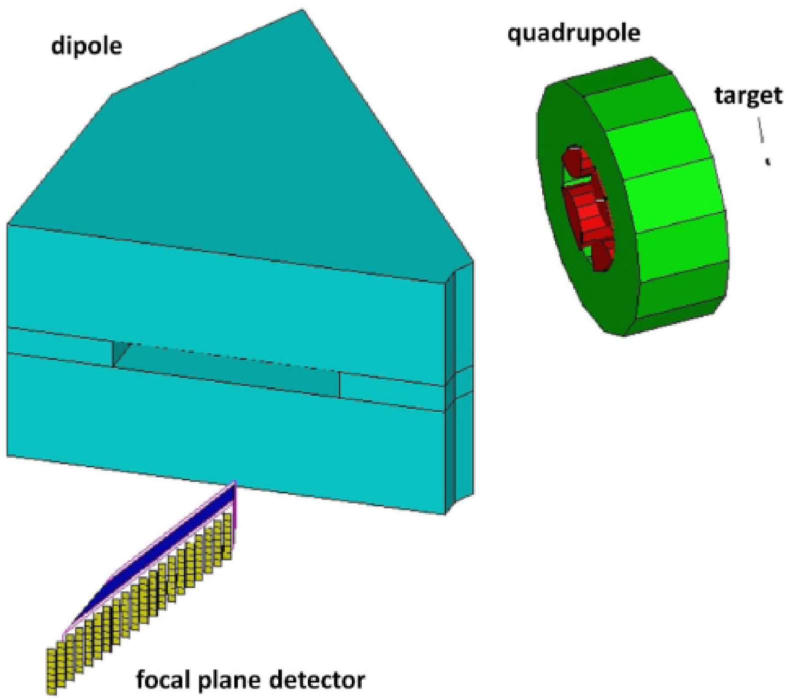

Figure 2.1: A schematic view of MAGNEX

2.2.1 Focal Plane Detector

A beam of $^{70}Zn^{15+}$ at 15 MeV/nucleon delivered by the S800 superconducting cyclotron bombarded a 1.18 mg/cm^2 ^{64}Ni foil at the optical object point of the MAGNEX large acceptance spectrometer [64, 65, 21]. The spectrometer's optical axis was positioned at 9.0°, allowing MAGNEX to cover an angular range from 4.0° to 15.0°. The unreacted beam was collected in an electron suppressed Faraday cup inside the target chamber. The ejectiles emerging from the target passed through a 6 μm Mylar stripper foil and then were momentum analyzed by the MAGNEX spectrometer [66, 67] and detected by its focal plane detector (FPD) [68, 69].

The structure of MAGNEX mainly involves of a vertically focusing quadrupole and a horizontally dispersing and focusing magnet. This apparatus provides a momentum acceptance of about 24% and a solid angle of 50 msr [68]. This performance results from the implementation of trajectory reconstruction. The development of such a complex apparatus requires an advanced Focal Plane Detector (FPD) too. This detector is responsible of providing an unambiguous particle identification, but also an accurate tracking of the ions trajectory as they pass through the various magnetic elements of the spectrometer. The focal plane detector (FPD) is a large ($1360{\times}200{\times}90$ mm^3 active volume) gas-filled hybrid detector with a wall of 60 large-area silicon detectors ($50{\times}70{\times}0.5$ mm^3) arranged in three rows at the end. It mainly consists of two parts: a gas tracker sensitive to the energy loss of the reaction products and a stopping wall of silicon detectors for the measurement of their residual energy. The gas tracker is inside a vacuum chamber and has a mylar window with typical thickness ranging from 1.5 μm to 6 μm. The active region of the gas tracker is filled with isobutane with pressure ranging from 5 to 100 mbar. In our experiment, as already mentioned, a mylar window of 6 μm thickness and isobutane of 40 mbar were used. To avoid any further dead layers there is no exit window. The Si detectors are located inside the gas volume.

2.2.2 Energy Loss

Figures 2.2 and 2.3 represent sketches that depict the bottom and the lateral view of the MAGNEX FPD, respectively. One can distinguish three different regions:

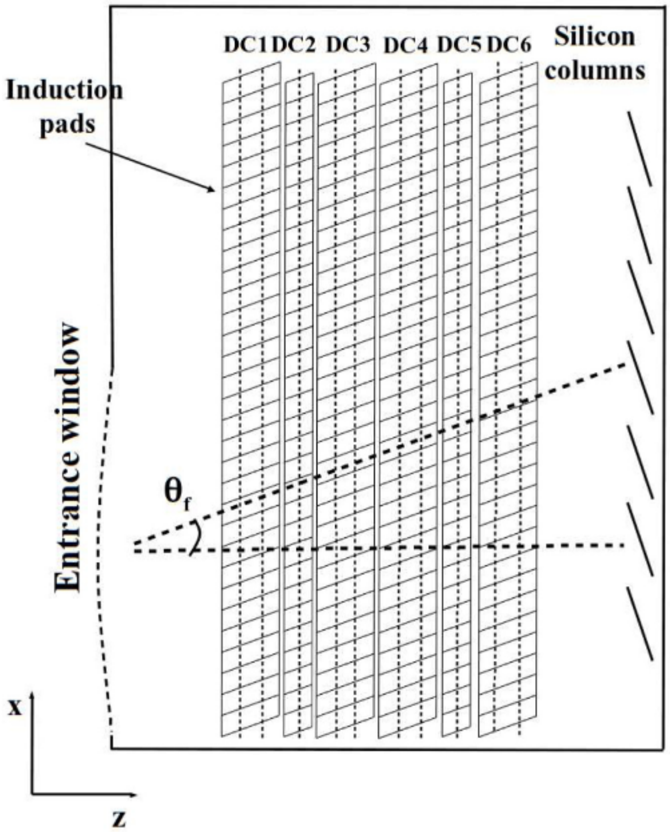

Figure 2.2: Sketch of the bottom view of the FPD. [68]

the drift region, the multiplication region and the induction region, where the latter can be seen more thoroughly in the first sketch which depicts the bottom view of the FPD. The drift region consists of the cathode, an aluminum plate and a Frisch grid. The multiplication region is defined by the Frisch grid and the plane where ten proportional wires are located. The ten wires are shared among six Drift Chambers DCi = 1,2,...,6. Specifically, DC2 and DC5 have just a single wire while the other DCs have two proportional wires. The induction region is defined by the plane where the ten proportional wires lay and the anode. The anode is divided in six longitudinal strips, one for each DC. The operation principle of the FPD is rather standard. When an incident charged particle coming from the dipole crosses the entrance window of the FPD, it generates a track of ions and electrons in the gas section between the cathode and the Frisch grid. The presence of a uniform electric field of around 50 V/cm, drifts the primary electrons towards the grid with a constant velocity. Then the electrons pass in the multipli-

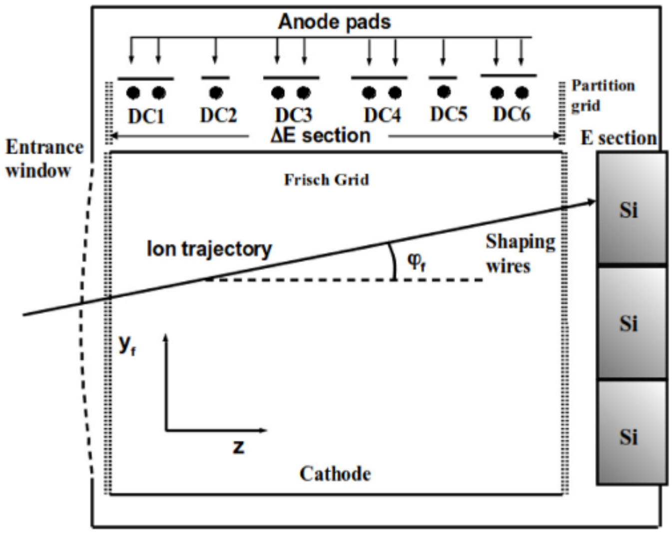

Figure 2.3: Sketch of the lateral view of the FPD. [68]

cation region where they are being accelerated by the strong electric field from the proportional wires. Due to the fact that the gas counter works in the proportional regime, the electron avalanches that are produced close to the wires are proportional to the energy loss of the ion in the gas. Hence, six independent signals are given for the energy loss, one for each DC. With the use of proper amplifiers, the signals are shaped and amplified. These amplified signals are used for particle identification. The total measured energy loss is given by the equation:

$$\Delta E_{tot} = \sum_{i=1}^{6} \Delta E_i \tag{2.3}$$

The logic outputs are also used as a STOP signal for measuring the drift time of the electrons. Furthermore, for each event, the total energy loss ΔE_{tot} in the FPD needs to be corrected for the angle of incidence at the focal plane, giving the corrected energy loss ΔE_{cor} corresponding to the angle of incidence $\theta_{inc} = 59.2°$ of the central trajectory. It means that:

$$\Delta E_{cor} = \frac{cos\theta_{foc}}{cos\theta_{inc}} \Delta E_{tot} \tag{2.4}$$

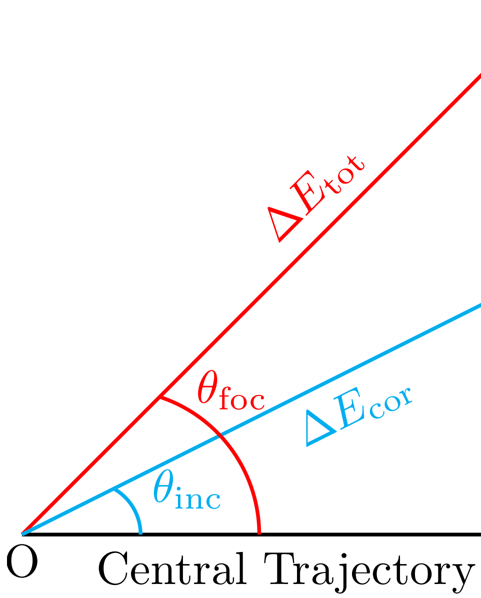

Figure 2.4: Visualization of θ_{inc} and θ_{foc} with respect to the central trajectory, ΔE_{cor}, and ΔE_{tot}.

Apart from the signal produced from the DC wires, the electron avalanche is responsible for the induction of a charge in a given number of pads that are laying above the wires. This type of multiplexed signals are then readout and digitally converted. The center of gravity of the charge distribution at each DC wire is finally extracted, leading to the identification of the horizontal position (X$_{foc}$) and the horizontal angle (θ_{foc}) of each incident particle. As far as the vertical coordinates are concerned, they are extracted by measuring the arrival time of the electron avalanches in the wires. Of course, it essential that the gas tracker works in the proportional regime as already mentioned, where the drift velocity is almost constant in the whole volume of the detector system. The drift times in the gas are measured by the interval between the signal provided by the Si detectors (START) and the DCs (STOP), using six standard TAC+ADC readout chains. This way, six vertical positions are extracted, one for each wire, that are used to obtain the vertical position (Y$_{foc}$) and the angle (ϕ_{foc}). As can be seen in Fig. 2.5, there has been a cross-talk [69, 70] in the induced signals between two neighboring detectors on the FPD. The electron avalanche produced by a given proportional wire is also capable of inducing a charge in pads that correspond to a neighboring wire. Thus, the extracted charge distributions for a given wire could be distorted affecting the determination of the horizontal coordinates.

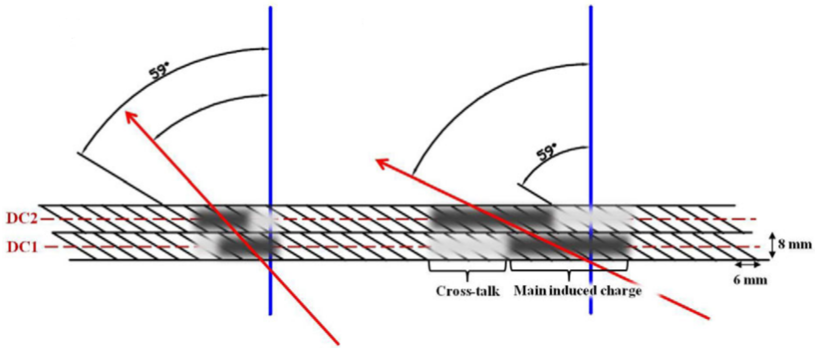

Figure 2.5: Sketch depicting details from the induction pad. The red arrows represent the main induced charge over the electrode after the ion passing. The gray shadow is an indication of the cross-talk signal induced by the neighbor DC. [69]

In order to alleviate the problem of cross-talk, the geometry of the wires and the strips was changed, introducing a 2 mm spacer between two adjacent strips as can be seen on the left-hand side of Fig.2.6. On the right-hand side of the same figure, a schematic representation of the induction signals is shown, specifically in the region of DC4, DC5, and DC6 multiplication wires. The dotted areas indicate the presence of a cross-talk induced signal, where the filled areas correspond to areas of main charge induction. Apart from the modification of the geometry of the FPD, a proper procedure was implemented to estimate the cross-talk induced signal and reported in ref. [21, 66, 67, 68, 69].

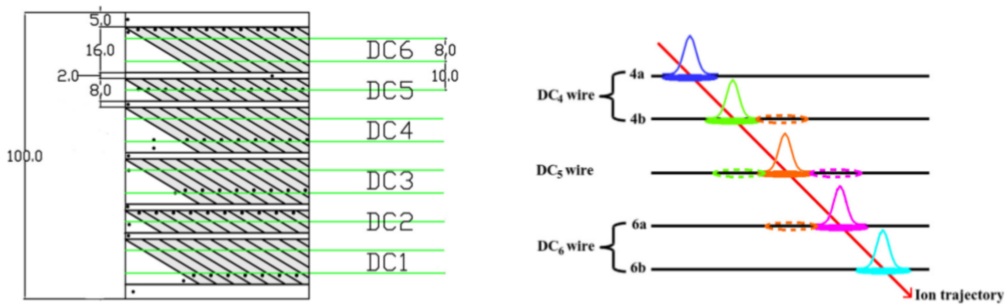

Figure 2.6: Left panel: Scale drawing depicting six strips that correspond to the six drift chambers. Each strip is segmented in pads (gray colored area). Right Panel: Schematic representation of the induction signal formation in specific DC wires.

2.2.3 Silicon Wall - Residual Energy Extraction

As mentioned above, the silicon stopping wall is embedded in the gas in order to avoid further dead layers. The "wall" has 60 silicon pad detectors, arranged in 20 columns and 3 rows. Each one of the silicon detectors has a rectangular shape, an active area of $50x70$ mm^2 and a thickness of 500 μm. The silicon columns are mounted orthogonally to the spectrometer optical axis. This way the effective dead layer is minimized. When the charged particles cross the gas section of the FPD, they finally reach the silicon detector wall. Charge pre-amplifiers similar to those used for the wire signals are used. The outputs are sent to shaping amplifiers providing spectroscopic and timing outputs. The spectroscopic signals provide the residual energy (E_{resid}) of the incident particles. Timing signals can be used to measure the Time Of Flight (TOF) as will be described further on in this work, among other uses.

In the present experiment only about one-half of the active area of FPD was used (the other part was covered with an aluminum screen) in order to avoid radiation damage of the silicon detectors and high dead times due to limitations in the data acquisition system. These experimental restrictions will be circumvented in the future in view of the upgrading of the MAGNEX facility [71]. Thus, in a full acceptance run, the whole area of the FPD can be exposed to the flux of the reaction products, especially for the investigation of very suppressed reaction channels. Furthermore, in this experiment a set of vertical slits before the quadrupole restricted the vertical angular acceptance of MAGNEX in the range -0.8 to 0.8 degrees. The restriction of the vertical acceptance and the active area of the FPD resulted in the use of only seven of the silicon detectors belonging to the middle row of the detector system. For the present analysis, the silicon detectors used are the following: Si-8, Si-11, Si-14, Si-17, Si-20, Si-23, Si-26. The signals of the silicon detectors gave the start for the time of flight (TOF) measurement of the particles through the spectrometer, while the cyclotron's radiofrequency (RF) of 20 MHz provided the stop signal. This setup provided a modest TOF resolution of $\sim$3 ns, limited mainly by the cyclotron RF timing.

The experiment at the INFN/LNS was performed in June 2018 and spanned five days, where a series of runs were carried out. The experiment conducted using the spectrometer comprised a total of 90 runs. However, not all these runs were directly utilized in the scope of the present work. Among these runs, several shared similar experimental configurations, such as the use of the same projectile and target, the employment of the same beam current and the same settings of the MAGNEX spectrometer. To streamline the analysis and organization of the data, the runs were categorized into distinct groups, referred to as run sets. Each run set represents a collection of runs characterized by consistent experimental settings, ensuring a logical structure for data interpretation and facilitating comparisons across different configurations.

The main run sets utilized for the purposes of this study are (Table 2.1):

- Runs 22–34, 41–61, 64–69: Corresponding to ^{70}Zn $+^{64}$ Ni reaction (Run Set "ZnNi").
- Runs 16–19: Corresponding to ^{70}Zn $+^{208}$ Pb reaction (Run Set "ZnPb").
- Run 39: Corresponding to ^{70}Zn $+^{27}$ Al reaction (Run Set "ZnAl").

Run Set	**Runs**	**Projectile**	**Target (thickness)**	**Bρ Setting (Tm)**	**Notes**
ZnNi	22-34, 41-61, 64-69	^{70}Zn	^{64}Ni$(1180\mu g/\text{cm}^2)$	1.2880 (Runs 22-34,41-61) 1.3594 (Runs 64-69)	Main focus of this work
ZnPb	16-19	^{70}Zn	^{208}Pb$(1164\mu g/\text{cm}^2)$ + C$(40\mu g/\text{cm}^2)$	1.2635	For cross section normalization
ZnAl	39	^{70}Zn	Al $(810\mu g/\text{cm}^2)$	1.2880	Additional reactor data

Table 2.1: Details of the run sets analyzed in this work.

In the following chapters, the focus of this work will be on the data analysis of the "ZnNi" run set, which corresponds to the ^{70}Zn + ^{64}Ni reaction. This analysis involves the detailed presentation of the particle identification approach, followed by the extraction of momentum, angular, mass distributions, including the reconstructed excitation energy distributions. It is worth noting that the same methodology was applied to the other run sets. Selected results from these additional analyses will also be presented.

The experimental setup described in this chapter was designed to address the primary goal of identifying neutron-rich ejectiles in medium-mass heavy-ion reactions at 15 MeV/nucleon. The use of the MAGNEX large-acceptance magnetic spectrometer, with its carefully calibrated detection systems and capabilities, ensured reliable and precise data collection. The data acquisition and particle identification approach will be presented in the following chapter of this work. The results presented later on will serve as strong indicators of effective particle production, supporting the validity of our experimental approach and providing important information regarding the reaction mechanisms of peripheral collisions at this energy regime.

Chapter 3
Data Analysis

3.1 Introduction

In this chapter, the focus shifts from the experimental setup to the methodologies employed in analyzing the data obtained from the studied reaction. The main interest of this work was to examine the feasibility of medium-mass ejectile identification in this energy regime. The main reaction under study (Run Set "ZnNi"), produced projectile-like fragments with atomic numbers Z=26-32 and mass numbers A =60–72. These fragments are central to exploring the production of neutron-rich nuclei and the underlying reaction mechanisms.

Initially, traditional approaches to reconstruct the atomic number (Z) were applied, relying on correlations between the total energy loss (ΔE_{cor}) in the gas section of the FPD and the residual energy (E_{resid}) measured by the silicon detectors. Previous studies with the MAGNEX spectrometer have demonstrated that this approach is effective for lighter ions (e.g., ^{18}O, ^{20}Ne, [72]). However, for medium-mass heavy ions, as examined in this work, this correlation alone was insufficient. Consequently, a different reconstruction methodology, utilizing the measured and calibrated quantities ΔE_{cor}, E_{resid}, and time-of-flight (TOF) was necessary to achieve reliable identification.

Following the successful identification of the reaction products, the next step was to study distributions for various reaction channels, with particular attention to neutron-rich isotopes. These distributions—including angular, momentum, and mass spectra—offer valuable insights into the production trends of neutron-rich nuclei and provide a basis for comparison with theoretical models, advancing our understanding of the reaction mechanism.

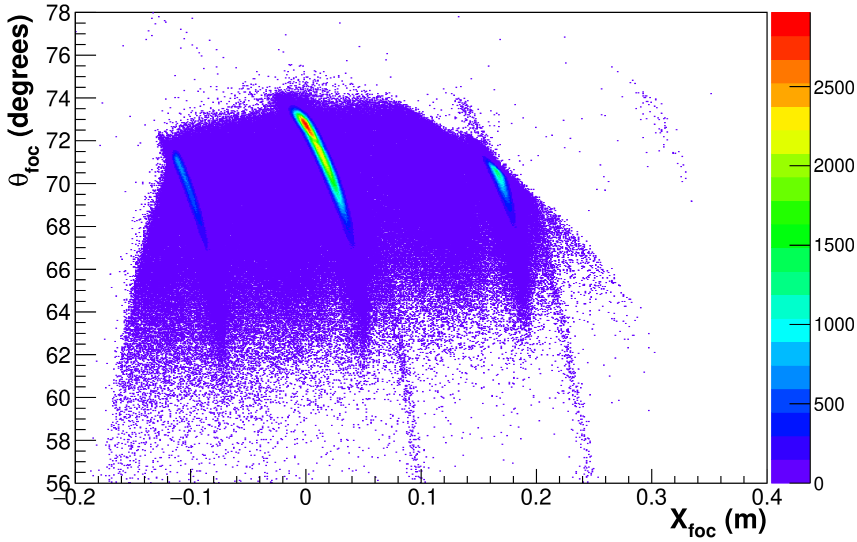

Figure 3.1: Plot of the horizontal angle versus the horizontal position measured at the MAGNEX focal plane for ejectiles from the interaction of a ^{70}Zn beam (15 MeV/nucleon) with a ^{64}Ni target distributed on all the FPD silicon detectors used for this experiment, namely Si-8, Si-11, Si-14, Si-17, Si-20, Si-23, Si-26.

3.2 Particle Identification Procedure

The magnetic rigidity in this experiment was set properly in order to transport the ejectiles and bring them to the center of the FPD. A typical plot of the horizontal angle (θ_{foc}, in degrees) versus the horizontal position (X_{foc}, in meters) measured at the FPD is presented in the following three figures. In these figures, unidentified experimental data of ejectiles from the ^{70}Zn (15 MeV/nucleon) + ^{64}Ni reaction are shown. Specifically, in Fig. 3.1, these data are distributed on all silicon detectors (Si-8, Si-11, Si-14, Si-17, Si-20, Si-23, Si-26). In Fig. 3.2, these data are distributed on four silicon detectors (Si-8, Si-14, Si-20, Si-26). The blank areas correspond to data of the 3 other silicon detectors, eliminated by software gates, for better clarity of the presentation. Moreover, the red lines correspond to simulated data for elastically scattered ^{70}Zn ejectiles at the charge states $30+$, $29+$ and $28+$, from left to right, respectively, being in their ground state. In Fig. 3.3, the same correlation is presented but this time the previously omitted Si detectors are shown (Si-11, Si-17, Si-23). While the blank areas correspond to data of the rest 4 Si detectors that are now omitted.

After the description of the setup and the overview of the collected events, as

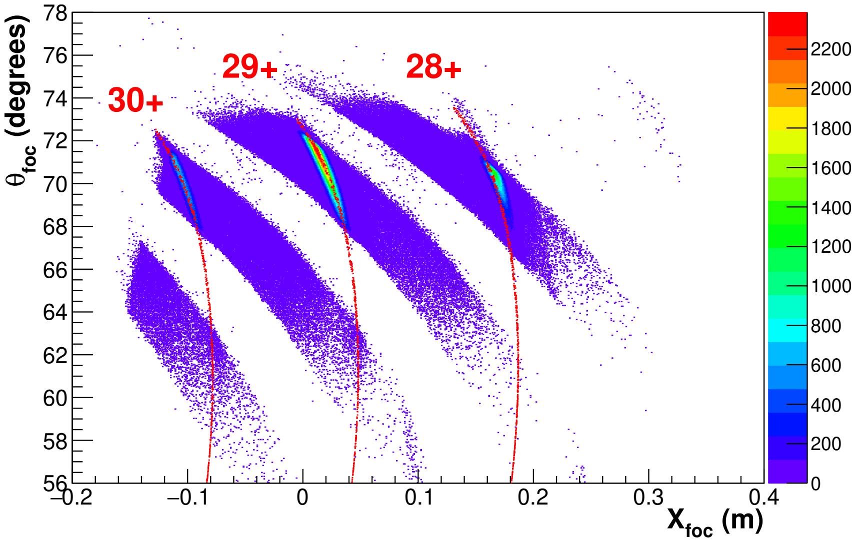

Figure 3.2: Plot of the horizontal angle versus the horizontal position measured at the MAGNEX focal plane for ejectiles from the interaction of a ^{70}Zn beam (15 MeV/nucleon) with a ^{64}Ni target distributed on four of the FPD silicon detectors, namely Si-8, Si-14, Si-20 and Si-26. The open (blank) areas correspond to three other silicon detectors, namely Si-11, Si-17, Si-23 (whose data are omitted by software gates) adjacent to the ones whose data are shown. The red lines are simulations for elastically scattered ^{70}Zn ejectiles in the charge states $30+$, $29+$ and $28+$, from left to right, respectively.

illustrated in the horizontal angle versus horizontal position plots, the approach for the identification procedure of the reaction products will be presented. This approach is based on the technique of [68]. Specifically, the determination of the atomic number of the ejectiles involves a correlation between the residual energy measured by the silicon detectors and the total energy loss in the gas section of the Focal Plane Detector of the spectrometer corrected for path length differences depending on the angle of incidence.

In Fig. 3.4, two plots depicting the total energy loss at the gas section of the FPD versus the residual energy measured by a single silicon detector are presented. From now on, this Si detector (Si-11) will be considered as a "reference" Si detector. The left panel displays the results of the analyzed data from this experiment, specifically focusing on the reaction observed with the MAGNEX spectrometer. The Si detector, marked with an asterisk in Fig. 3.3, was utilized for this analysis. To refine the dataset, elastic events corresponding to ^{70}Zn^{30+}, ^{70}Zn^{29+}, ^{70}Zn^{28+} were excluded by applying a dedicated software gate. This gate was implemented in the θ_{foc} versus X_{foc} correlation, as illustrated in Figs. 3.2 and 3.3.

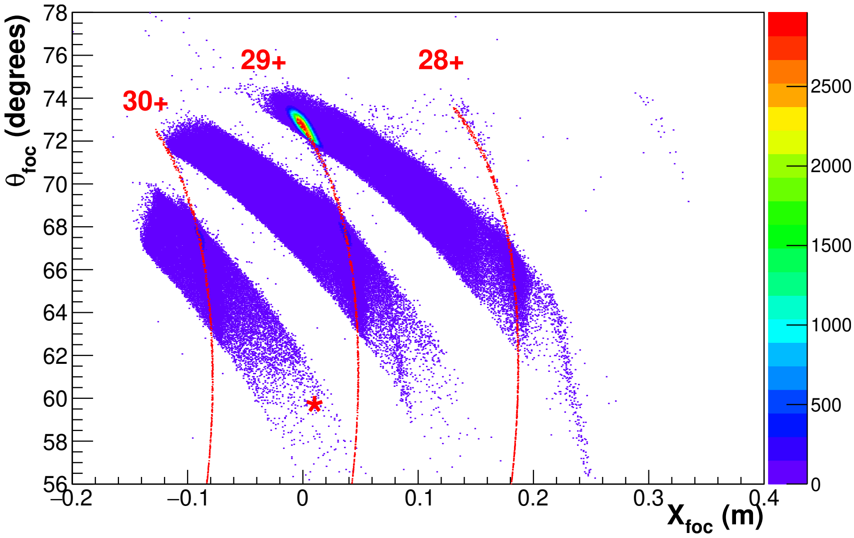

Figure 3.3: Plot of the horizontal angle versus the horizontal position measured at the MAGNEX focal plane for ejectiles from the interaction of a ^{70}Zn beam (15 MeV/nucleon) with a ^{64}Ni target distributed on three of the FPD silicon detectors, namely Si-11, Si-17 and Si-23. The open (blank) areas correspond to four other silicon detectors, namely Si-8, Si-14, Si-20 and Si-26 (whose data are omitted by software gates) adjacent to the ones whose data are shown. The red lines are simulations for elastically scattered ^{70}Zn ejectiles in the charge states $30+$, $29+$ and $28+$, from left to right, respectively. The asterisk designates the "reference" detector (Si-11) which can be seen on the following figure.

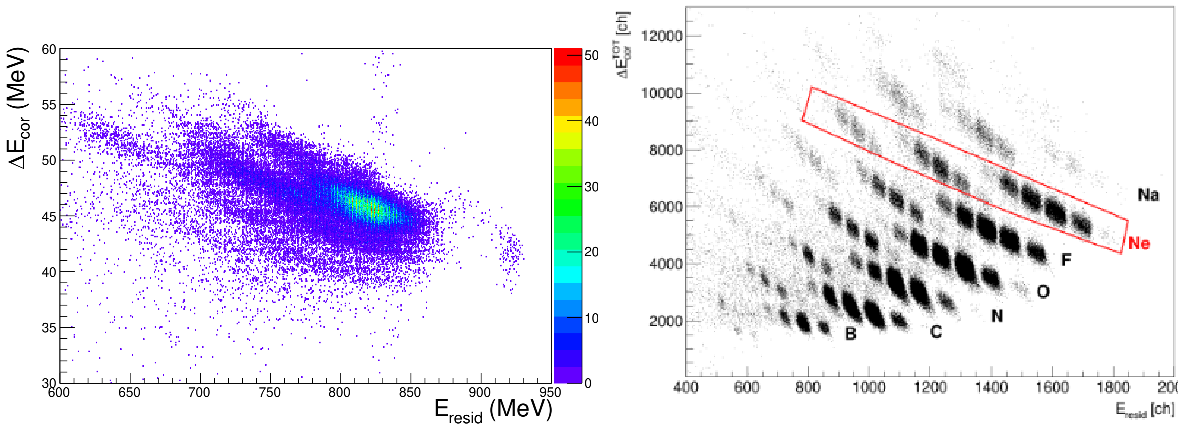

Figure 3.4: ΔE_{cor} vs E_{resid} correlation for the identification of Z. On the left, our data from the reaction of ^{70}Zn + ^{64}Ni with the MAGNEX spectrometer are presented. On the right, data from [72] for ^{20}Ne^{10+} induced reactions are presented.

On the right panel, the results from the analysis that was carried out in Ref. [72] are shown. It is evident that this correlation is actually adequate for the determination of the atomic number Z of light ions. However, in the case of heavier medium-mass ions, a clear Z separation could not be obtained. For this reason, the particle identification approach was extended with the measurement of the time of flight and a reconstruction of the atomic number Z and charge state q of the ejectiles.

The Z reconstruction is based on the energy loss, the residual energy, as well as TOF measurements after an appropriate calibration of these parameters [72]. In the calibration procedure of the energy loss and the residual energy, advantage was mainly taken of the fact that the elastically scattered ^{70}Zn ions enter the FPD in a broad range of angles (as indicated in Fig. 3.2, 3.3 with the red lines), thus providing calibration points of ΔE_{tot} and E_{resid} for successive θ_{foc} angle windows. In the present analysis, several variants of the Z reconstruction approach have been developed. An overview of these will be presented in the following subsections.

3.2.1 First Effort of PID: Z_I, q approach

The first approach was based on the measured quantities of time-of-flight (TOF) and ΔE_{cor}. Guided by Bethe-Bloch's stopping power formula $\Delta E \propto \frac{Z^2}{v^2}$, the atomic number Z may be expressed as $Z \propto v\sqrt{\Delta E_{cor}}$, where v is the velocity of the ejectiles. Following this dependence, we can reconstruct Z with the expression:

$$Z_I = a_0(v) + a_1(v)v\sqrt{\Delta E_{\text{cor}}} + a_2(v)(v\sqrt{\Delta E_{\text{cor}}})^2 \tag{3.1}$$

In order to determine the functions $a_0(v)$, $a_1(v)$, and $a_2(v)$ in the velocity range of interest, the energy-loss data of Hubert et al. [73] were employed to determine the coefficients of this equation for the atomic number range $6 \leq Z \leq 36$ and in the energy range of 8–18 MeV/nucleon. A least-squares fitting procedure was applied at each energy in steps of 0.5 MeV/nucleon. The values of each coefficient at the various energies were then fitted with polynomial functions of velocity.

The TOF measurement, along with the trajectory length of each particle, enabled the determination of the velocity of the ejectiles:

$$v = \frac{L}{\text{TOF}} \tag{3.2}$$

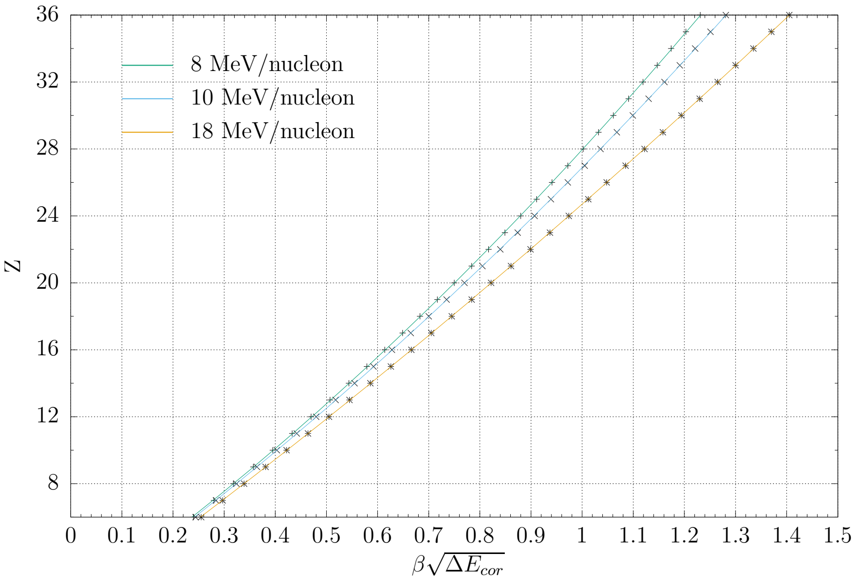

Figure 3.5: Example Z vs $\beta\sqrt{\Delta E_{cor}}$ correlation for ejectiles for Z = 6-36 at 8, 10 and 18 MeV/u, with $\beta = \frac{v}{c}$.

where L is the trajectory length obtained from the trajectory reconstruction, as reported in [21]. Furthermore, calculation of the ionic charge state q was based on the fundamental equation of magnetic spectrometry:

$$B\rho = \frac{p}{q} \tag{3.3}$$

where $B\rho$ represents the magnetic rigidity, and p denotes the momentum of the particle. Within the context of this work, we have used an equivalent expression for the magnetic rigidity that is:

$$B\rho = \frac{1}{\alpha}\frac{pc}{q} \tag{3.4}$$

with $\alpha = 299.79\ \frac{MeV}{T \cdot m}$. In this expression, the magnetic rigidity $B\rho$ is expressed in Tesla · meters (T·m), the momentum in MeV/c and q is the integer value of the charge state of the ion. In a non-relativistic approach, the total kinetic energy E_{tot} of the ions reaching the focal plane can be expressed as:

$$E_{tot} = \frac{1}{2}mv^2 = \frac{1}{2}(m_n A)\left(\frac{v}{c}\right)^2 = \frac{1}{2}(m_n c^2 A)\beta^2 \tag{3.5a}$$

$$E_{tot} = \frac{p^2}{2m} = \frac{(pc)^2}{2mc^2} = \frac{(pc)^2}{2m_n c^2 A} \tag{3.5b}$$

where m is the mass of the ion, m_n the atomic mass, A the mass number of the ion and $\beta = \frac{v}{c}$. Combining the last terms of equations 3.5a and 3.5b, we can express the momentum p as:

$$pc = \sqrt{2m_n\ c^2\ A\ E_{tot}} = \sqrt{2m_n\ c^2\ \left(\frac{2E_{tot}}{m_n c^2 \beta^2}\right)\ E_{tot}}$$

leading to:

$$pc = \frac{2E_{tot}}{\beta} \tag{3.6}$$

By substituting 3.6 into eq. 3.4, the charge state q can be finally expressed as:

$$q = \frac{1}{\alpha}\ \frac{1}{B\rho}\ \frac{2E_{tot}}{\beta} \tag{3.7}$$

The total kinetic energy of the ions reaching the FPD is determined from the expression:

$$E_{\text{tot}} = \Delta E_w + \Delta E_{\text{tot}} + E_{\text{resid}} \tag{3.8}$$

where ΔE_w is a calculated correction for the energy loss in the entrance window of the FPD, ΔE_{tot} is the sum of the measured energy loss in the gas section of the FPD and E_{resid} is the residual energy measured by the Si detectors, as previously mentioned.

The magnetic rigidity $B\rho$ is obtained from the following equation:

$$B\rho = B\rho_0\ (1 + \delta) \tag{3.9}$$

where $B\rho_0$ is the magnetic rigidity of the central trajectory and δ is the fractional deviation of the magnetic rigidity of the particle from that corresponding to the central trajectory, calculated through the standard procedure of optical reconstruction as reported in [21].

The first effort for particle identification involved a correlation of the reconstructed atomic number Z with the reconstructed ionic charge state q of the products in a two dimensional plot (Fig. 3.6).

However, the correlation of Z_I with q did not yield a sufficient Z separation.

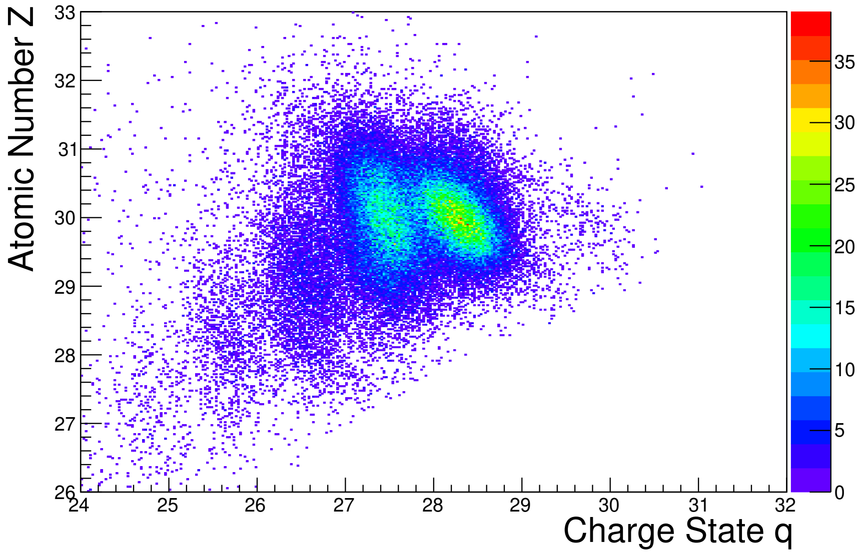

Figure 3.6: Reconstructed Z_I vs charge state q correlation of ejectiles from the reaction ^{70}Zn (15 MeV/nucleon) + ^{64}Ni corresponding to the reference Si detector.

For this reason, a different approach was implemented, for the reconstruction of Z as described below.

3.2.2 Second Effort: Z_{II}, q Approach

The second approach is similar to the first one described before, but takes into account both ΔE_{cor} and E_{tot}, as well as the velocity of the products. Following Bethe-Bloch's formula, and considering that the total kinetic energy of the incident ions is proportional to the velocity squared, $E_{\text{tot}} \propto \upsilon^2$, we can write:

$$\Delta E \propto \frac{Z^2}{E_{\text{tot}}} \tag{3.10}$$

$$Z \propto \sqrt{\Delta E_{cor} E_{\text{tot}}} \tag{3.11}$$

Based on Eq. 3.11, Z was then reconstructed using the expression:

$$Z_{II} = b_0(\upsilon) + b_1(\upsilon)\sqrt{E_{\text{tot}}\Delta E_{\text{cor}}} + b_2(\upsilon)\left(\sqrt{E_{\text{tot}}\Delta E_{\text{cor}}}\right)^2 \tag{3.12}$$

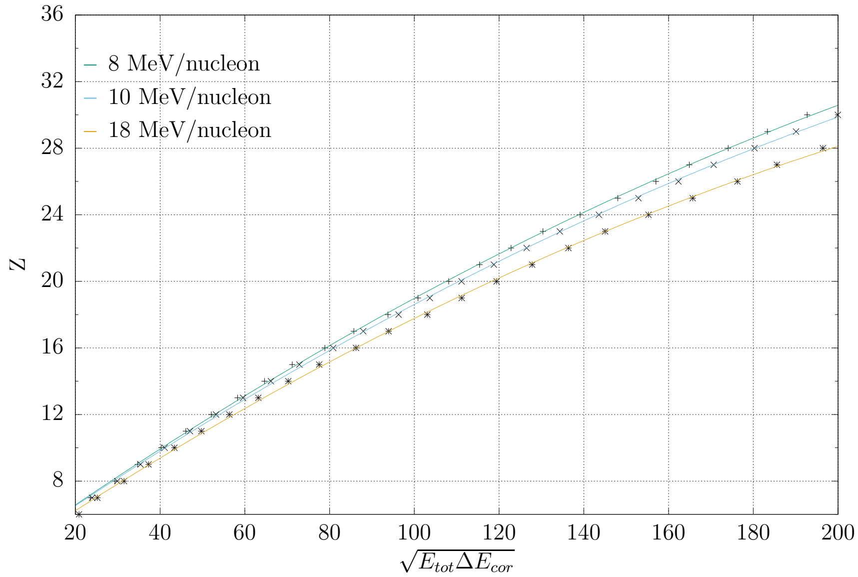

Figure 3.7: Example of the Z vs $\sqrt{E_{tot}\Delta_{cor}}$ as in Fig. 3.5.

As in the first approach, the functions $b_0(v)$, $b_1(v)$, and $b_2(v)$ were determined within the Z and velocity range of interest. This second approach involved a correlation of Z_{II} and q (as obtained before) for the ejectiles in a two dimensional plot (Fig. 3.8).

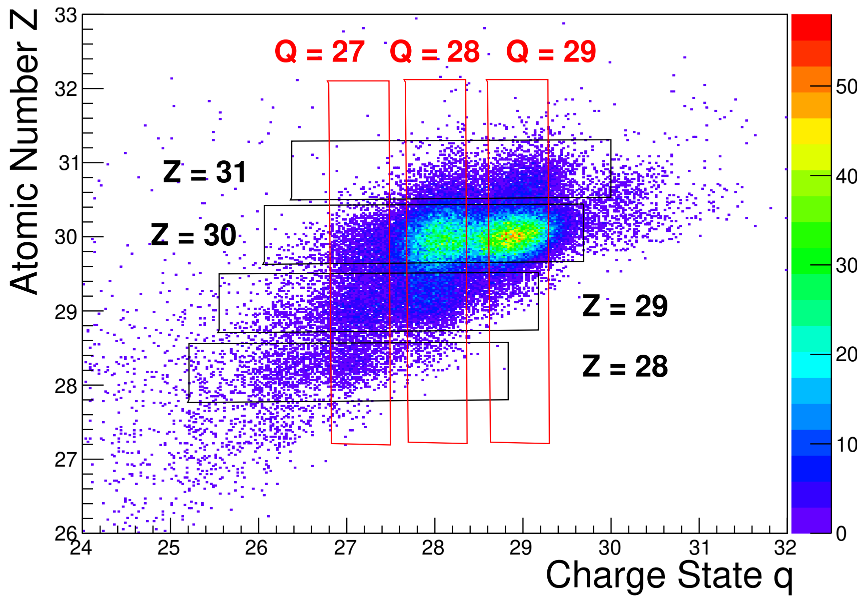

Figure 3.8: Reconstructed Z_{II} vs charge state q correlation of ejectiles from the reaction ^{70}Zn (15 MeV/nucleon) + ^{64}Ni corresponding to the same silicon detector using the second approach. Graphical contours are shown on each band corresponding to the atomic numbers Z (horizontal bands) and the ionic charge states q (vertical bands) of the ejectiles.

In a first glance, this approach leads to a rather adequate Z separation in comparison to the first one. At this point, we note that the Z_I reconstruction, based on TOF and ΔE_{tot}, shows inadequate resolution mainly due to the limited resolution of the TOF measurement.

However, the Z_{II} reconstruction based on the measured ΔE_{cor} and E_{resid} (employing the TOF measurement only in the velocity-dependent coefficients) reaches a rather adequate resolution.

3.2.3 Third Effort: Velocity Reconstruction from $\Delta E_{cor},\ E_{tot}$

Given the limited TOF resolution of ≈ 2.5 %, derived from $\Delta(TOF) = 3\ ns$ and a mean TOF value of 118.6 ns, we observed that the velocity resolution is directly dependent on the TOF resolution, resulting in an equivalent velocity resolution of ≈ 2.5 %, since the uncertainty in the length is negligible. To overcome this limitation, we decided to develop an approach for the velocity determination of the particles of interest based solely on ΔE_{cor} and E_{tot}. Again, starting from Bethe-Bloch's formula, we have:

$$\Delta E \propto \frac{Z^2}{v^2} \tag{3.13}$$

$$v \propto \frac{Z}{\sqrt{\Delta E}} \tag{3.14}$$

Now, Z can be expressed as:

$$Z \propto \lambda A \tag{3.15}$$

where λ has a typical value of ~ 0.5 for stable nuclei and of course depends on the N/Z of the nuclei (e.g. $^{70}_{30}Zn$ yields $\lambda = \frac{30}{70} = 0.43$) and Eq. 3.15 becomes:

$$v \propto \frac{\lambda A}{\sqrt{\Delta E}} \tag{3.16}$$

Now, considering the expression for the total kinetic energy of the particles:

$$E_{\text{tot}} = \frac{1}{2}(m_n c^2) A \frac{\upsilon^2}{c^2} \tag{3.17}$$

where m_n is the atomic mass. The mass number A can be written as:

$$A = \frac{2E_{\text{tot}}}{m_n \upsilon^2} \tag{3.18}$$

Using Eq. 3.16 in the above expression for velocity, we obtain:

$$\upsilon \propto \lambda^{1/3} \left(\frac{E_{\text{tot}}}{\sqrt{\Delta E}} \right)^{1/3} \tag{3.19}$$

where $\beta = \frac{\upsilon}{c}$. Following this proportionality, the velocity of the particles of interest was reconstructed as:

$$\beta_{\text{rec}} = c_0 + c_1 X + c_2 X^2 \tag{3.20}$$

where $X = \left(\frac{E_{\text{tot}}}{\sqrt{\Delta E_{cor}}} \right)^{1/3}$.

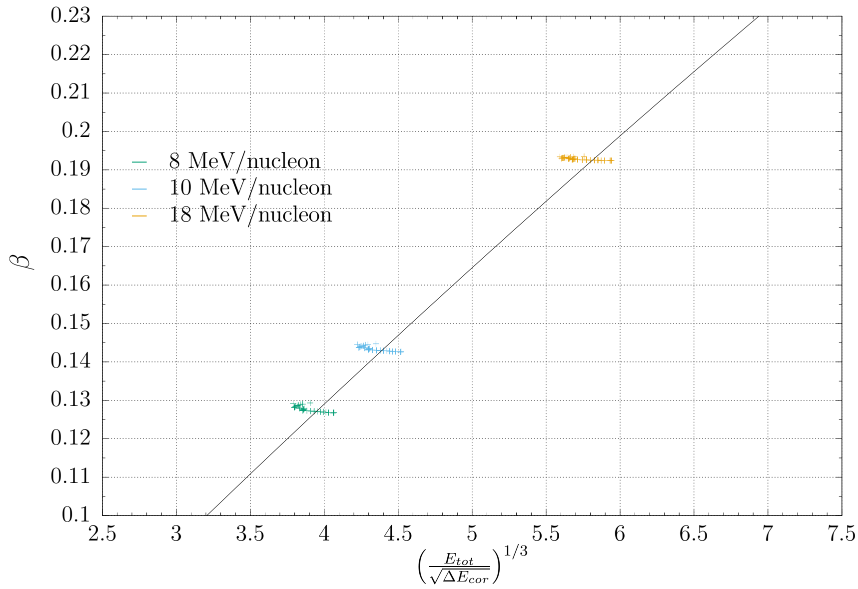

Figure 3.9: Example of the β vs. $\left(\frac{E_{\text{tot}}}{\sqrt{\Delta E_{cor}}} \right)^{1/3}$ correlation.

The reconstruction of the velocity with the above procedure, gave results equivalent to the ones obtained using the TOF measurement. However, this approach of velocity reconstruction had to be employed for those runs where TOF was not measured, namely Runs 22-34 for the Zn+Ni system and Run 39 for the Zn+Al system. In the subsequent analysis, we decided to employ the relativistic equations for velocity, momentum and energy. The reconstructed energy per nucleon of the particles is obtained from the reconstructed velocity via the relativistic expression:

$$E_{\text{n,rec}} = m_n c^2 \cdot (1 - \gamma_{\text{rec}}) \tag{3.21}$$

where

$$\gamma_{\text{rec}} = \frac{1}{\sqrt{1 - \beta_{\text{rec}}^2}}$$

and

$$\beta_{\text{rec}} = \frac{\upsilon_{\text{rec}}}{c}$$

It has already become clear that the reconstruction quality of the atomic number Z is dependent on the resolution of the velocity as we have seen in the previous two approaches of Z reconstruction. So, in this third effort we employ the aforementioned approach of Z reconstruction, Eq. 3.12, which depends on E_{tot} and ΔE_{tot} and where the velocity is now obtained via Eq. 3.20. The obtained atomic number is now denoted as Z_{III}.

Furthermore, we reconstruct the ionic charge state q, taking into account the relativistic expression of the momentum:

$$pc = \sqrt{E_{\text{tot}}\left(E_{\text{tot}} + 2m_n c^2 A\right)} \tag{3.22}$$

in the $B\rho$ equation:

$$B\rho = \frac{1}{\alpha}\frac{pc}{q} \tag{3.23}$$

so we get:

$$q = \frac{1}{\alpha}\frac{1}{B\rho}\sqrt{E_{\text{tot}}\left(E_{\text{tot}} + 2m_n c^2 A\right)} \tag{3.24}$$

Using $E_{tot} = A \cdot E_{n,rec}$ we get $A = \frac{E_{tot}}{E_{n,rec}}$. Then, Eq. 3.23 becomes:

$$q_{\text{II}} = \frac{1}{\alpha} \cdot E_{\text{tot}} \cdot \frac{\sqrt{1 + \frac{2m_n c^2}{E_{\text{n,rec}}}}}{B\rho} \tag{3.25}$$

Furthermore, the reconstructed parameters of Z and q obtained with the previous approach were correlated in two independent 2D plots with the residual energy. These correlations were adopted to take into account possible dependencies of the reconstructed parameters Z and q on energy (that turned out to be insignificant). In Fig. 3.10 the Z_{III} versus E_{resid} correlation of events collected by the reference silicon detector is shown. Adequate separation of the atomic numbers of the reaction products is achieved with a resolution (FWHM) of approximately 0.8 Z units.

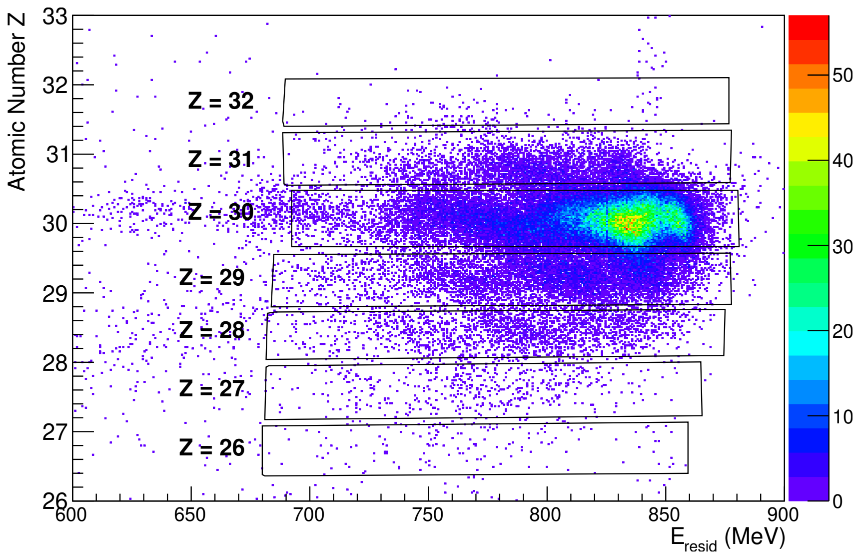

Figure 3.10: Reconstructed Z_{III} vs residual energy E_{resid} correlation of ejectiles from the reaction ^{70}Zn (15 MeV/nucleon) + ^{64}Ni corresponding to the reference silicon detector. Graphical contours are shown on each band corresponding to the atomic numbers Z = 26-32 (horizontal bands) of the ejectiles.

The next figure represents the q_{II} versus E_{resid} correlation of events collected by the reference silicon detector. Adequate separation of the ionic charge states of the ejectiles is achieved with a resolution (FWHM) of approximately 0.7 units.

From now on, we will use the Z_{III} and q_{II} and we will refer to these parameters simply as Z and q. The Z and q gates that were obtained through software gating from the Z vs E_{resid} and q vs E_{resid} correlations respectively, were used for the next step of the data analysis, that involves the identification of the masses.

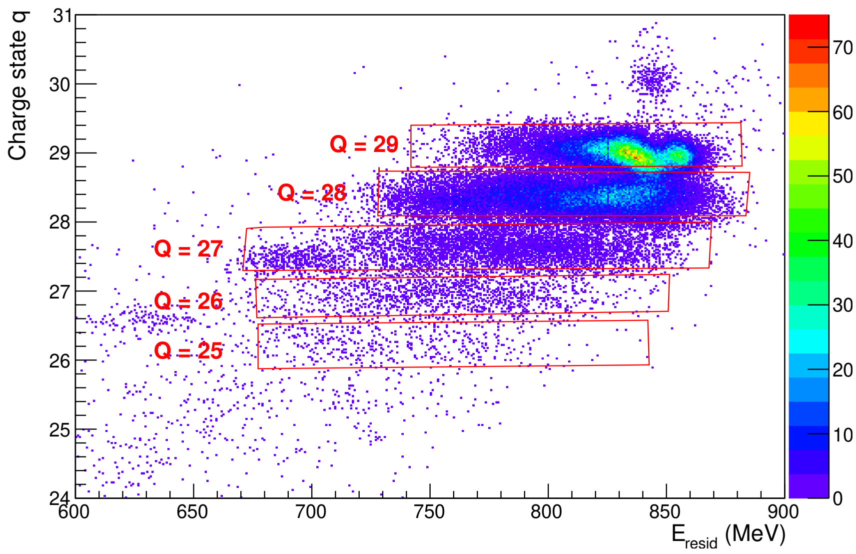

Figure 3.11: Reconstructed q_{II} vs residual energy E_{resid} correlation of ejectiles from the reaction ^{70}Zn (15 MeV/nucleon) + ^{64}Ni corresponding to the reference silicon detector. Graphical contours are shown on each band corresponding to the charge states q = 25-29 (horizontal bands) of the ejectiles.

3.2.4 Mass Determination and Distributions

We continue with the description of the procedure of mass identification after the reconstruction of the atomic number Z and the charge state q. For the determination of the masses, software gates were set on Z and q for each Si detector used in each experimental run. For given Z and q, the identification technique, as first documented in ref. [53], was adopted. This technique is based in general on the relationship between the kinetic energy of the ions and the magnetic rigidity which can be expressed non relativistically as:

$$B\rho = \frac{1}{\alpha}\frac{\sqrt{A}}{q}\sqrt{2E_{\text{tot}}} \tag{3.26}$$

This relationship expresses a proportionality of $B\rho$ on $\sqrt{E_{tot}}$ with a slope of $\frac{\sqrt{A}}{q}$. Thus, a correlation of $B\rho$ on $\sqrt{E_{tot}}$ or, (for simplicity) on E_{tot} should result on a grouping of the particles in bands of the same $\sqrt{A}/q$. But since in this procedure the value of q is fixed, the bands should correspond to successive masses.

To make the connection with the work of the MAGNEX group, we note that the magnetic rigidity is mainly determined by the position at the focal plane of the spectrometer. Since only a small fraction of the energy is deposited in the gas section, the above relationship is approximately preserved between the two primary measured quantities X_{foc} and E_{resid}, where these two quantities provide the basis of the mass identification as performed in the works of the MAGNEX group.

In the following Figure, a $B\rho$ versus E_{tot} plot of the Zn^{28+} (Z=30, q=28) of events for the reference Si detector is presented. The gap in the $B\rho$ range is due to a gate applied to exclude the intense group of elastic events. In this representation, the selection of the various masses can be performed by setting the respective graphical cuts, as shown for A = 68–72 in the case of Zn^{28+} ejectiles.

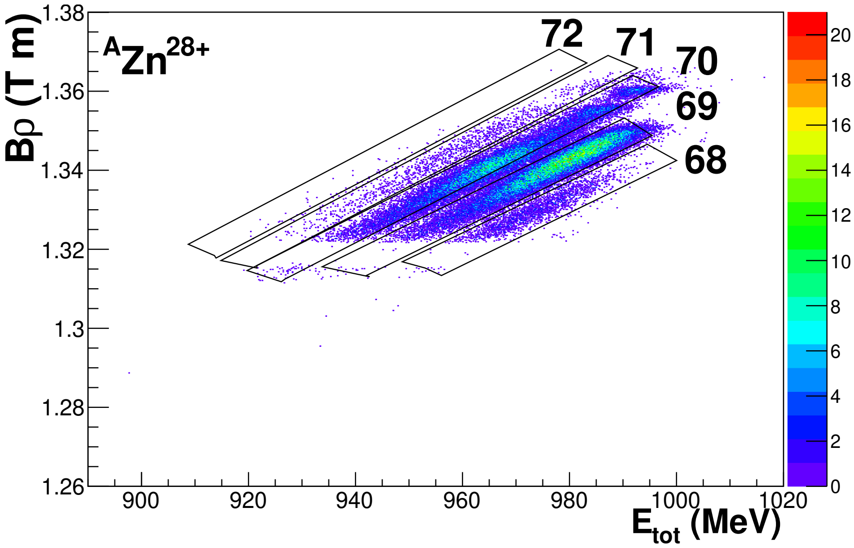

Figure 3.12: Magnetic rigidity vs total energy correlation of ejectiles with Z = 30 and Q = 28 from the reaction ^{70}Zn (15 MeV/nucleon) + ^{64}Ni. The graphical contours represent isotopes of Zn^{28+} (A = 68-72).

However, a crucial issue concerns the correct identification of the bands. The course of action involves the implementation of simulations based once again on the general relationship between the magnetic rigidity and the total kinetic energy of the particles, taking also into account the relativistic expressions. Combining Eq. 3.22 and 3.23 we get:

$$B\rho = \frac{1}{\alpha}\frac{\sqrt{A}}{q}\sqrt{E_{tot}}\sqrt{2m_n c^2 + E_{n,rec}} \tag{3.27}$$

with the last factor $\sqrt{2m_n c^2 + E_{n,rec}}$ being the relativistic correction. The use of

Eq. 3.27 yields the colored lines on the plot below that provide a strong indication of the correct identity of the ejectile mass in the present case.

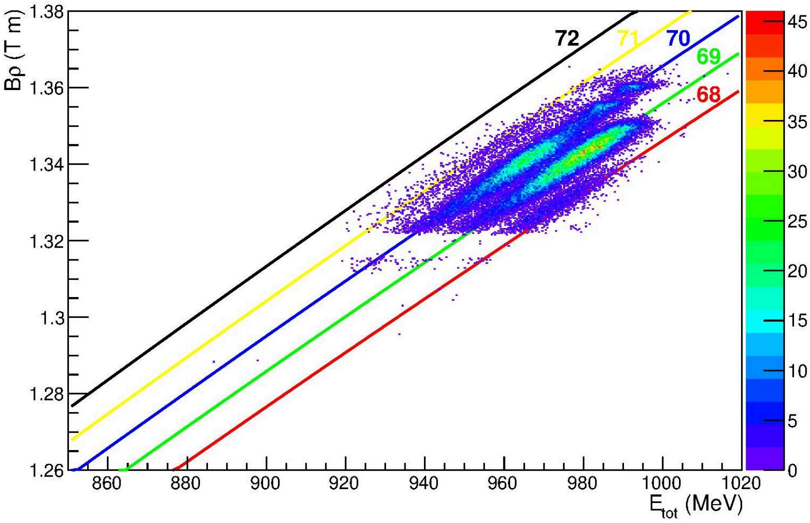

Figure 3.13: Magnetic rigidity vs total energy correlation of ejectiles with Z = 30 and Q = 28 from the reaction ^{70}Zn (15 MeV/nucleon) + ^{64}Ni. The graphical contours represent isotopes of Zn^{28+} (A = 68-72). The colored lines are calculations, obtained from Eq. 3.27.

From this analysis, it is evident that the reconstruction of the ionic charge state is very important. If the PID approach was, for example, based only on the reconstruction of the atomic number Z, then in the $B\rho$ vs E_{tot} correlation, we would not be able to identify products that have (nearly) the same ratio of $\frac{\sqrt{A}}{q}$, but different charge states and masses. (e.g. ^{70}Zn^{29+} yields the same ratio as ^{68}Zn^{28+}).

The next step of the analysis refers to the extraction of momentum and angular distributions, as well as production cross sections. After setting proper graphical cuts in the $B\rho$ versus E_{tot} plot, these cuts are saved for further use. At this point, each cut represents an ejectile of specific Z, q, and A. We remind that in this experiment, seven of the silicon detectors of the FPD of the MAGNEX spectrometer were used. The methodology presented here, concerning the Z, q, and A identification of the ejectiles in the reference detector, has been implemented in all other active Si detectors of the FPD.

After determining the isotopes for each silicon detector in each run, a correlation is obtained between the reaction angle in the lab frame θ_r versus $B\rho$. In the next figure, a typical example of this plot for ejectiles of $Z = 30$, $q = 28+$, $A = 70$

and $Z = 30$, $q = 28+$, $A = 71$ for the reference Si detector are shown.

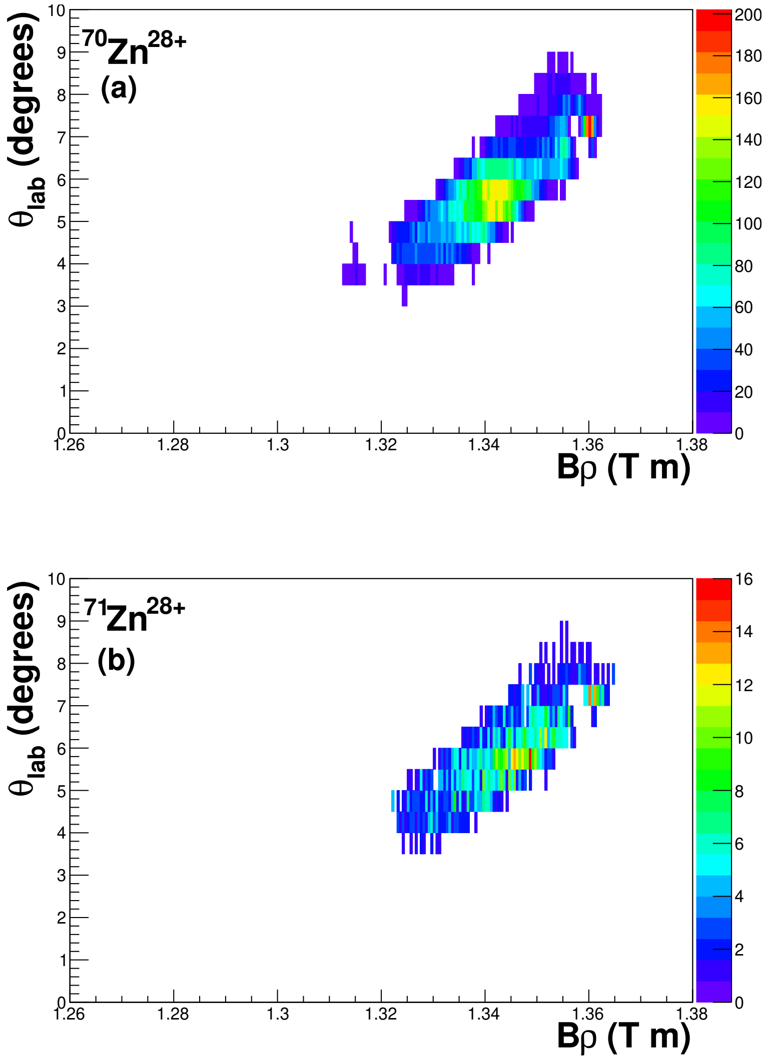

Figure 3.14: Reaction angle in the lab frame (θ_r) vs magnetic rigidity ($B\rho$) plot for ejectiles of $Z = 30$, $q = 28+$, $A = 70$ and $Z = 30$, $Q = 28+$, $A = 71$ for the reference Si detector.

Subsequently, each $\theta_r - B\rho$ distribution was written in a text file with a bin width of $\Delta\theta_r = 0.5°$ and $\Delta(B\rho) = 0.001\,\mathrm{T \cdot m}$. These table files were properly combined with the use of a data analysis program written in Fortran (called `zap.f`) developed in our laboratory.

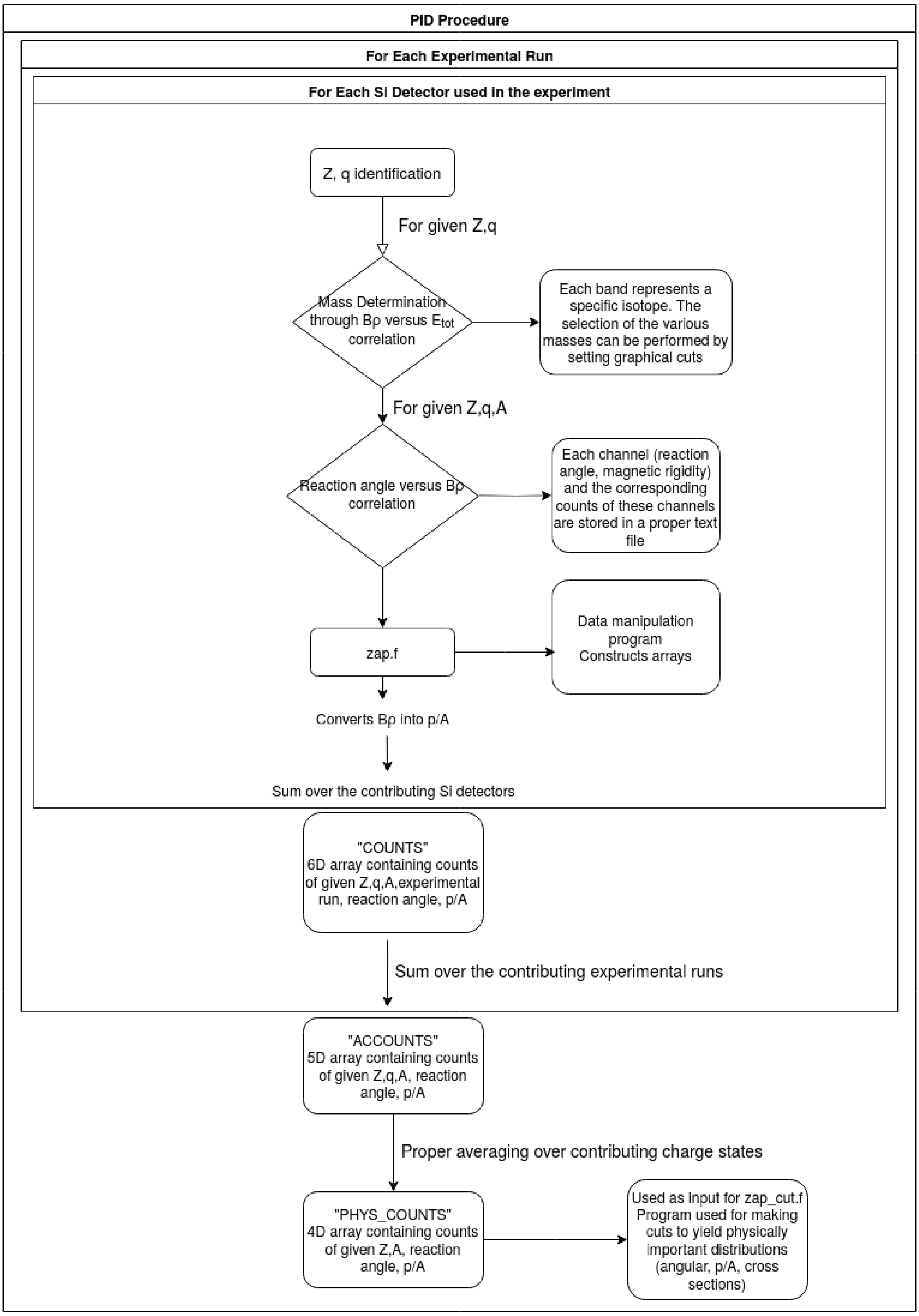

Figure 3.15: A flowchart that outlines the main steps of our procedure from identifying the particles to the point of employing our code zap.f to extract the physics matrix w.r.t Z, A, θ_r, p/A to be used further to obtain physically important distributions (angular, p/A, cross section distributions).

Before presenting what the analysis program `zap.f` does, a brief summary is given for the identification procedure up to this point. For each silicon detector used in each experimental run, a Z and q identification was made. The next step was the correlation of Z vs E_{resid} and q vs E_{resid}, because it was found that it leads to a clear identification and separation by correlating each reconstructed parameter with the experimentally measured observable E_{resid}, effectively taking care of possible dependence of Z and q on E_{resid}. Then, for a given Z and q pair, the masses of the isotopes were identified according to a $B\rho$ versus E_{tot} correlation. Finally, for each isotope identified in Z, q, and A for each Si detector, a reaction angle versus magnetic rigidity correlation was obtained. This $\theta_r - B\rho$ distribution is saved for subsequent analysis.

The program `zap.f` will be now addressed. It is mainly a data manipulation program responsible for combining the analysis results so far to produce various arrays. These arrays are subsequently used as inputs to another program, called `zap_cut.f`, in order to obtain important physics distributions such as angular distributions, momentum distributions, and cross-section distributions. A flowchart of the program is presented in Fig. 3.15.

The analysis procedure to be performed by `zap.f` is controlled by a master file, a part of which is presented in Table 3.1. This file contains information regarding the gates set for a given Z, q, and A on each of the Si detectors. Thus, it provides a complete map of the $\theta_r - B\rho$ distributions that have to be properly combined to obtain the physics distribution of a given isotope Z, A.

IS is an index representing each active Si detector. If the value is equal to zero for a Si detector, that means that the specific isotope was not present in this detector. If the value is equal to its respective number, then this isotope has been identified by the respective Si detector. After reading the master file, the code accesses and reads the $\theta_r - B\rho$ table, then converts the magnetic rigidity to momentum per nucleon p/A using the equation:

$$\frac{pc}{A} = \alpha \, B\rho \left(\frac{q}{A}\right) \tag{3.28}$$

with $\alpha = 299.79 \, \frac{MeV}{T \cdot m}$ and then creates a three-dimensional array, named SiCOUNTS (IS, ITH, IP). This array yields the counts over a given silicon detector and each

Run	IZ	IQ	IA	IS: 1	2	3	4	5	6
41	30	28	67	0	0	14	17	20	0
41	30	28	68	0	11	14	17	20	0
41	30	29	68	0	0	0	17	20	0
41	30	28	69	8	11	14	17	20	0
41	30	29	69	0	0	14	17	20	0
41	30	28	70	8	11	14	17	20	0
41	30	29	70	8	11	14	17	20	0
41	30	28	71	8	11	14	0	0	0
41	30	29	71	8	11	14	17	20	0
41	30	28	72	8	11	0	0	0	0
41	30	29	72	8	11	14	17	0	0

Figure 3.15: Part of the master file (in the form of a table) used by the data manipulation program `zap.f`. This file contains information regarding the gates have been set for a given Z, q, A on each of the Si detectors.

value of the reaction angle θ_r and the momentum per nucleon p/A, respectively. Another array is the so-called COUNTS (IZ, IQ, IA, IRun, ITH, IP). This is a 6D array and is a result of the summation over the contributing silicon detectors for each isotope. It yields the counts for a given value of Z, q, A, experimental run, θ_r and p/A. For a given Z and A, the counts of each contributing run in each bin of θ_r and p/A are properly summed. This procedure gives the array ACCOUNTS (IZ, IQ, IA, ITH, IP). This summation takes place after relative normalization, so that each run corresponds to the same total beam charge on target. Because of this normalization, the obtained counts are thus "normalized" counts.

The next step is to construct the "physics" array PHYSCOUNTS (IZ, IA, ITH, IP) that contains the counts of each isotope Z, A in each bin of θ_r and p/A. For this reason, an appropriate combination is obtained over the contributing charge states for a given p/A, θ_r, as well as A and Z. The averaging of the charge states is done by calculating a parameter called q_{factor}, depending mainly on the equilibrium charge state distribution [74] that we will briefly describe below.

The charge state distribution is due to the stochastic character of the processes of electron capture and loss by the projectile. These processes take place during the interaction (through collisions) of the projectile atoms with the ones of the target. The charge state distribution for a swift highly charged ion beam behind a target foil is characterized by the mean charge, the width, and the shape of the distribution. The equilibrium state is reached at a certain thickness, the so-called equilibrium thickness, due to the equilibration of electron loss and capture processes. Various semi-empirical formulae predicting the mean charge state of heavy ions that are produced from reactions at intermediate energies have been proposed. The semi-empirical equation of Baron [75] that describes the mean charge state for heavy ions passing through thin foils was used in this work, as in all previous works of our group (e.g. [45]). This equation describes the mean charge state as a function of the incoming projectile velocity v_p, the projectile atomic number Z_p, and the target atomic number Z_t as shown below:

$$Q_{\text{mean}} = Z_p \left[1 - \exp\left(-83.275\,\beta Z_p^{0.477}\right)\right] f(Z_p) g(Z_t) \tag{3.29}$$

where $\beta = \frac{v_p}{c}$,

$$f(Z_p) = \left[1 - \exp\left(-12.905 + 0.2124 Z_p - 0.00122 Z_p^2\right)\right] \tag{3.30}$$

and

$$g(Z_t) = \left[1 - 5.21 \times 10^{-3}(Z_t - 6) + 9.56 \times 10^{-5}(Z_t - 6)^2 - 5.9 \times 10^{-7}(Z_t - 6)^3\right] \tag{3.31}$$

where $f(Z_p)$ is a correction term that must be considered for systems where the projectile has an atomic number higher than 54, while $g(Z_t)$ is a correction factor that describes the dependence of the mean charge state on the target atomic number with reference to a C foil ($Z_t = 6$).

By using this formula, we obtain the equilibrium charge state distribution after the stripper, with inputs $Z_t = 6$ and $A_t = 12$, while Z_p and A_p are the atomic number and mass number of the projectile, as well as the various ejectiles as indicated in the master file of our analysis.

Assuming a Gaussian distribution, the width is given by the following equation:

$$d = q_{\text{mean}} \left(0.07535 + 0.19Y - 0.2654Y^2\right) \times 1.1432 \tag{3.32}$$

where $Y = \frac{q_{\text{mean}}}{Z_p}$.

After the calculation of the equilibrium charge state distribution after the stripper and its corresponding width, the subroutine calculates the area of a normalized gaussian distribution that corresponds to a specific charge state q of each event of the array ACCOUNTS (IZ, IQ, IA, ITH, IP). With the total area of the gaussian normalized distribution being equal to 1, the correction factor q_{factor} is equal to the ratio of the area corresponding to the given charge state for a given event over the total area, which is 1. The correction factor q_{factor} essentially provides the correction to the yield of a specific isotope Z,A (at a given velocity p/A) and one charge state q if the others are not taken into account. An average of the corrected counts for each contributing q is then obtained (if more than one q is present) leading finally to the array PHYSCOUNTS (IZ, IA, ITH, IP). This matrix is then written in a text file and will be used for the generation of the angular, p/A and cross section distributions that will be performed with the code `zap_cut.f`, developed also in our lab. The following table is an example of the aforementioned text file. It consists of six rows that represent the atomic number Z, the mass number A, the reaction angle (θ_r), the momentum per nucleon (p/A) and finally the normalized counts and the standard deviation, respectively.

The angular and p/A distributions can now be obtained and eventually the production cross sections of the produced ejectiles can be obtained using the code zap_cut.f developed in our lab. This step is performed with contents of the physics array PHYSCOUNTS (IZ,IA,ITH,IP). In Table 3.2 an example of the matrix file is presented; the row under the name “counts” gives the value of PHYSCOUNTS.

In order to obtain cross sections, the cross section that corresponds to one (normalized) count needs to be calculated. For this reason, a cross section factor

Z	A	θ_r	$\frac{p}{A}$	Counts	Error
30	70	6.5	160.0	523.12	35.60
30	70	6.5	160.5	863.77	51.15
30	70	6.5	161.0	718.59	41.35
30	70	6.5	161.5	623.30	49.54
30	70	6.5	162.0	811.87	53.20
30	70	6.5	162.5	1573.84	85.87
30	70	6.5	163.0	3496.23	109.42
30	70	6.5	163.5	10523.86	156.24
30	70	6.5	164.0	423.13	22.45

Table 3.2: Table presenting part of the physics matrix as explained in the text. The rows represent the atomic number Z, the mass number A, the reaction angle θ_r, the momentum per nucleon $\frac{p}{A}$, and finally the normalized counts and the standard deviation, respectively.

“cs_factor” has been implemented. Through the experiment, the current integrator (CI) was set at 10^{-10} Coulomb/pulse. In other words, during the experiment, 10 pulses were obtained per 1 nC (nano Coulomb). We note that 1nC is equal to $0.624 \cdot 10^9$ particles. For each experimental run, the total number of pulses was recorded. So, from the number of pulses of the current integrator for each experimental run, the beam charge in nC was extracted. By dividing this by the average charge state of the beam that exits the target (taken as q_{mean} = 28+), the “particle” beam charge in particle-nC can be obtained. The cs_factor for each experimental run was calculated based on the known value of the beam’s pnC and the target thickness.

The set of combined runs 41-61 of the runset ”ZnNi” is designated as the ”reference run” and the corresponding beam charge was determined, leading ultimately to the calculation of the cs_factor (mb/count). The extraction of the beam charge pnC for run 41-61 will be presented. Specifically, for run 41-61, the number of pulses was $Q_{live,41} = 111007$, corresponding to a beam charge of $I_{live,41} = 11101$ nC. This calculation allowed the pnC to be determined as:

$$pnC_{41} = \frac{11101}{28} \approx 397\ pnC \tag{3.33}$$

The calculation of the cs_factor (mb/count), of course, comes from the definition of the cross section:

$$
\begin{aligned}
P &= \sigma n x \\
\frac{N}{N_0} &= \sigma n x \\
\sigma &= \frac{N}{N_0}\frac{1}{nx}
\end{aligned}
\tag{3.34}
$$

where nx is the particle number density (particles/mb) expressing the target thickness, N_0 the number of particles of the beam that hit the target during a specific run and N are the counts of a specific product. To obtain the cross section that corresponds to one event, we simply set $N = 1$ in Eq. 3.34 and we obtain the cross section factor:

$$
cs\_factor = \frac{1}{N_0}\frac{1}{nx} \tag{3.35}
$$

For the reference run, we have:

$$
nx = \frac{X_{tgt}}{A_{tgt} \cdot 1000} 6.022 \cdot 10^{23} particles/cm^2 = 0.28125 \cdot 10^{-7} particles/mb \tag{3.36}
$$

where $A_{tgt} = 64$ the mass number of ^{64}Ni target and $X_{tgt} = 1.18 mg/cm^2$ the target thickness. In the last equality we used $1mb = 10^{-27} cm^2$.

For the number of beam particles N_0 we have:

$$
N_{0,41} = pnC_{41} \cdot 0.624 \cdot 10^{-24} \tag{3.37}
$$

where $0.624 \cdot 10^{-24}$ is the number of particles per nC of current, as mentioned earlier. By substituting the results from Eq. 3.36 and 3.37, the cs_factor of run 41-61 for run 41-61 is found to be $cs\_factor_{41} = 3.64 \cdot 10^{-5}\ mb/count$.

For the different runs of the same runset "ZnNi" (runs 22-34, 64-69) with a different $B\rho$ setting of that in the run 41-61, an appropriate normalization with respect to this reference run is needed. These normalization factors were obtained so that the counts of each run times this normalization may correspond to a beam charge equal to that of the reference run. The normalization factor is obtained as:

$$f_i = \frac{Q_{live,41}}{Q_{live,i}} \tag{3.38}$$

where the index i corresponds to the various runs used in this work. For run 64-69, the normalization factor is:

$$f_{64} = \frac{Q_{live,41}}{Q_{live,64}}$$
$$f_{64} = \frac{111007}{80676} = 1.38$$

And for run 22-34, a correction to this normalization was required to account also for the difference in the vertical angular range between this run and the reference run.

$$f_{22} = \frac{Q_{live,41}}{Q_{live,22}}$$
$$f_{22} = \frac{111007}{186778} = 0.595$$

For the run 22-34, the vertical angular range was $\Delta\phi = \pm 0.2°$, while for the runs 41-61, was set at $\Delta\phi = \pm 0.8°$. For this reason, the normalization factor was multiplied by four, to obtain a final factor value of $f_{22} = 2.38$ for run 22-34.

Run	$B\rho\ (Tm)$	$Q_{live}\ (counts)$	Normalization Factor
22-34	1.2880	186778	2.38
41-61	1.2880	111007	1.00
64-69	1.3594	80676	1.38

Table 3.3: Table summarizing the normalization factors for the various runs of the runset ZnNi.

In Table 3.3, we provide an overview of the different runs, along with their respective pulse counts and normalization factors relative to the reference run.

After converting the counts into cross section, the next step was to create the various distributions. In order to extract the angular distribution, the full array was summed over the momentum per nucleon and then written in a distribution of Z, A and θ_r. An example of this type of distribution is given in Table 3.4.

Z	A	θ_r	Counts	Error	σ (mb)	dσ (mb)	dσ/dΩ (mb/msr)	Error of dσ/dΩ
30	70	4.0	28435.44	392.16	1.7699	0.0244	7.254	0.1000
30	70	4.5	29391.58	257.46	1.8294	0.0160	7.498	0.0657
30	70	5.0	39404.41	321.65	2.4527	0.0200	10.052	0.0821
30	70	5.5	59403.50	421.34	3.6975	0.0262	15.154	0.1075
30	70	6.0	32913.95	307.71	2.0487	0.0192	8.396	0.0785
30	70	6.5	20501.93	241.45	1.2761	0.0150	5.230	0.0616
30	70	7.0	6503.65	139.68	0.4048	0.0087	1.659	0.0356
30	70	7.5	2029.72	75.00	0.1263	0.0047	0.518	0.0191
30	70	8.0	769.71	57.28	0.0479	0.0036	0.196	0.0146
30	70	8.5	282.97	44.90	0.0176	0.0028	0.072	0.0115
30	70	9.0	98.88	34.81	0.0062	0.0022	0.025	0.0089
30	70	9.5	12.58	5.38	0.0008	0.0003	0.003	0.0014

Table 3.4: Excerpt of the angular distribution file extracted from the code `zap_cut.f`.

The first two rows represent the atomic number and the mass number, respectively. The third row represents the reaction angle and the next two rows the respective normalized counts and the corresponding error. The sixth row represents the measured cross section, while the eighth row represents the differential angular cross section, $d\sigma/d\Omega$ (mb/msr). This is the result of dividing the measured cross section by the solid angle bin, the latter being calculated from the horizontal and vertical acceptance of the experimental setup. The equation that yields the differential angular cross section is the following:

$$\frac{d\sigma}{d\Omega} = \frac{(\text{counts} \cdot cs\_factor)}{\Delta\Omega} \tag{3.39}$$

where $\Delta\Omega$ is the solid angle element width and cs_factor is the cross section factor as presented before. Specifically, the horizontal angle width is $\Delta\theta = 0.5°$ or $8.7mrad$, while the vertical angle width is $\Delta\phi = 1.6°$ or $27.9mrad$. So, $\Delta\Omega$ is:

$$\Delta\Omega = \frac{\Delta\theta \cdot \Delta\varphi}{1000} = 0.242\,\text{msr} \tag{3.40}$$

An example of an angular distribution can be seen in panel (a) of Fig. 3.16

depicting the inelastic channel (^{70}Zn). The data are shown by solid black circles. The grazing angle of the reaction under study is $\theta_{gr} = 6.5°$. We need to clarify the reason why it is called an 'inelastic' channel. This is because before the implementation of the PID approach, we have effectively excluded by software gating the elastic events that were presented in Fig. 3.2, 3.3 of this work. The general feature of the angular distributions is that they peak near the grazing angle. However, elements further away from the projectile are characterized by a rather monotonically decreasing angular distribution. The subsequent section will offer a more comprehensive discussion, featuring specific examples and detailed results that illustrate these trends in angular distributions.

Moving on to the p/A distributions, the physics array (i.e. Table 3.2) is summed over the reaction angle and then converted to a distribution w.r.t. Z, A and p/A. A typical example of the resulting distribution is shown in Table 3.5. In the current analysis, the extraction of momentum distributions involves summing the angular distributions across the full range of reaction angles. These distributions are then expressed as functions of the atomic number Z, the mass number A, and the momentum per nucleon p/A.

Z	A	p/A	Counts	Error	σ (mb)	dσ (mb)
30	70	158.0	1010.00	75.78	0.0368	0.0028
30	70	158.5	2543.11	90.82	0.0926	0.0033
30	70	159.0	3989.59	107.46	0.1452	0.0039
30	70	159.5	4842.86	123.62	0.1763	0.0045
30	70	160.0	6464.10	138.05	0.2353	0.0050
30	70	160.5	11445.20	194.97	0.4166	0.0071
30	70	161.0	13443.11	207.36	0.4893	0.0075
30	70	161.5	12324.29	187.62	0.4486	0.0068
30	70	162.0	11805.71	159.14	0.4297	0.0058
30	70	162.5	15551.94	163.54	0.5661	0.0060
30	70	163.0	18740.19	189.07	0.6821	0.0069

Table 3.5: Excerpt of the momentum per nucleon distribution file obtained from the code `zap_cut.f`.

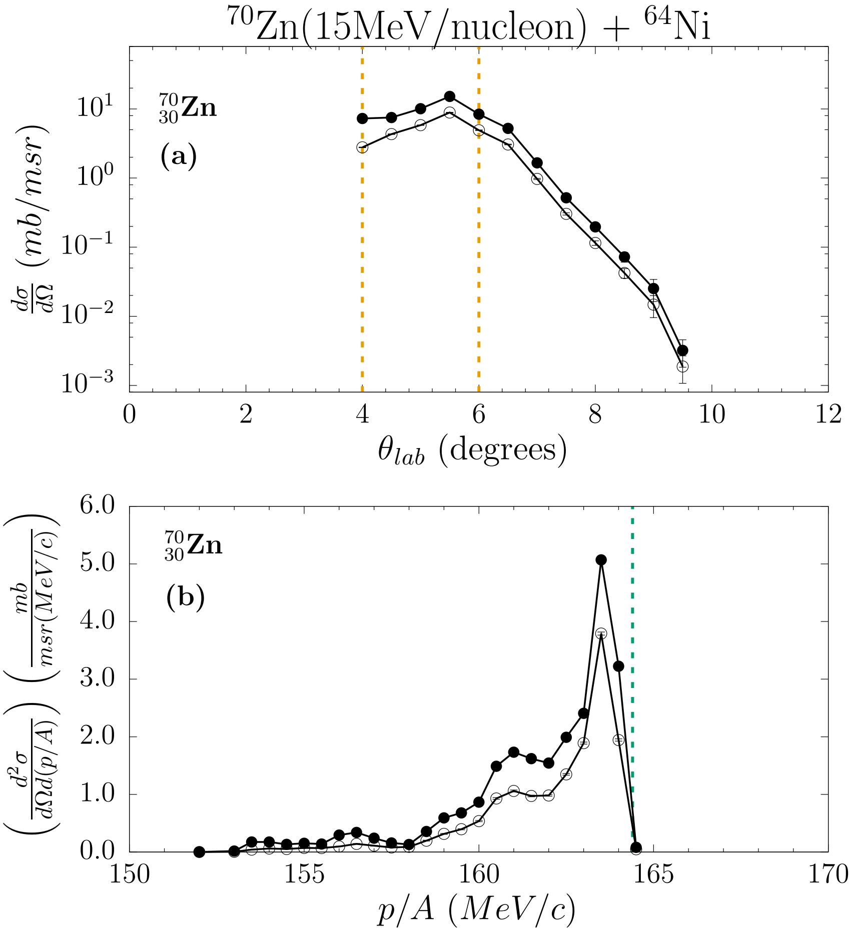

Figure 3.16: (a): Angular distribution of ejectiles from the inelastic channel of the reaction ^{70}Zn (15 MeV/nucleon) + ^{64}Ni. The experimental data in the angular range of $4°$–$15°$ are represented by open circles, while those in the $4°$–$6°$ window are shown by closed circles. The vertical dashed (orange) lines indicate the $4°$–$6°$ angle window. (b): Momentum per nucleon distribution of ejectiles from the inelastic channel. The experimental data in the angular range of $4°$–$15°$ are represented by open circles, while those in the $4°$–$6°$ window are shown by closed circles. The vertical dashed (green) line represents the p/A of the projectile.

A decision was made regarding the horizontal angle interval for integration. For the p/A distributions, we have decided to integrate the angular distribution in the interval $\theta_{lab} = 4° - 6°$, corresponding more closely to the peak of the angular distributions and not on the full observation window $\theta_{lab} = 4° - 15°$. We have verified that if we obtain the p/A distributions of this channel in the full observation window of $\theta_{lab} = 4° - 15°$, the shape of the spectrum remains almost unchanged and the differential cross section is only slightly higher (Fig. 3.16). This is valid for all reaction channels involved in this work. The choice of $\theta_{lab} = 4° - 6°$ is thus motivated by the goal of focusing on the most significant region of the angular distribution where most of the yield lies.

The cross section that we report for the p/A spectra has a bin width of $\Delta(p/A) = 0.5 MeV/c$. Using this differential cross section we obtain the value of $\frac{d^2\sigma}{d\Omega d(p/A)}$ in units of $\frac{mb}{msr(MeV/c)}$. The observation window is presented by the gray rectangle in the sketch presented in Fig. 3.17. The solid angle of this observation window, defined by $\Delta\theta = 2°$ and $\Delta\phi = 1.6°$ is:

$$\Delta\Omega = \left(\frac{2}{57.3\ deg/rad}\right) \cdot \left(\frac{1.6}{57.3\ deg/rad}\right)$$
$$\Delta\Omega = 0.975 \cdot 10^{-3}\ sr = 0.975\ msr$$

The orange disk represents the entire angular range where integration was per-

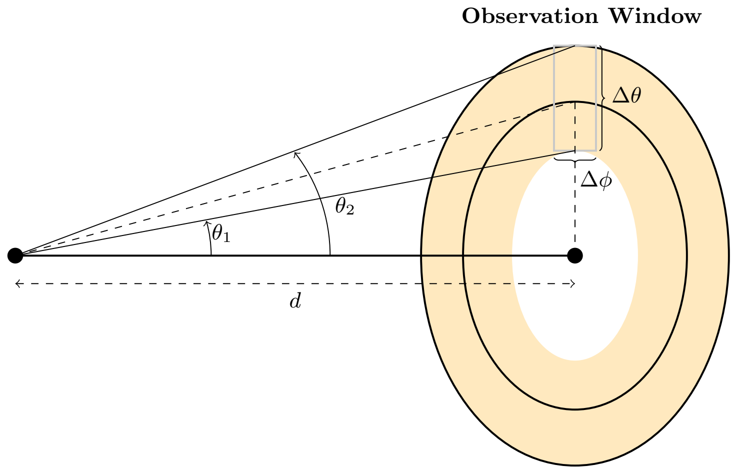

Figure 3.17: Schematic representation of the angular integration ranges and the full azimuthal angle. The orange disk illustrates the full angular range corresponding to $\theta_{lab} = 4° - 6°$. The observation window, highlighted within this range, is defined by $\Delta\theta = 2°$ and $\Delta\phi = 1.6°$, corresponding to a solid angle of $\Delta\Omega = 0.975 msr$ (see text).

formed for the p/A spectra, specifically for $\theta_{lab} = 4° - 6°$. This is the broader region in space where particles are being observed or measured. In simpler terms, the difference between the orange disk and the observation window, is that the latter represents a ”small slice” of the broader orange disk. The solid angle of the orange disk is calculated as follows:

$$\Omega = \frac{S}{d^2} = \frac{\pi(\theta_2 d)^2 - \pi(\theta_1 d)^2}{d^2} = \frac{d^2\pi(\theta_2^2 - \theta_1^2)}{d^2}$$
$$\Omega = \pi\left[\left(\frac{6}{57.3}\right)^2 - \left(\frac{4}{57.3}\right)^2\right] = 0.0191\ sr$$
$$\Omega = 19.1\ msr$$

where S represents the area of the orange disk.

Dividing the solid angle of the orange disk by the solid angle of the observation window yields a scaling factor, denoted as ϕ_{factor} in this work, which is:

$$\phi_{factor} = \frac{\Omega}{\Delta\Omega} = \frac{19.1msr}{0.975msr} = 19.6$$

In the theoretical calculations used in the subsequent analysis, to enable realistic comparisons with the measured data, it was necessary not only to filter the calculations for the angular acceptance window of the experiment and the magnetic rigidity interval 1.260–1.425 T m covered in the experiment, but also to divide the calculations by the scaling factor ϕ_{factor}.

We note that, during the initial phase of the analysis, the experimental data was depicted using a linear scale. This approach provided a visualization of the overall features of the momentum distributions, revealing the presence of two primary regions of interest. However, it became evident that the dissipative region, corresponding to lower values of p/A, characterized by significantly lower cross sections, could not be effectively studied with this representation. The linear scale suppressed important details of the behavior in this region, limiting further insights. For this reason, the next phase of the analysis involved adopting the presentations of the cross sections in logarithmic scale. This approach enabled a more comprehensive analysis, uncovering details about the reaction dynamics as we will discuss in detail in the following chapter.

In regards to the isotope production cross sections (mass distributions), an integration over the momentum per nucleon and subsequently an integration over the angular width was done at the full physics array. For each ejectile (Z,A), the integrated cross section in the whole reaction angle range of $\theta_r = 4 - 15°$ is obtained as:

$$\sigma = \int \frac{d\sigma}{d\Omega} d\Omega = 2\pi \int \frac{d\sigma}{d\Omega} \sin\theta \, d\theta = 2\pi \sum_{\theta_i=4°}^{15°} \frac{d\sigma}{d\Omega} \left(\sin\left(\frac{\theta \cdot \pi}{180°} \right) \right) \frac{\Delta\theta \cdot \pi}{180°} \tag{3.41}$$

where θ is in degrees and $\Delta\theta$ = 0.5°, is the experimental bin of the polar angle.

The flowchart shown below (Fig. 3.18), schematically presents the procedure followed by the code `zap_cut.f` for the extraction of the angular and p/A distributions, as well as the isotope production cross sections.

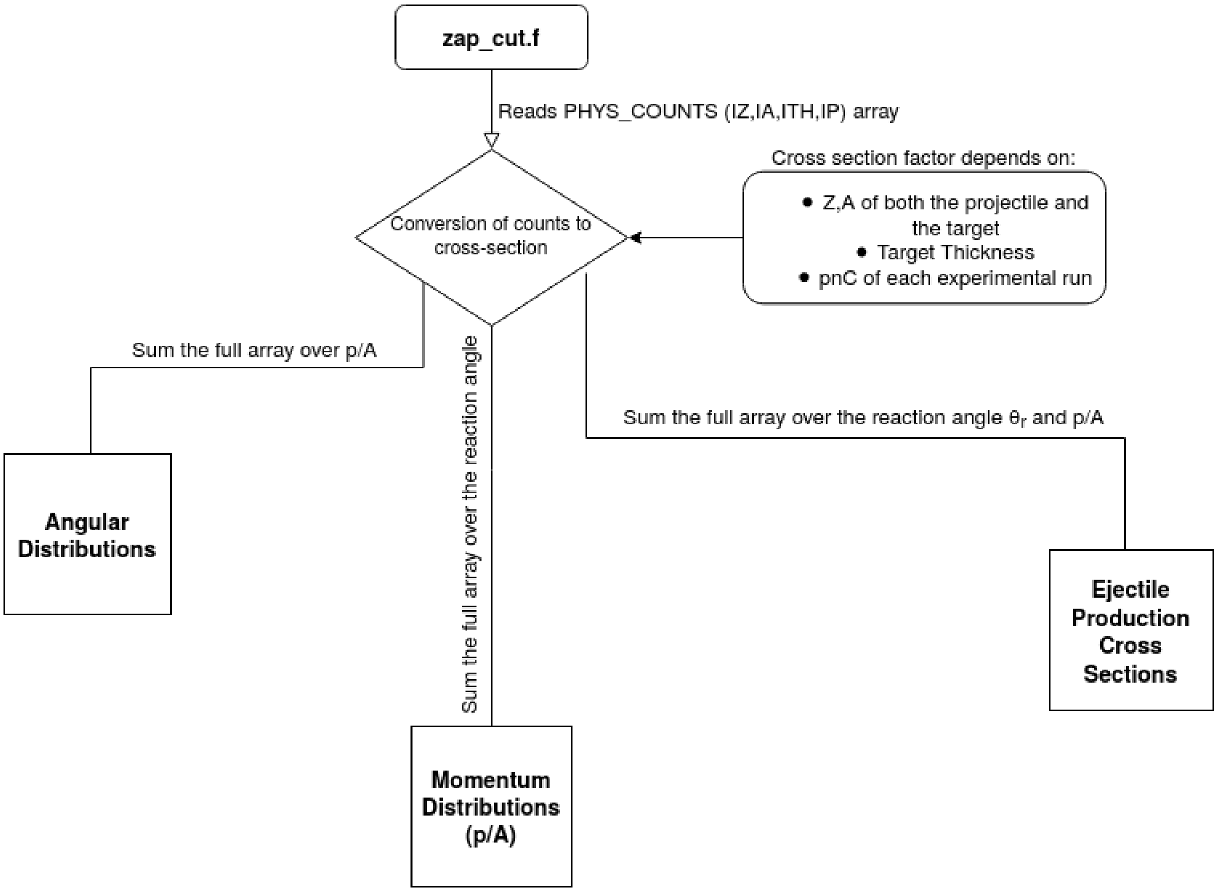

Figure 3.18: A flowchart that outlines the main distributions obtained from the code `zap_cut.f`

Summarizing, in this chapter, the data analysis methodology employed to extract ejectile distributions from the reaction of ^{70}Zn at 15 MeV/nucleon with ^{64}Ni using the MAGNEX spectrometer was outlined. A systematic approach was developed to reconstruct the atomic number Z and the ionic charge state q of the ejectiles, utilizing the measured and calibrated quantities of energy loss, residual energy, and time-of-flight (TOF). This was followed by a correlation of the magnetic rigidity with the total kinetic energy to identify the various masses of the ejectiles. Subsequently, a correlation between magnetic rigidity and the reaction angle was used for a given set of Z, Q, and A values. These steps, along with the implementation of two data manipulation programs allowed for the extraction of important distributions such as production cross sections, angular distributions, and momentum-per-nucleon distributions.

In the following chapters, the results from various reaction channels will be thoroughly presented and discussed. These results will be further examined, and insights will be drawn regarding the reaction mechanisms. Comparisons with two theoretical models, the phenomenological DIT model and the microscopic CoMD model, combined with the statistical de-excitation code GEMINI, will help in interpreting the observed distributions.

Chapter 4
Theoretical Models

4.1 Introduction

A significant and integral part of basic research in nuclear science has been the development of theoretical models for describing and interpreting the experimental data. These models, through various approaches and appropriate parameterizations offer insights into the reaction mechanisms that are dominant in various nuclear processes. However, continuous and stringent verification of their reliability and general optimizations in line with the latest developments observed in the international literature are required. This chapter will present the models that were used in the present work. The calculations are based on a standard two-stage Monte Carlo approach. In the first, dynamical stage, the interaction between the projectile and the target was described by two theoretical models: the phenomenological DIT model and the microscopic CoMD model, while the deexcitation of the primary fragments was described by the GEMINI code. The models utilized in this study will be outlined below.

4.2 Deep Inelastic Transfer Model (DIT)

The DIT (deep-inelastic transfer) model [76] is a phenomenological model designed to describe peripheral collisions in the Fermi energy domain. The nucleon transfer results in the gradual energy dissipation of the dinuclear system towards internal degrees of freedom and the conversion of the relative kinetic energy into internal excitation of the produced fragments. The resulting excitation of the system can be of rotational, vibrational, or thermal nature [51, 77]. An important aspect to be taken into account for the understanding of multinucleon transfer reactions is how the excitation energy is distributed between the two interacting nuclei. In general, in a phenomenological treatment of deep-inelastic reactions [78, 79], the projectile-target system is treated as a unified entity: collective variables are assumed to evolve through their simultaneous interaction with a thermal reservoir, which is in complete thermal equilibrium. This basic assumption therefore requires the dinuclear system to be characterized by a common temperature. However, this requirement presupposes that the distribution of excitation energy among the various products is based on the mass of each product. On the other hand, in the theory of nucleon exchange, the same behavior is not followed because excitation originates from nucleon transfers. Therefore, if the relative flow is approximately symmetric, the same behaviour will be noticed to the excitation energy of each pair of products. If the nucleon exchange is the dominant reaction mechanism, the energy dissipation of the system will tend to an equal distribution among the reaction products. Thus, in the case of a highly asymmetric system, the light fragment will have a higher temperature [51].

The direction and the type of transfer is determined by random selection based on transfer probabilities. The probabilities are calculated through an integral over phase space taking into account effects such as Pauli blocking. Both the projectile and the target are assumed to be spherical and approach each other along Coulomb trajectories until they are within the range of the nuclear interaction. Then, the system is represented as two Fermi gases in contact allowing the stochastic exchange of nucleons through a “window” that opens between the touching nuclear surfaces. Specifically, a ”window” opens in the nuclear potential, and nucleon transfer takes place stochastically. These nucleon transfers are responsible for the gradual dissipation of the kinetic energy of relative motion into internal excitation and collective rotation of the primary fragments. The stochastic nucleon exchange as described in this model, leads ultimately to a broad distribution of produced fragments in terms of mass, atomic number, spin and excitation energy. These transfers generate dissipation and fluctuations. In the model, this aspect is simulated by random drawing followed by a Monte Carlo [80] method which allows the computation of any observable on an event-by-event basis. After interaction of the dinuclear system, the primary fragments are excited and move along Coulomb trajectories. In this work, the DIT code was run with its standard parameters in the impact parameter range b = 4–12 fm. After separation, the two primary fragments, namely, the excited projectile-like and target-like fragments—that we also call, respectively, quasiprojectile (QP) and quasitarget—share approximately equally the total excitation energy.

It is emphasized that DIT assumes that the only source of energy dissipation is the exchange of nucleons. Collisions between nucleons are not taken into account.

Subsequently, we present a more quantitative discussion of the nucleon exchange process performed by DIT.

4.2.1 Description of the model

Before beginning the analysis of the model, we give some clarifications. Initially, the nucleus donating nucleons will be denoted as 1, and the recipient nucleus as 2. Additionally, the prime symbol ’ will be placed on any quantity related to the system after the completion of nucleon transfer.

Due to energy conversation for the system under study, the equation for the variations of different kinds of energy is the following:

$$\Delta\delta_1 + \Delta\delta_2 + \Delta E_1^* + \Delta E_2^* + \Delta K + \Delta U_{int} = 0 \tag{4.1}$$

The first two terms represent the variations of the mass excesses of the two nuclei in their ground states, as deduced from mass tables. Specifically:

$$\Delta\delta_1 = \delta_1^{'} - \delta_1 = S_1 - \delta_\alpha \tag{4.2}$$

$$\Delta\delta_2 = \delta_2^{'} - \delta_2 = -(S_2^{'} - \delta_\alpha) \tag{4.3}$$

$$\Delta\delta_1 + \Delta\delta_2 = S_1 - S_2^{'} \tag{4.4}$$

where δ_α is the mass excess of the exchanged nucleon and S_1, $S_2^{'}$ the neutron (or proton) separation energy from nuclei 1 and 2 before and after the transfer, respectively.

The terms ΔE_1^*, ΔE_2^* are related with the excitation energy, which includes the rotational degress of freedom:

$$\Delta E_1^* = E_1^{*'} - E_1^* = \epsilon_{F1} - \epsilon_1 \tag{4.5}$$

$$\Delta E_2^* = E_2^{*'} - E_2^* = \epsilon_2 - \epsilon_{F2'} \tag{4.6}$$

where ϵ_1 and ϵ_2 are the kinetic energies of the transferred nucleon referred to nuclei 1 (donor) and 2 (recipient); ϵ_{F1} and $\epsilon_{F2'}$ are the Fermi energy levels, the prime sign labelling the nucleus 2 after it received the transferred nucleon. The last two terms of Eq. 4.1 represent the variations of relative kinetic and potential energy of the composite system, this last quantity being significant only for proton transfers due to the long-range Coulomb interaction.

At this point, considering that the neutron/proton separation energy and the Fermi energy level are linked as quantities with the depth of the potential well at infinity through the relation $S_i + \epsilon_{Fi} = U_{i\infty}$:

$$\Delta\delta_1 + \Delta\delta_2 = (\epsilon_{F1} - \epsilon_{F2'}) + (U_{2\infty} - U_{1\infty}) \tag{4.7}$$

thus Eq. 4.1 becomes:

$$\Delta K = -\Delta U_{int} - (\epsilon_2 - \epsilon_1) + (U_{2\infty} - U_{1\infty}) \tag{4.8}$$

where ΔK is the relative change in kinetic energy and ΔU_{int} the relative change of the dynamic energy of the dinuclear system. Requiring the potential wells of the two nuclei to be of the same depth, it follows that:

$$\Delta K = -\Delta U_{int} - (\epsilon_2 - \epsilon_1) \tag{4.9}$$

It is emphasized at this point that ΔU_{int} in DIT takes a nonzero value only when the transferred nucleon is a proton, due to the strong Coulomb interaction experienced by the system. If a neutron is transferred, it holds: $\Delta U_{int} \approx 0$. ΔU_{int} is given by the following equation:

$$\Delta U_{int} = 1.44 \frac{Z_1 - Z_2 - 1}{d} \tag{4.10}$$

where d represents the distance between the interacting nuclei measured in fm.

We will now move on to the quantities of angular momentum and spin. The angular momentum is examined only through the components that are perpendicular to the reaction plane (meaning the z-axis projections). This is due to the fact that in DIT, the y-axis is considered as the beam axis, instead of the z-axis which is usually considered in describing the kinematics of reactions. Now, if s_1 and s_1 are the spins of the donor and receiver nuclei respectively, and L is the orbital angular momentum, it holds that:

$$\Delta s_1 = -l_1 \tag{4.11}$$

$$\Delta s_2 = l_2$$

$$\Delta L = -(l_2 - l_1)$$

where l_1, l_2 represents the orbital angular momentum of the exhanged nucleon with respect to the donor and recipient nucleus.

As already mentioned in the beginning of this section, when the projectile comes within the range of effective nuclear interaction, a window opens at the surface between the two interacting systems to achieve a stochastic nucleon transfer. According to Randrup [81], the velocity of the nucleon while reaching the recipient nucleus depends not only on its initial velocity, but also on the relative velocity of the dinuclear system, meaning:

$$\mathbf{u_2^{'}} = \mathbf{u_1} + \mathbf{V_{rel}} \tag{4.12}$$

An important quantity examined in DIT is the transfer probabilities. The probability of transferring a nucleon from nucleus 1 to nucleus 2 is given by the equation:

$$P = \int \Phi T n_1 (1 - n_2) d^5\sigma \tag{4.13}$$

where $d^5\sigma = rdrd\theta d^3p$ and $rdrd\theta$ represents the area of an infinitesimal sector in polar coordinates.

Flux (Φ) is defined as the number of nucleons passing through a perpendicular surface per unit time:

$$\Phi = \frac{dN}{dSdt} \tag{4.14}$$

by multiplying both numerator and denominator with dx, we have the following:

$$\frac{dN}{dSdx}\frac{dx}{dt} = \rho_F * u_x \tag{4.15}$$

with ρ_F being the density of the Fermi level. Because DIT refers to phase space, it is known that a phase cell of two nucleons occupies a volume of h^3, therefore:

$$\frac{dN}{dVd^3p} = \frac{2}{h^3} \tag{4.16}$$

$$\rho_F = \frac{2}{h^3} d^3p$$

By combining Eq. 4.14 and 4.16, the number of nucleons passing through an infinitesimal surface dS is:

$$\Phi dS = \frac{2}{h^3} d^3p u_x dS = \frac{2}{h^3} u_x rdrd\theta d^3p \tag{4.17}$$

thus, 4.13 becoming:

$$P = \int \frac{2}{h^3}\ u_x\ r\ T\ n_1\ (1 - n_2)\ dr\ d\theta\ d^3p \tag{4.18}$$

with T being the transmission coefficient, which depends on the potential of the particle in the transfer window, calculated as the sum of the Woods-Saxon and Coulomb potentials. For the calculation of T, the Hill-Wheeler equation for parabolic potential barriers was employed [76]. Finally, n_1 and n_2 represent the probabilities of occupation of an energy level of the donor and recipient nucleus, respectively.

In a nuclear reaction, the quantity of interest is the cross section, which is calculated for a given value of angular momentum as follows:

$$\sigma_l = \pi \bar{\lambda}^2 (2l + 1) P \tag{4.19}$$

where $\bar{\lambda} = \frac{\hbar}{p}$ is the De-Broglie wavelength and P the transfer probability. The total cross section is the following:

$$\sigma_{tot} = \pi \bar{\lambda}^2 \sum_{l=0}^{l_{max}} (2l + 1) P \tag{4.20}$$

Under the assumption that the transfer is successful, meaning $P = 1$, it yields:

$$\sigma_{tot} = \pi \bar{\lambda}^2 l_{max} \tag{4.21}$$

where l_{max} is the maximum value of orbital angular momentum, in which a successful nucleon transfer takes place.

In DIT, for each angular momentum value l, a number of events is generated. The model assumes that these events have to be evenly distributed across the entire target surface. This uniform distribution is achieved by considering the target's cross-section to be circular and perpendicular to the beam axis and also selecting a number of events that is proportional to the radius of the circle. In this case, the radius of the circular target coincides with the impact parameter, upon which both the angular momentum and cross-section depend.

Based on a semiclassical approach, the impact parameter (b), is related to angular momentum as follows:

$$b = \bar{\lambda} l \tag{4.22}$$

In order to achieve a uniform distribution of events, it is assumed that for each l, a number of events proportional to l is chosen that is:

$$n(l) = f_n l \tag{4.23}$$

where f_n is an integer number. Thus, the max number of events will be:

$$N = \sum_{l=0}^{l_{max}} n(l) \approx \frac{f_n l_{max}^2}{2} \tag{4.24}$$

The cross section for a specific reaction channel where a number of n events is generated is:

$$\sigma = \sigma_{tot} \frac{n}{N} \tag{4.25}$$

By combining the equations 4.21, 4.23 with 4.25 it yields the cross section per event ($mb/event$), which is independent of the angular momentum, that is:

$$\frac{\sigma}{n} = \pi \bar{\lambda}^2 \frac{2}{f_n} \tag{4.26}$$

From equation 4.26, it is understood that with a proper adjustment of the value of f_n, events with very low cross-sections can be generated.

4.3 CoMD

The CoMD (constrained molecular dynamics) model [82, 83] is a microscopic model designed for heavy-ion nuclear reactions from the Coulomb barrier to the Fermi energy and above. The code is based on the general approach of quantum molecular dynamics (QMD) [84] describing the nucleons as localized Gaussian wave packets that interact via an effective nucleon-nucleon interaction. In this model, the enforcement of the Pauli principle is achieved via a phase space constraint at each step of the time evolution of the system. The wavefunction of the i-th nucleon is expressed as:

$$\phi_i = \frac{1}{(2\pi\sigma^2{}_r)^{3/4}} exp\left[\frac{-(\mathbf{r} - \langle\mathbf{r_i}\rangle)^2}{2\sigma^2{}_r} + \frac{i}{\hbar}\mathbf{r}\cdot\langle\mathbf{p_i}\rangle\right] \tag{4.27}$$

where $\langle r_i \rangle$ and $\langle p_i \rangle$ are the centroids of position and momentum of the i-th nucleon, respectively. The total wavefunction of the N-body system is expressed as the product of the individual wavefunctions, as follows:

$$\Phi = \prod_i \phi_i(\mathbf{r}) \tag{4.28}$$

As is well known, the formulation of quantum mechanics does not allow for the simultaneous determination of the position and momentum of a particle. Through the Fourier transformation it allows the interchange between representations in position and momentum space; In the theoretical study of nuclear structure and nuclear reactions, the existence of a probability distribution for the positions and momenta of nucleons is necessary. For this reason, CoMD employs an alternative formulation of quantum mechanics, based on phase space, which relies on the Wigner transformation. The phase-space distribution function as obtained by the Wigner transformation of ϕ_i, and with the Gaussian function yields the following equation:

$$f_i(\mathbf{r},\mathbf{p}) = \frac{1}{\pi^3\hbar^3}\exp\left[-\frac{(\mathbf{r}-\langle\mathbf{r}_i\rangle)^2}{2\sigma_r^2} - \frac{2\sigma_r^2(\mathbf{p}-\langle\mathbf{p}_i\rangle)^2}{\hbar^2}\right] \tag{4.29}$$

so for the N-body phase space distribution function it yields:

$$f(\mathbf{r},\mathbf{p}) = \sum_i f_i(\mathbf{r},\mathbf{p}) \tag{4.30}$$

By taking into consideration the momentum width σ_p, the phase-space distribution function takes the final form:

$$f_i(\mathbf{r},\mathbf{p}) = \frac{1}{(2\pi\sigma_r\sigma_p)^3} \exp\left[-\frac{(\mathbf{r}-\langle\mathbf{r_i}\rangle)^2}{2\sigma^2{}_r} - \frac{(\mathbf{p}-\langle\mathbf{p_i}\rangle)^2}{2\sigma^2{}_p}\right] \tag{4.31}$$

The Gaussian description of the wavefunctions in the time dependent Schrödinger's equation for N particles leads into Hamilton's equations of motion for the centroids of the wavepackets. The Hamiltonian $\mathcal{H}$ of the system for A particles with mass m consists of the kinetic energy, the effective nucleon-nucleon interaction and a constant term resulting from the Gaussian width in momentum space, which is not taken into consideration in the context of the formalism of the CoMD code [82].

$$\frac{d}{dt}\langle\mathbf{p_i}\rangle = -\frac{\partial\mathcal{H}}{\partial\langle\mathbf{r_i}\rangle} \tag{4.32}$$

$$\frac{d}{dt}\langle\mathbf{r_i}\rangle = \frac{\partial\mathcal{H}}{\partial\langle\mathbf{p_i}\rangle} \tag{4.33}$$

$$\mathcal{H} = \sum_i \frac{\langle\mathbf{p_i}\rangle^2}{2m} + V_{eff} + A\frac{3\sigma_p^2}{2m} \tag{4.34}$$

The second term (V_{eff}) is the potential part of the Hamiltonian and is based on Skyrme-like interactions along with a surface term. The potential energy involves the following individual terms:

$$V = V^{vol} + V^{surf} + V^{coul} + V^{sym} + V^{(3)} \tag{4.35}$$

$$V^{vol} = \langle \hat{V}^{vol} \rangle = \frac{T_0}{2\rho_0} \sum_{i=1, j\neq i}^{A} \rho_{ij}$$

$$V^{surf} = \langle \hat{V}^{surf} \rangle = \frac{C_s}{2\rho_0} \sum_{i=1, j\neq i}^{A} \nabla^2_{\langle \vec{r}_i \rangle} \rho_{ij}$$

$$V^{coul} = \langle \hat{V}^{coul} \rangle = \frac{e^2}{2} \sum_{i=1, j\neq i}^{A} \frac{1}{\| \langle \mathbf{r_i} \rangle - \langle \mathbf{r_j} \rangle \|} \left(\frac{\| \langle \mathbf{r_i} \rangle - \langle \mathbf{r_j} \rangle \|}{2\sigma_r} \right)$$

$$V^{sym} = \langle \hat{V}^{sym} \rangle = \frac{a_{sym}}{2\rho_0} \sum_{i=1, j\neq i}^{A} \left(2\delta_{\tau_i, \tau_j} - 1 \right) \rho_{ij}$$

$$V^{(3)} = \langle \hat{V}^{(3)} \rangle = \frac{T_3}{\rho_0^{\mu} (\mu + 1)} \sum_{i=1, j\neq i}^{A} \rho_{ij}^{\mu}$$

where $\rho_{ij} = \int \rho_i (\mathbf{r_i}) \rho_j (\mathbf{r_j}) \delta (\mathbf{r_i} - \mathbf{r_j}) d^3\mathbf{r_i} d^3\mathbf{r_j}$ is the superposition integral (or interaction density) which describes the interaction between the i-th and j-th nucleons. This integral expresses the density of two nucleons i and j as a function of their positions r_i and r_j, where the delta function $\delta (\mathbf{r_i} - \mathbf{r_j})$ enforces the condition that the nucleons are at the same position, ensuring that the interaction density is only non-zero when the nucleons overlap spatially. While $\rho_i = \int f_i (\mathbf{r}, \mathbf{p}) d^3\mathbf{p}$ represents the position-dependent density of the i-th nucleon and τ_i corresponds to the z-component of the isospin degree of freedom. The parameters of the effective interaction were as in the recent works of [49, 85] and correspond to a compressibility of K=254 MeV.

In this model a constraint is imposed in order to effectively restore the Pauli principle at each time step of the evolution of the system. This constraint restores, in a stochastic way, the fermionic nature of the nucleon motion in the evolving nuclear system. The requirement for this constraint, is:

$$\bar{f}_i \leq 1 \tag{4.36}$$

$$\bar{f}_i \equiv \sum_j \delta_{\tau_i,\tau_j}\delta_{s_i,s_j}\int_{h^3} f_j(\mathbf{r},\mathbf{p})d^3\mathbf{r}d^3\mathbf{p} \tag{4.37}$$

where s_i,τ_i the z component of the spin and isospin of nucleon i, respectively. The integration is performed in a hypercube of volume h^3 in phase space centered around the point $(\langle\mathbf{r_i}\rangle, \langle\mathbf{p_i}\rangle)$, in the **r** and **p** space, respectively. For each particle i and for each time step, the phase space occupation $\bar{f}_i$ is checked. If the value is greater than 1, an ensemble K_i of nearest particles within distances $3\sigma_r$ and $3\sigma_p$, is determined. Then, for the particles in the ensemble, the momenta are changed in a way that the total momentum is conserved. The new configuration will be accepted only if f_i is reduced below 1; otherwise, the iteration of the process continues until the constraint is achieved.

The short range nucleon-nucleon interactions are described as individual nucleon-nucleon collisions governed by the nucleon-nucleon scattering cross section, the available phase-space and the Pauli principle. For each collision, the occupation probability is checked and the collisions with $\bar{f}_i < 1$ are accepted, in accordance with the Pauli constraint as discussed above (Pauli blocking). Within the Gaussian wavepacket representation, it is found necessary to empirically scale the occupation fraction $\bar{f}_i$ by employing a mass-dependent Pauli constraint parameter ($paulm$), taking the value $paulm = 94$ for the mass range of interest in this work. The occupation constraint f_i becomes [49, 85]:

$$\bar{f}_i \rightarrow \frac{128}{paulm}\bar{f}_i \tag{4.38}$$

For the CoMD calculations presented in this work, the impact parameter range b = 4-12 fm was covered and the dynamical evolution of the system was stopped at t = 600 fm/c (2×10^{-21} s), which is adequate time for the completion of the dynamical stage of nucleon transfer without allowing considerable de-excitation of the hot primary fragments.

4.4 GEMINI

After the dynamical stage of the reaction, described by either of the above two models, the deexcitation of the primary fragments was described by the GEMINI code. GEMINI is a statistical deexcitation code that implements Monte Carlo techniques and the Hauser-Feshbach formalism to calculate the probabilities for fragment emission with Z≤2 [86, 87, 38]. Heavier fragments may be emitted with probabilities following a transition state formalism. The final partition of products is generated by a succession of binary decays.

In general, the de-excitation of an excited nucleus is based on probabilities. As a result, the de-excitation distribution of a nucleus (Z_0, A_0) into a final product (Z_1, A_1) can be calculated using the Breit-Wigner resonance formula:

$$P = \frac{2J_R + 1}{(2J_0 + 1)(2J_1 + 1)} \cdot \frac{\Gamma^2}{(E - E_R)^2 + \frac{\Gamma^2}{2}} \tag{4.39}$$

In the above relation, J_R and E_R express the spin and resonance energy, respectively, while Γ represents the decay width, which is related to the average lifetime τ of the decaying state by the relation $\Gamma\tau = \hbar$. The decay width Γ is expressed as:

$$\Gamma = \frac{2\pi}{\hbar}|V'_{fi}|^2\rho(E_f) \tag{4.40}$$

based on Fermi's golden rule.

For fragments with $Z \leq 2$, the energy width of decay Γ is calculated following the Hauser-Feshbach formalism. The process followed for the de-excitation of these nuclei is called evaporation.

Considering an excited system (Z_0, A_0) with spin J_0, which decays by emitting a particle (Z_1, A_1) with spin J_1 and transitions to a final state (Z_2, A_2) with spin J_2, the decay amplitude can be given by the relation:

$$\Gamma_{J_2}(Z_1, A_1, Z_2, A_2) = \frac{2J_1+1}{2\pi\rho_0} \sum_l \int_0^{E^*-B-E_{rot}(J_2)} T_l(\epsilon)\rho_2(U_2, J_2) d\epsilon \tag{4.41}$$

where the summation spans from $l_{min} = |J_0 - J_2|$ to $l_{max} = J_0 + J_2$ and l and ϵ are the angular momentum and kinetic energy of the emitted particle, ρ_0 and $\rho_2(U_2, J_2)$ are the density of states of the emitted particle and the residual nucleus, respectively, and U_2 is the thermal excitation energy:

$$U_2 = E^* - B - E_{rot}(J_2) - \epsilon \tag{4.42}$$

Here, B denotes the binding energy and E_{rot} is the rotational energy of the final system. The transmission coefficient $T_l(\epsilon)$ is defined as:

$$T_l(\epsilon) = \begin{cases} 0 & \epsilon \leq E_{coul} + \frac{\hbar^2 l(l+1)}{2\mu R^2} \\ 1 & \epsilon > E_{coul} + \frac{\hbar^2 l(l+1)}{2\mu R^2} \end{cases} \tag{4.43}$$

where R is the absorptive radius and μ is the reduced mass of the emitted particle - residual energy system.

For the description of the de-excitation of heavier fragments with $A \geq 12$, the transition state formalism of Moretto is applied, which is based on the formation of a saddle point. The decay width Γ is calculated as follows:

$$\Gamma(Z_1, A_1, Z_2, A_2) = \frac{1}{2\pi\rho_0} \int_0^{E^*-E_{\text{sad}}(J_0)} \rho_{\text{sad}}(U_{\text{sad}}, J_0)\, d\epsilon \tag{4.44}$$

with $T_l(\epsilon) = 1$. Here, ρ_{sad} and U_{sad} denote the density of states and the thermal excitation energy at the saddle point, respectively:

$$U_{sad} = E^* - E_{sad}(J_0) - \epsilon \tag{4.45}$$

The density of states is given by:

$$\rho(U, J) = (2J + 1) \left(\frac{\hbar^2}{2I} \right)^{3/2} \left(\frac{\sqrt{a}}{12U^2} \right) e^{2\sqrt{aU}} \tag{4.46}$$

where $a = 8.5$ MeV^{-1} is the level density parameter and I is the moment of inertia of the final system. The above expression for the density of states arises from the Fermi gas theory.

The implementation of GEMINI in our work was performed with its standard parameters as in the original works of [86, 87].

We close this chapter by noting that, within the context of this work, the two-stage DIT/GEMINI and CoMD/GEMINI calculations will be referred to as DIT and CoMD calculations, respectively.

Chapter 5
Results and Discussion

5.1 Introduction

In this chapter, we present the experimental results of ejectile distributions from the reaction of ^{70}Zn with ^{64}Ni at 15 MeV/nucleon obtained from the analysis described in Chapter 3. Further on, we proceed with a comparison of the experimental data with theoretical calculations employing the models presented in Chapter 4.

We remind at this point that the analysis of the data resulted in ejectile distributions (differential cross sections) with respect to Z, A, θ_{lab} and p/A. In order to have an overall perspective of the distributions for most of the isotopes analyzed, two-dimensional distributions of p/A versus θ_{lab} are presented in Fig. 5.1. These plots – that will be referred to as Wilczynski plots in this discussion – are essentially equivalent to the traditional Wilczynski plots. The latter are plots of kinetic energy vs scattering angle widely used in the study of deep-inelastic collisions near and above the Coulomb barrier providing information on energy dissipation and the dynamical behavior of the dinuclear complex [38, 88, 89]. In the plots of Fig. 5.1, the horizontal lines represent the projectile p/A=164.4 MeV/c, and the vertical lines indicate the grazing angle θ_{gr} $\simeq$6.5° of the ejectiles of the reaction [96]. The various channels are marked by the number of neutrons or protons added or removed from the projectile. For orientation, the channel of ^{70}Zn, corresponding to no net nucleon transfer, called the "inelastic" channel, is displayed in the middle panel. In most of the channels, the existence of a peak (a "band") is evident near the velocity of the beam (quasielastic peak) and an extended region of lower velocities corresponding to more dissipative events, as it will be discussed in further detail later. In addition, in most of the channels, char-

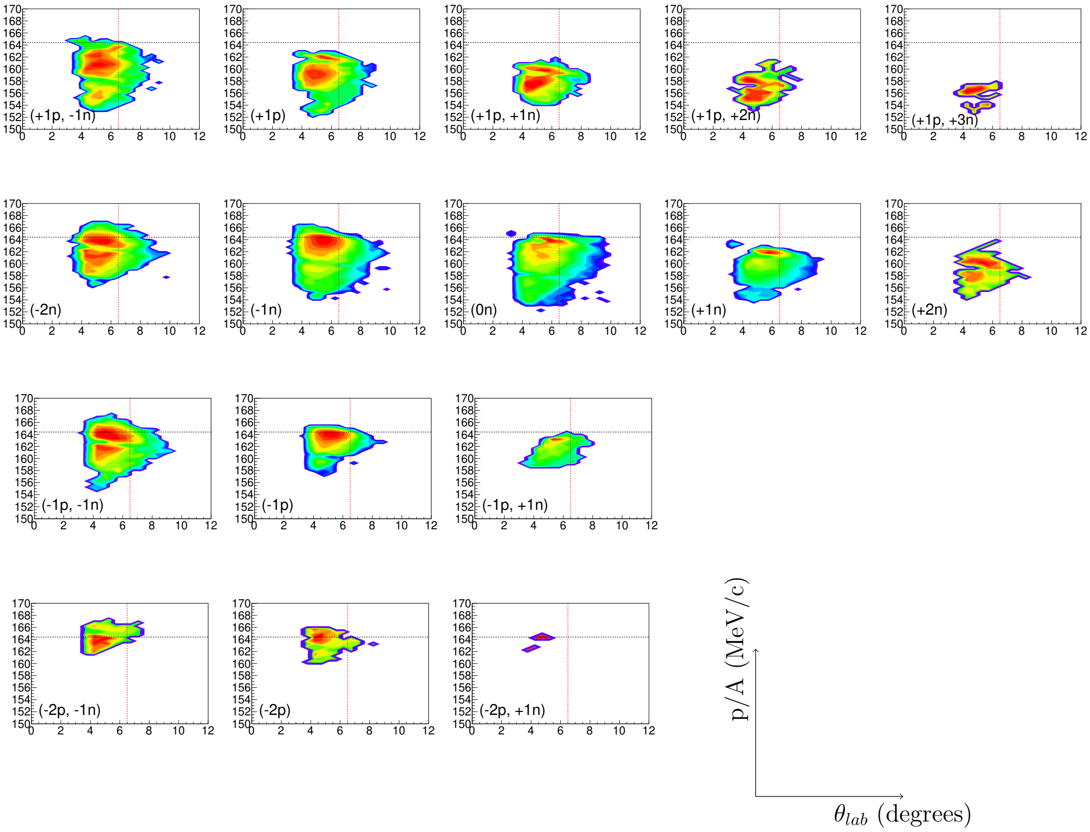

Figure 5.1: Wilczynski plots of ejectiles from representative channels of the reaction ^{70}Zn (15 MeV/nucleon) + ^{64}Ni. The horizontal lines represent the p/A of the projectile and the vertical lines the grazing angle. Channels are marked by the number of neutrons or protons added or removed from the projectile. The inelastic channel, denoted as ”0n” (corresponding to no net nucleon transfer) is also displayed.

acteristic valleys along the θ_{lab} coordinate are observed, or correspondingly dips in the distributions along the p/A coordinate (as can be seen also later). These dips are the result of the software gates imposed during the data analysis to remove the elastically scattered beam. As we may expect, the nucleon pickup products are characterized by overall lower p/A values (velocities) essentially due to momentum conservation, as these projectile-like fragments have picked up nucleons from the ”stationary” target. It is noted here that a velocity shift for nucleon pickup products has also been observed at higher (fragmentation) energies (80–140 MeV/nucleon) [97, 98] and interpreted with a simple momentum conservation model. It is further observed that the distributions peak at and near the grazing angle. This fact reveals the quasielastic and deep-inelastic character of the production mechanism.

At this point, these plots will not be discussed further. Instead, attention will be given to, first, the integration of these distributions with respect to p/A that will give angular distributions (to be discussed later), whose further integration with respect to θ_{lab} will provide the production cross sections of the observed nuclides. Moreover, we will proceed with integration of these two-dimensional distributions over θ_{lab} in an appropriate window that will result in the p/A distributions.

5.2 Production Cross Sections

In Figs. 5.2 and 5.3, the production cross sections for the observed isotopes of the elements with Z = 28–31 from the reaction ^{70}Zn (15 MeV/nucleon) with ^{64}Ni are presented. In both figures, the experimental data are shown by the full black points. The vertical dashed (green) line indicates the beginning of neutron pickup that develops from this line to the right.

As it is evident from these figures (and also from Fig. 5.1), the present experiment successfully achieved the production and complete characterization – in terms of Z, A, p/A and θ_{lab} – of several neutron-rich nuclides corresponding to the pickup of 2–3 neutrons from the target.

The distinct advantage of employing the MAGNEX spectrometer is the high-resolution measurement of the reaction angle and the momentum resulting from the trajectory reconstruction procedure. This detailed angular and momentum information plays a key role in the elucidation of the reaction mechanisms, as already noted in relation to Fig. 5.1 and will be further elaborated in the following sections.

The experimental cross sections are now compared with the DIT and CoMD calculations presented in Figs. 5.2 and 5.3, respectively. We note that the calcu-

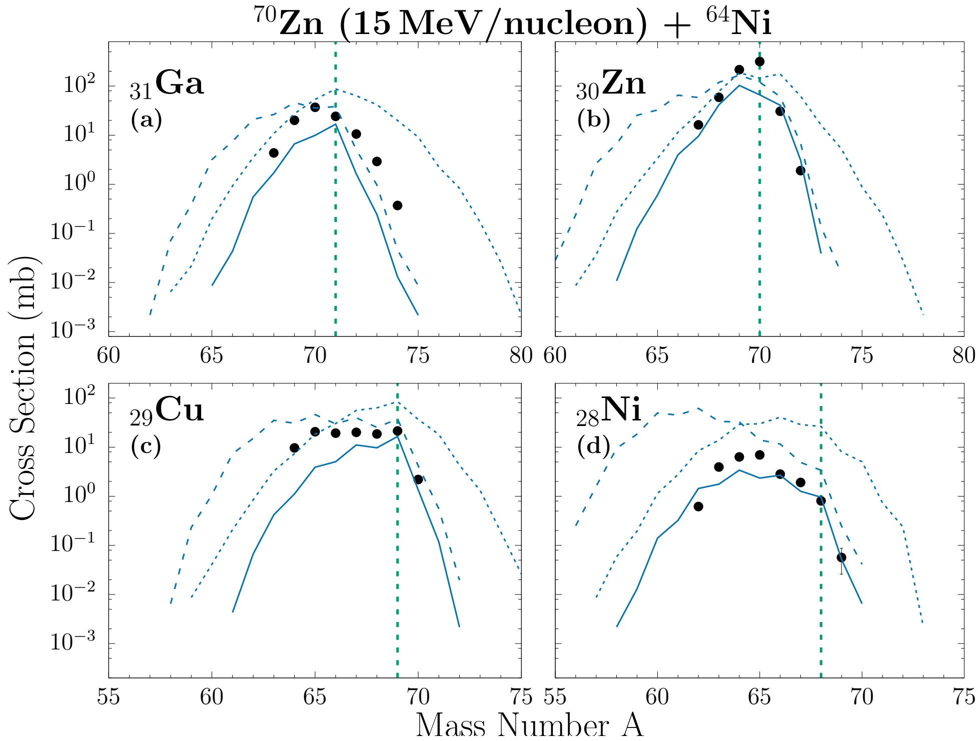

Figure 5.2: Mass distributions (cross sections) of elements with Z = 28–31 from the reaction ^{70}Zn(15 MeV/nucleon) + ^{64}Ni. The experimental data are shown by closed (black) circles. The DIT calculations are shown as follows: primary fragments with dotted (blue) line, final (cold) fragments with dashed (blue) line, and final fragments filtered for acceptance with the solid (blue) line (see text). The vertical dashed (green) line indicates the initiation of neutron pickup.

lations are performed using a Monte Carlo approach leading to calculated distributions (differential cross sections) in terms of Z, A, p/A and θ_{lab}. Moreover, ionic charge states can be assigned to the above distributions by employing the parametrization of charge state distributions of Leon et al. [74] that was also employed in the analysis of the experimental data in Chapter 3. Thus, the calculated distributions can be appropriately projected (and/or integrated) so that they can be compared with the experimental data.

In Fig. 5.2, focus will be initially directed towards the calculated yield distributions of the primary projectile-like fragments (quasiprojectiles) presented by the dotted (blue) lines. Wide and nearly symmetric distributions are observed, extending significantly towards the neutron-rich side. The deexcitation of these excited primary products with the GEMINI code leads to the (cold) nuclides with cross sections depicted by the dashed (blue) lines. The distributions of these fi-

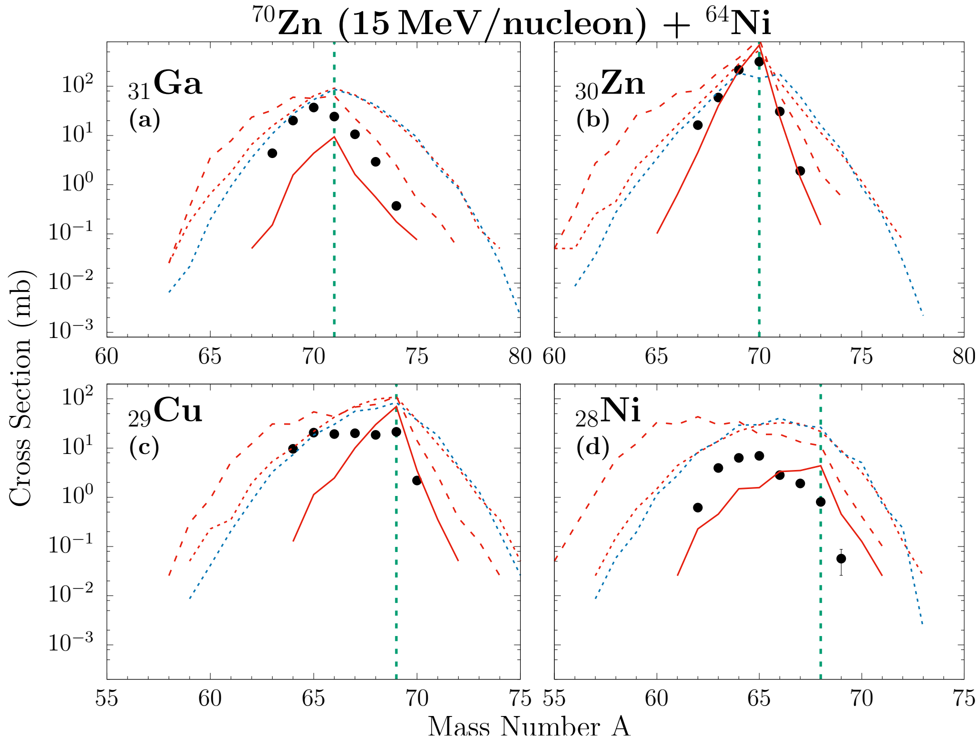

Figure 5.3: Mass distributions (cross sections) of elements with Z = 28–31 from the reaction ^{70}Zn(15 MeV/nucleon) + ^{64}Ni. The experimental data are shown by closed (black) circles. Here, the CoMD calculations are shown as follows: primary fragments with dotted (red) line, final (cold) fragments with dashed (red) line, and final fragments filtered for acceptance with the solid (red) line (see text). For comparison, primary fragments from DIT are repeated with dotted (blue) line. The vertical dashed (green) line indicates the initiation of neutron pickup.

nal nuclides are substantially altered compared to those of the primary nuclides (especially on their neutron-rich side) and are closer to the experimental data. As a general observation, the symmetric shape of the primary yield distributions bears some similarity to that of the yield distributions of products from multinucleon transfer reactions near the Coulomb barrier [25, 26, 32]. However, at our energy, the excitation energies of the primary products are expected to be higher and the evaporation chains longer, thus leading to substantially altered final yield distributions.

Furthermore, in Fig. 5.2, the cross sections are presented with solid (blue) lines after filtering the theoretical distributions for the angular acceptance of MAGNEX $\Delta\theta_{lab}$ = 4° – 15° and the magnetic rigidity interval $B\rho = 1.260 - 1.425\ T\,m$ covered in the experiment. Interestingly, the filtered DIT calculations lead to cross sections that are in overall reasonable agreement with the experimental data. The neutron-rich sides of the distributions are rather well described, with the exception of the Ga (Z=31) isotopes (one-proton pickup). On the neutron-deficient side, both the filtered distributions and the data are considerably lower than the calculated total (i.e. without filtering) cold yield distributions (dashed lines in the figure). This is obviously an effect of the limited Bρ range covered in the present experiment. The calculations show that the minimum Bρ should be 1.000 T m in order to cover the full range of the neutron deficient nuclides.

In Fig. 5.3, the CoMD calculations and their comparison to the data are presented in a manner similar to that of the DIT results. The dotted (red) lines show the CoMD primary yields directly compared to the DIT primary yields (dotted blue lines) that are also repeated in this figure. It is interesting to notice that the two primary fragment distributions are nearly identical, especially on the neutron-rich side. This result suggests that the overall effect of nucleon transfer (exchange) and the mass flow are effectively similar in both models, despite the different physical ingredients of them. As in Fig. 5.2, here again the dashed (red) lines show the cross sections after the GEMINI deexcitation stage, and the full (red) lines show the filtered cross sections.

A remark concerning the CoMD calculations is that while they provide, to some extent, an overall description of the shape of the experimental yield distributions, they tend to overpredict the yields of the neutron-rich sides of the distributions for the isotopes below the projectile. Given the observed similarity in the calculated primary yields between DIT and CoMD, the observed differences in the cross sections are tentatively ascribed to possible differences in the excitation energies of the primary products. Despite the overall better agreement of DIT with the experimental cross section data, the results from both codes will be presented and evaluated in the following discussion. One of the aims of our research group for future works, is to further understand and improve the CoMD results by possible proper choice of the parameters of the model and investigate the excitation energy distributions of the primary products. The results of the latter will be addressed later in section 5.4 of this work.

It is noticeable that the present results do not extend as far out toward neutron-rich nuclides as previous measurements with the 15 MeV/nucleon ^{86}Kr beam on

^{64}Ni and ^{124}Sn with the MARS separator [45, 46], due to severe limitations in the beam current imposed by the experimental setup in which the elastically scattered projectiles were accepted in the focal plane detector. This limitation will be circumvented in the future in view of the ongoing upgrade of MAGNEX [71] toward accepting high rates that will be crucial in order to extend further experimental studies to very neutron-rich nuclides.

5.3 Momentum and Angular Distributions

In this section, we present the momentum per nucleon and the angular distributions for the various reaction channels under investigation. Each channel is examined individually to elucidate the distinct distribution patterns and mechanisms associated with its pathway. For clarity and systematic analysis, the section is organized into subsections, with each subsection dedicated to the momentum and angular distribution characteristics of a specific reaction channel. This structure facilitates a thorough comparison across channels, contributing to a comprehensive understanding of the reaction dynamics.

5.3.1 Inelastic Channel

In Fig. 5.4, the angular and momentum distributions of ^{70}Zn ejectiles are presented. This channel will be referred to as the ”inelastic” channel, including possible complicated processes of nucleon pickup, breakup and evaporation which end up with no net nucleon transfer from the target to the projectile. This point will be revisited later. In Fig. 5.4a, the angular distribution of the inelastic channel is presented. The experimental data are shown by the closed points. The vertical dashed line indicates the grazing angle θ_{gr} = 6.5°. As already mentioned, the elastically scattered projectiles have been removed by software gates, and thus do not contribute. This angular distribution has the characteristic shape of a quasielastic process peaking just inside the grazing angle, as it is the case for the angular distributions of most of the observed channels. The experimental distribution is also compared with the results from the DIT and CoMD calculations shown by open (blue) circles and open (red) squares, respectively. The DIT calculations exhibit a rather flat behavior underestimating the data, while extending to larger angles. The CoMD calculations tend to overestimate the data, while they describe the peak of the data inside the grazing angle.

We now proceed with a discussion of the momentum per nucleon distribution of the inelastic channel, ^{70}Zn, displayed in Fig. 5.4b. The experimental data are shown by the closed points. The vertical dashed line indicates the p/A of the projectile. The horizontal axis gives the p/A in steps of 0.5 MeV/c representing a momentum resolution of $\sim$0.3%. To obtain the p/A distributions, the experimental distributions were integrated in the angular range θ_{lab} = 4°–6°, corresponding to the region around the peak of the distributions. The vertical axis gives the value of $\frac{d^2\sigma}{d\Omega d(p/A)}$ in units of $\frac{mb}{msr(MeV/c)}$.

We have verified that obtaining the p/A distributions of this channel in the full observation window of θ_{lab} = 4°–15°, the shape of the spectrum remains almost unchanged and the differential cross section is only slightly higher. This is valid for all reaction channels involved in this work.

The numbers above some of the peaks give the total excitation energy of the quasiprojectile - quasitarget system obtained using the indicated p/A values and employing binary kinematics. The excitation energy is connected to the reaction Q-value as $E^*_{tot} = Q_{gg} - Q$, where Q$_{gg}$ is the ground-state to ground-state Q-value of the channel, reported on the right side of the p/A figure. The quasielastic peak corresponding to E^*_{tot}=6 MeV represents inelastic excitation of the projectile and/or the target to low-lying states with a combined excitation energy of this value. The bump at E^*_{tot}=42 MeV corresponds to more complicated processes possibly involving the pickup of a neutron from the projectile and the subsequent evaporation of a neutron to yield the ^{70}Zn nucleus. In a similar fashion, as in the detailed analysis of Sohlbach et al. [54], one can assume that the bump at E^*_{tot}=88 MeV corresponds to the pickup of two neutrons from the projectile and a subsequent evaporation. This point will be revisited later by decomposing the DIT calculations into various processes.

In the same figure, along with the experimental data, the DIT calculation is shown with open (blue) circles. The theoretical DIT distributions were filtered taking into account the Bρ range of the experiment and the polar (horizontal) angular window θ_{lab} = 4°– 6° that were chosen for the integration of the experimen-

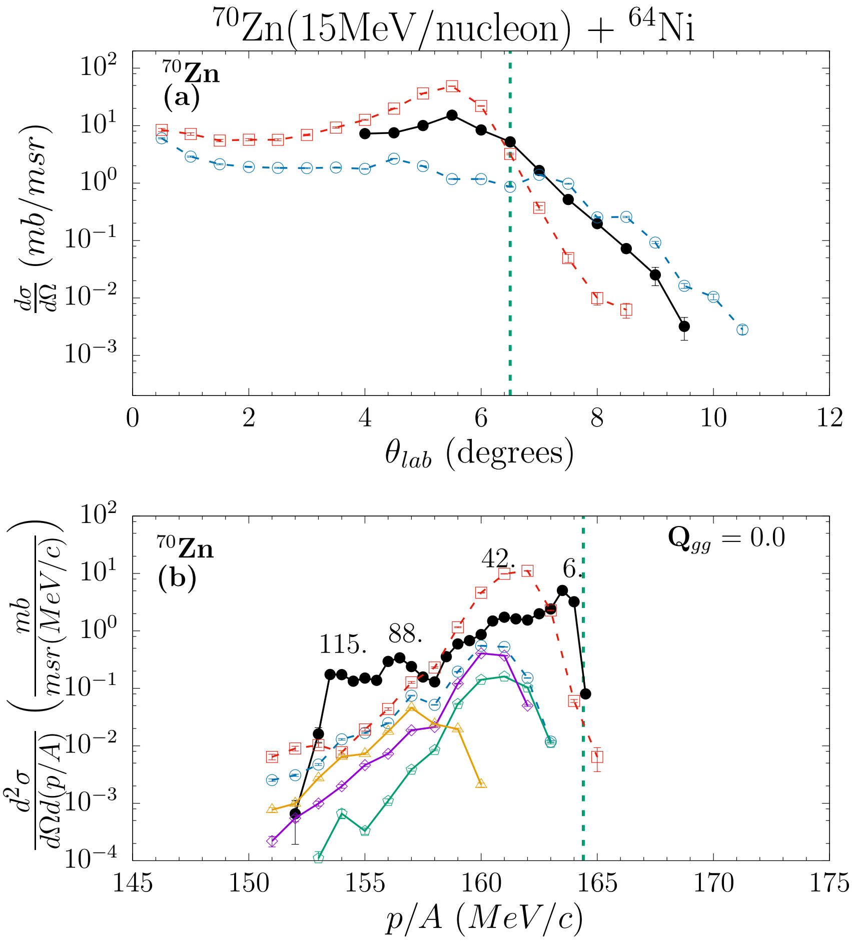

Figure 5.4: (a): Angular distribution of ejectiles from the inelastic channel of the reaction ^{70}Zn (15 MeV/nucleon) + ^{64}Ni. The experimental data are shown by closed (black) circles. The vertical dashed (green) line indicates the grazing angle. The calculations shown are: DIT by open (blue) circles, and CoMD by open (red) squares.
(b) Momentum per nucleon distribution of ejectiles from the inelastic channel. The experimental data are shown by closed (black) circles. The vertical dashed (green) line represents the p/A of the projectile. The numbers above some peaks give the total excitation energy (in MeV) obtained from binary kinematics using the corresponding p/A values.
The DIT calculation is shown with open (blue) circles and the CoMD one by open (red) squares. Three components of the DIT distribution, called QP-0n, QP-1n and QP-2n, are shown under the assumption that the primary fragment (the quasiprojectile, QP) undergoes pick up of no neutrons [open (green) squares], one neutron [open (purple) diamonds] and, two neutrons [open (yellow) triangles] and subsequent evaporation of them.

tal p/A distributions, as already mentioned. Furthermore, since the experimental azimuthal angle window was $\Delta\phi_{lab}$ = 1.6°, and no filter for the above azimuthal acceptance was applied in the calculations, we downscaled the theoretical distribution by the ϕ_{factor} as presented in Chapter 3 before comparing it to the experimental p/A distribution. [This factor is the ratio of the solid angles subtended in the corresponding two cases of polar angular window θ_{lab} = 4°– 6° and azimuthal angular windows of 360°, and $\Delta\phi_{lab}$ = 1.6°.]. It is important to note that the bin width used in the DIT calculation for the p/A spectra is $\Delta(p/A) = 1.0MeV/c$, while the data has a bin width of $\Delta(p/A) = 0.5MeV/c$. This has been properly taken into account in both the data and the calculations when evaluating the double differential cross section $\frac{d^2\sigma}{d\Omega d(p/A)}$.

We observe that the DIT calculation can describe only the part of the distribution from the first bump at p/A=161 MeV/c (E^*_{tot}=42 MeV) and lower. This result is consistent with the fact that DIT has no inherent mechanism of inelastic excitation, thus it cannot describe the inelastic part of the experimental p/A spectrum. It is noted that the only process treated by the DIT model is the sequential transfer of nucleons from the projectile to the target and vice versa. Thus, the discrepancy between the data and the DIT model yields an insight into the direct mechanisms that contributed to the quasielastic ^{70}Zn events.

To elaborate further on the DIT calculation, we performed a decomposition of the p/A distributions of the ejectiles calculated by DIT under the assumption that they come from primary quasiprojectiles that have picked up no neutrons (green squares), one neutron (purple diamonds) and two neutrons (yellow triangles), respectively, and lost an equal number of neutrons in subsequent evaporation. These calculations, presented in Fig. 5.4b, will be referred to as QP-λn, where λ=0,1,2, denoting that the observed ejectile comes from a primary fragment (quasiprojectile, QP) which (after appropriate pickup) has evaporated no neutrons, one neutron, and two neutrons, respectively. The first two of these distributions peak near the experimental bump of E^*_{tot}=42 MeV, with the QP–0n channel contributing 29% and the QP–1n channel contributing 52% of the total DIT distribution. The QP–2n channel (with 13% contribution) peaks at lower p/A values in correspondence with the observed bump at E^*_{tot}=88 MeV, albeit the higher yield of the latter. The dip in the data at p/A=158 MeV/c due to the exclusion of elastically scattered projectiles can also be described by the DIT calculation, provided that a software gate was imposed to exclude elastically scattered projectiles with q=29+ in the calculation.

Between the left side of the inelastic peak of E^*_{tot}=6 MeV and the the right side of the peak of the DIT distribution corresponding to E^*_{tot}=42 MeV, there is an area

Calculation Component	Contribution (%)
QP–0n	29%
QP–1n	52%
QP–2n	13%

Table 5.1: Relative Percentage Contribution of Individual QP-λn Calculations to the Total DIT Calculation for the Inelastic Channel.

of the spectrum that is not accounted for by either of the above two contributions. We tentatively assign this part of the distribution to higher-energy inelastic excitation of the target nucleus to the giant resonance regime possibly involving double (or higher order) resonances (see, e.g. [90] and references therein). A similar contribution may be assumed for the part of the experimental spectrum corresponding to the bump of E^*_{tot}=88 MeV and to lower p/A values including the edge of E^*_{tot}=115 MeV which is near the lower limit of the magnetic rigidity of the experiment.

Furthermore, in Fig. 5.4b, the CoMD calculation (open squares) is also shown. The CoMD calculation is higher and broader than DIT, extending to larger p/A values toward the experimental quasielastic peak. Despite the overall disparity of the CoMD calculation with respect to the data and the DIT calculation, owing to its fully microscopic N-body character, the model has the inherent ability to describe inelastic excitation (in a gross manner – CoMD predicts no discrete states), as well as giant resonances [85] and the collective response of the projectile and the target induced by their mutual interaction. This dynamical behavior of CoMD requires further investigation [91] and is beyond the scope of this work. Along these lines, from an experimental point of view, we wish to mention that investigation of a collective dipole mode, the so called, dynamical dipole mode has been recently performed (e.g. [92, 93] and references therein) via measurements of preequilibrium γ ray emission of the projectile and target after their interaction. In close relation to these studies, we expect that the coupling of the MAGNEX spectrometer with the proposed G-NUMEN array [94, 63, 95] will enable further studies of pre-equilibrium aspects in combination with fully identified ejectiles and elucidation of the relevant deexcitation mechanisms.

5.3.2 Nucleon Removal and Nucleon Pickup Channels

5.3.2.1 Nucleon Removal Channels

The following discussion will proceed with the p/A distributions of some of the most important transfer channels observed, and later on with the corresponding angular distributions. In Fig. 5.5, the p/A distributions of several nucleon removal products are shown. Specifically, the products obtained from the removal of one neutron (^{69}Zn), one proton (^{69}Cu), two neutrons (^{68}Zn) and two protons (^{68}Ni) are presented. As discussed before, the observed dips in the p/A spectra are due to software gates in the data analysis to exclude elastically scattered beam particles.

Concerning the one-neutron removal (-1n) and the one-proton removal (-1p) channels, the experimental p/A distributions have rather similar shapes (apart from the abrupt ending of the second in its left side, due to experimental $B\rho$ restrictions). However, a large difference in the cross sections of the -1n and -1p channels can be observed, the former being one order of magnitude higher than the latter. In these distributions, a distinct quasielastic peak is evident just below the projectile velocity corresponding to low E^*_{tot} and a lower bump corresponding to higher E^*_{tot}, in analogy to the situation regarding the inelastic channel (Fig. 5.4b).

Focusing now to the -1n channel, the first peak at p/A=164 MeV/c and E^*_{tot}=11 MeV can be assigned to a direct process of one neutron stripping from the ^{70}Zn projectile. Furthermore, the part of the distribution below p/A=162 MeV/c may be assigned to a multistep process involving the pickup of one neutron, leading to an excited primary ejectile of ^{71}Zn, and the subsequent evaporation of two neutrons. This analysis is corroborated by the DIT calculation presented in the same manner as in Fig. 5.4b for the inelastic channel. The DIT calculation is lower than the data, but the shape of the quasielastic peak is reasonably well described by the QP–0n component of the calculation. The QP–1n and QP–2n components reasonably well describe the lower part of the distribution and the bump at E^*_{tot}=69 MeV, but they are again lower than the data. The contributions of the above three components relative to the total DIT distribution are 63%, 17% and 11%, respectively (Table 5.2).

Calculation Component	Contribution (%)
QP–0n	63%
QP–1n	17%
QP–2n	11%

Table 5.2: Relative Percentage Contribution of Individual QP-λn Calculations to the Total DIT Calculation for the One-Neutron Removal Channel (–1n).

Analogous remarks pertain to the -1p channel. The quasielastic peak represents a direct proton stripping, and the part at lower velocities comes from a more complex process involving, apart from proton-removal, neutron pickup and subsequent evaporation, corroborated by the DIT analysis, as above. It is interesting to note that the DIT calculation adequately describes the experimental p/A distributions of -1n and -1p channels, most notably the quasielastic part. This points to the overall fair description of the one nucleon stripping, that is the simplest process that can be described by the DIT model. However, the discrepancy in the magnitude of the QE part of the -1n channel may be ascribed to details of the direct processes that require proper analysis with direct reaction codes. Moreover, the discrepancy regarding the lower part of the -1n spectrum may reflect collective excitations of the target, as in the case of the inelastic channel. In regards to the CoMD model, the calculation results in peaks at velocities lower than those of the experimental quasielastic peaks, and appears to overestimate the distributions, especially the one-proton removal channel.

We now focus our attention on the two-neutron and two-proton removal channels, Figs. 5.5c, 5.5d. As in the case of one nucleon removal channels, the spectra are characterized by a quasielastic peak and a lower velocity tail. The two spectra are rather similar, apart from the abrupt left side of the -2p spectrum, the first one being about two orders of magnitude higher. For the -2n channel, the DIT calculation underestimates both the quasielastic peak and the lower part of the p/A distribution. The QP-λn decomposition appears to yield approximately equal contributions($\sim$23%) of the three components. Concerning the -2p channel, the DIT calculation gives a somewhat better description of the experimental spectrum, but it also underestimates the QE side of the spectrum. The three QP-λn DIT components have contributions of 53%, 23% and 12%, following the same trend as obtained for the -1n and -1p channels (Table 5.3).

Calculation Component	Contribution (%)
QP–0n	53%
QP–1n	23%
QP–2n	12%

Table 5.3: Relative Percentage Contribution of Individual QP-λn Calculations to the Total DIT Calculation for the Two-Proton Removal Channel (–2p).

As in the case of reactions at lower energies (e.g. [35] and references therein), we may assume that a process of direct transfer of a nucleon pair (neutron pair or proton pair) contributes to the quasielastic part of these channels. The CoMD calculation appears to describe the -2n spectrum, apart from its QE part. To the contrary, it describes the QE part of the -2p spectrum, but it overestimates the lower part, as in the case of the -1p spectrum. A common observation regarding the left part of the -1n and -2n spectra is that the DIT calculation is substantially lower than the data. As already pointed out, this discrepancy may reflect contributions of collective excitations of the target residual that may be partially accounted for in the CoMD calculation.

After discussing the momentum distributions, we shift our attention to angular distributions of the nucleon removal (stripping) channels presented in Fig. 5.6. The horizontal axis of the distributions is the reaction angle in the lab frame and the vertical axis is the differential cross section $\frac{d\sigma}{d\Omega}$ [$\frac{mb}{msr}$]. The data are given by the closed points, while the open points are the calculations. The vertical dashed (green) line represents the ejectile grazing angle θ_{gr} = 6.5°. As in the case for the inelastic channel (Fig. 5.4a), the angular distributions exhibit a bell-shaped pattern peaking inside the grazing angle. The DIT and CoMD calculations appear to describe the general behavior of the angular distributions. However, the DIT calculations are broader than the data, whereas the CoMD calculations are somewhat narrower and, specifically for the -1p and -2p channels, are higher than the data (as seen also for the corresponding p/A distributions).

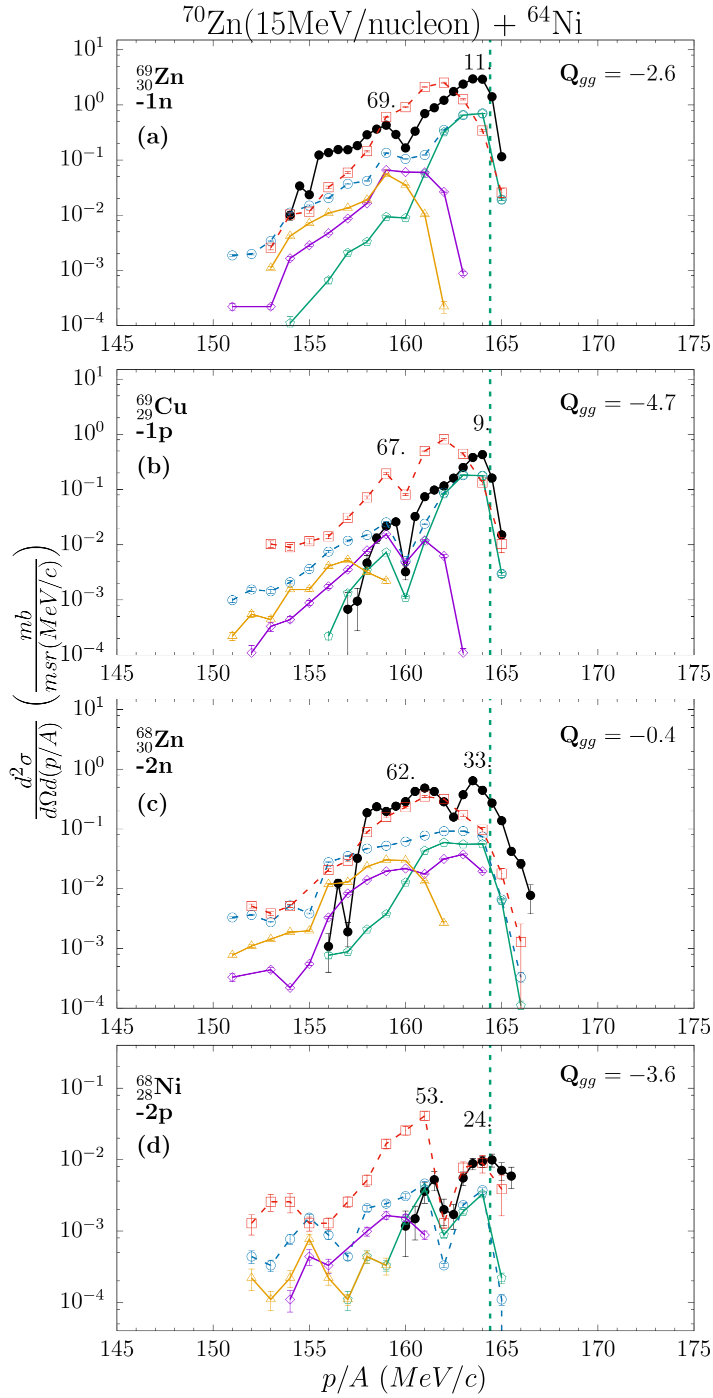

Figure 5.5: Momentum per nucleon distributions of ejectiles from stripping channels of the reaction ^{70}Zn (15 MeV/nucleon) + ^{64}Ni. The experimental data are shown by closed (black) circles. The vertical dashed (green) line is the p/A of the projectile. The DIT calculation is shown by open (blue) circles, and the CoMD one by open (red) squares. The three components of the DIT distribution, namely QP-0n, QP-1n and QP-2n, are also shown with open (green) squares, open (purple) diamonds and, open (yellow) triangles, respectively, as in Fig. 5.4b.

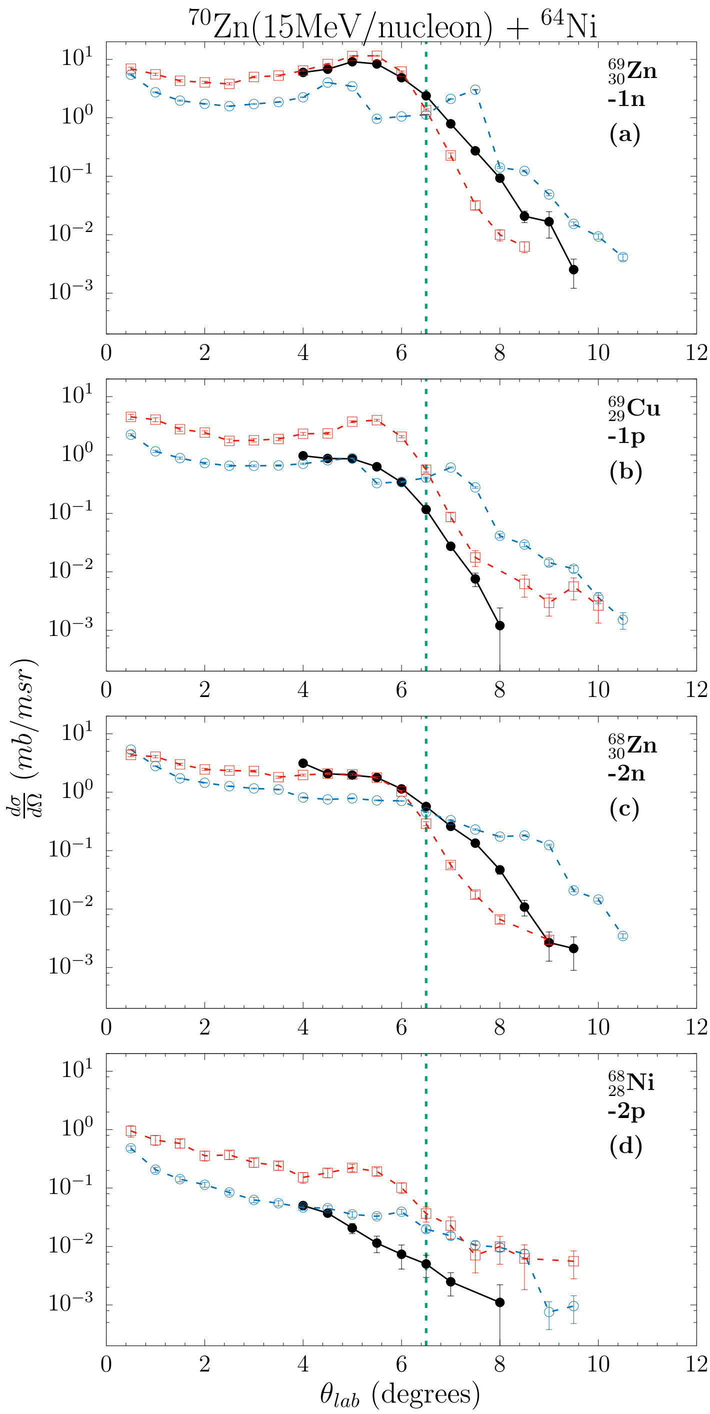

Figure 5.6: Angular distributions of ejectiles from stripping channels of the reaction ^{70}Zn (15 MeV/nucleon) + ^{64}Ni. The experimental data are shown by closed (black) circles. The vertical dashed (green) line shows the grazing angle. The calculations shown are: DIT by open (blue) circles, and CoMD by open (red) squares.

5.3.2.2 Nucleon Pickup Channels

In Fig. 5.7a-c, the p/A distributions of ejectiles with pickup of one proton, one neutron and two neutrons from the target are presented, whereas in Fig. 5.7d the p/A distribution for the single charge exchange channel is shown. As in the case of nucleon removal channels, the spectra of the pickup products are characterized by a quasielastic peak, now located at velocities just below the beam –because of the nucleon pickup– and an extended part at lower velocities. The total excitation energies of the quasielastic peaks, as indicated in the figures, are low. The full calculations with DIT [open (blue) circles with dashed lines] appear to describe part of the quasielastic peak and the shape of the tails of these pickup channels.

Specifically, for the +1p channel, the QP-0n component of the DIT distribution appears to describe only part of the quasielastic peak. To the contrary, the QP-1n is not able to describe the broad experimental peak of E^{*}_{tot}=48 MeV, indicating the inability of DIT to describe the proton pickup and/or the possible contribution of collective excitation of the target remnant in a way similar to the -1n, -2n and the inelastic channels, as discussed before.

Concerning the +2n channel, the QP-0n calculation describes most of the quasielastic part of the spectrum, apart from its right side. The QP-1n component describes the lower part of the p/A spectrum. Again, this observation may suggest the possibility of a direct neutron-pair pickup in the experimental data.

In Fig. 5.7d, we present the p/A distribution of the isotope ^{70}Cu (-1p,+1n) involving single charge exchange. A sharp quasielastic peak appears just below the velocity of the projectile corresponding to very low excitation energy. It is noteworthy that the DIT calculation (the QP-0n component) is able to describe most of the experimental distribution, apart from the quasielastic peak. We may consider this as an indicator of a direct charge exchange process involving meson exchange (see, e.g., [99] and references therein) in addition to the nucleon exchange, the latter process being rather adequately described by DIT.

Regarding the CoMD calculation for all the channels of Fig. 5.7 [open (red) squares with dashed lines], the general behavior is that the calculated p/A distributions exhibit broad peaks at lower velocities than the data, tend to be higher than the data in some of the channels and appear to miss the QE part of the spectra.

While in 5.8, the angular distributions of the nucleon pickup products are shown. The general behavior of the angular distributions exhibit a similar pattern to the ones shown in 5.6 with a bell shaped pattern peaking inside the grazing angle. The DIT and CoMD calculations appear to describe the overall behavior of the experimental data.

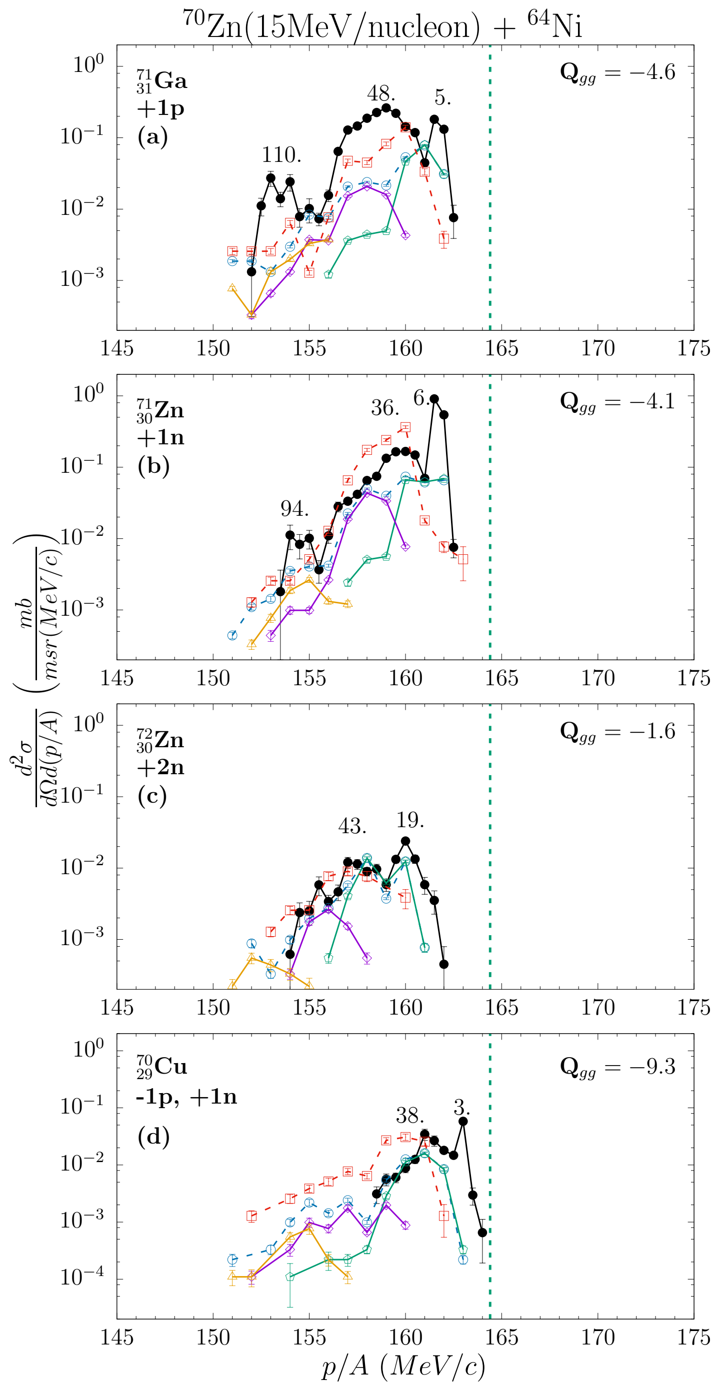

Figure 5.7: Momentum per nucleon distributions of ejectiles from nucleon pickup channels of the reaction ^{70}Zn (15 MeV/nucleon) + ^{64}Ni. The experimental data are shown by closed (black) circles. The vertical dashed (green) line is the p/A of the projectile. The DIT calculation is shown by open (blue) circles, and the CoMD one by open (red) squares. The three components of the DIT distribution, namely QP-0n, QP-1n and QP-2n, are also shown with open (green) squares, open (purple) diamonds and, open (yellow) triangles, respectively, as in Fig. 5.4b.

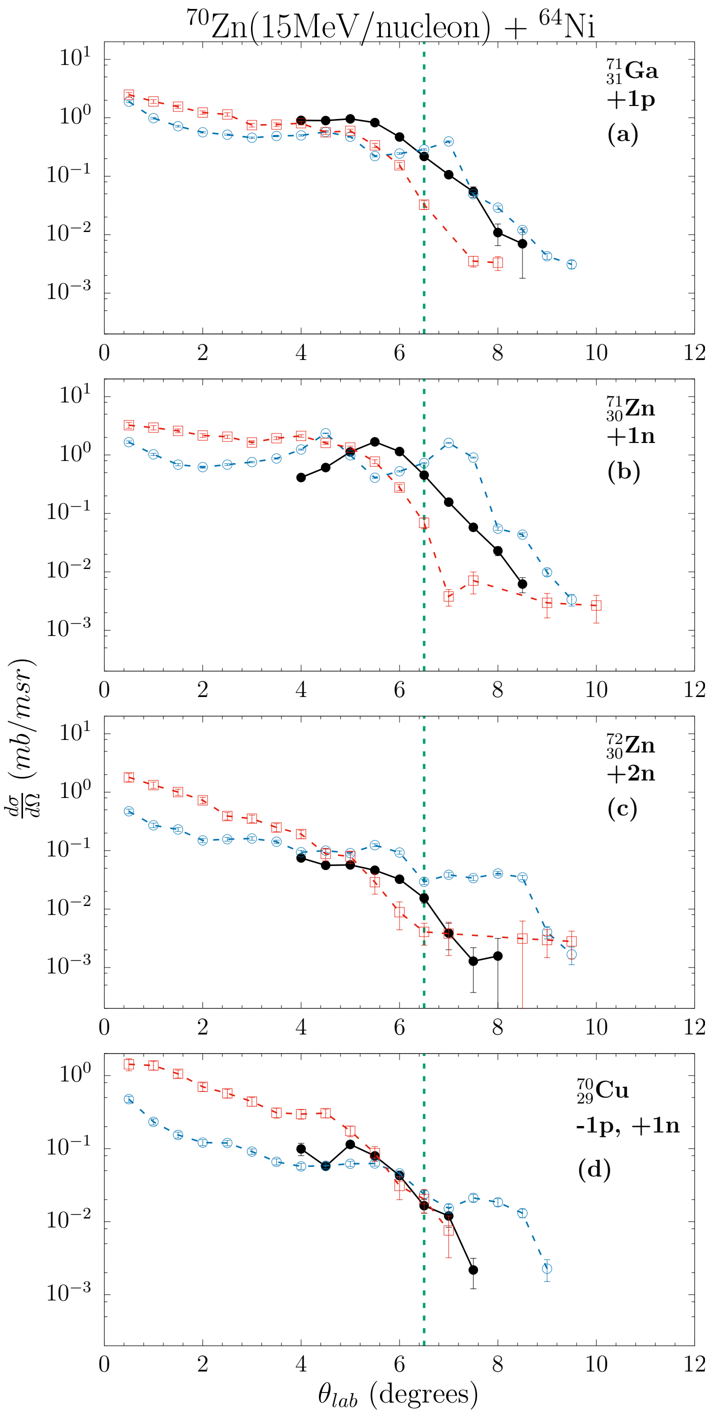

Figure 5.8: Angular distributions of ejectiles from nucleon pickup channels of the reaction ^{70}Zn (15 MeV/nucleon) + ^{64}Ni. The experimental data are shown by closed (black) circles. The vertical dashed (green) line shows the grazing angle. The calculations shown are: DIT by open (blue) circles, and CoMD by open (red) squares.

5.3.3 ”Cluster” Transfer Products

Concluding the presentation of the momentum and angular distributions of various reaction channels, we present in Fig. 5.9, 5.10 the p/A distributions of several nucleon pickup or removal channels that we call ”cluster” pickup or ”cluster” removal channels. The cluster pickup channels correspond to +1p+1n (+^{2}H), +1p+2n (+^{3}H), +1p+3n (+^{4}H) and +2p+2n (+^{4}He), whereas the cluster removal channels correspond to -1p-1n (-^{2}H), -1p-2n (-^{3}H), -1p-3n (-^{4}H) and -2p-2n (-^{4}He).

Regarding the cluster pickup channels, we can observe a progressive displacement of the quasielastic peak to lower velocities with increasing number of nucleons picked up, due to momentum conservation. Both the DIT and the CoMD calculations cannot describe the experimental distributions for these channels, grossly underestimating the data. This may suggest that apart from the sequential pickup of nucleons, the contribution of direct pickup of clusters (d, ^{3}H, ^{4}H, ^{4}He) from the target should be taken into account. Such a process is not described by the DIT or the CoMD models and motivates further theoretical investigation with appropriate models explicitly involving cluster degrees of freedom [100, 101, 102].

Analogous observations pertain for the cluster removal products. In Fig. 5.10 we see that in the case of $-d$ and $-t$ channels, the DIT calculations align well with the trend of the data, whereas the CoMD calculations tend to overestimate the data. In the case of $-^{4}H$ and $-\alpha$, both models underestimate the data of the quasielastic region indicating possibly breakup and/or transfer of these clusters to the target.

The angular distributions of the cluster pickup and cluster removal channels are presented in Fig. 5.11 and Fig. 5.12. Remarks similar to those of the angular distributions of the previously discussed channels pertain to these distributions.

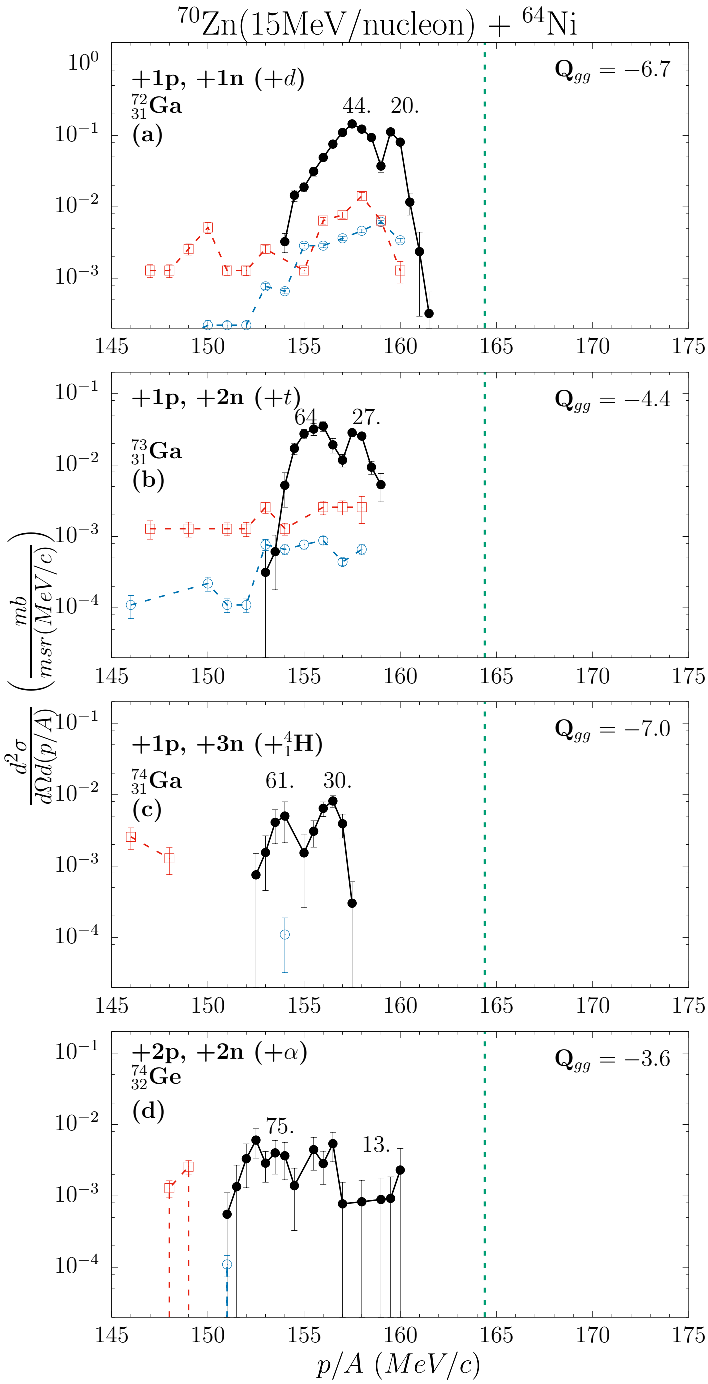

Figure 5.9: Momentum per nucleon distributions of ejectiles from "cluster" pickup channels of the reaction ^{70}Zn (15 MeV/nucleon) + ^{64}Ni. The experimental data are shown by closed (black) circles. The vertical dashed (green) line is the p/A of the projectile. The calculations shown are: DIT by open (blue) circles, and CoMD by open (red) squares.

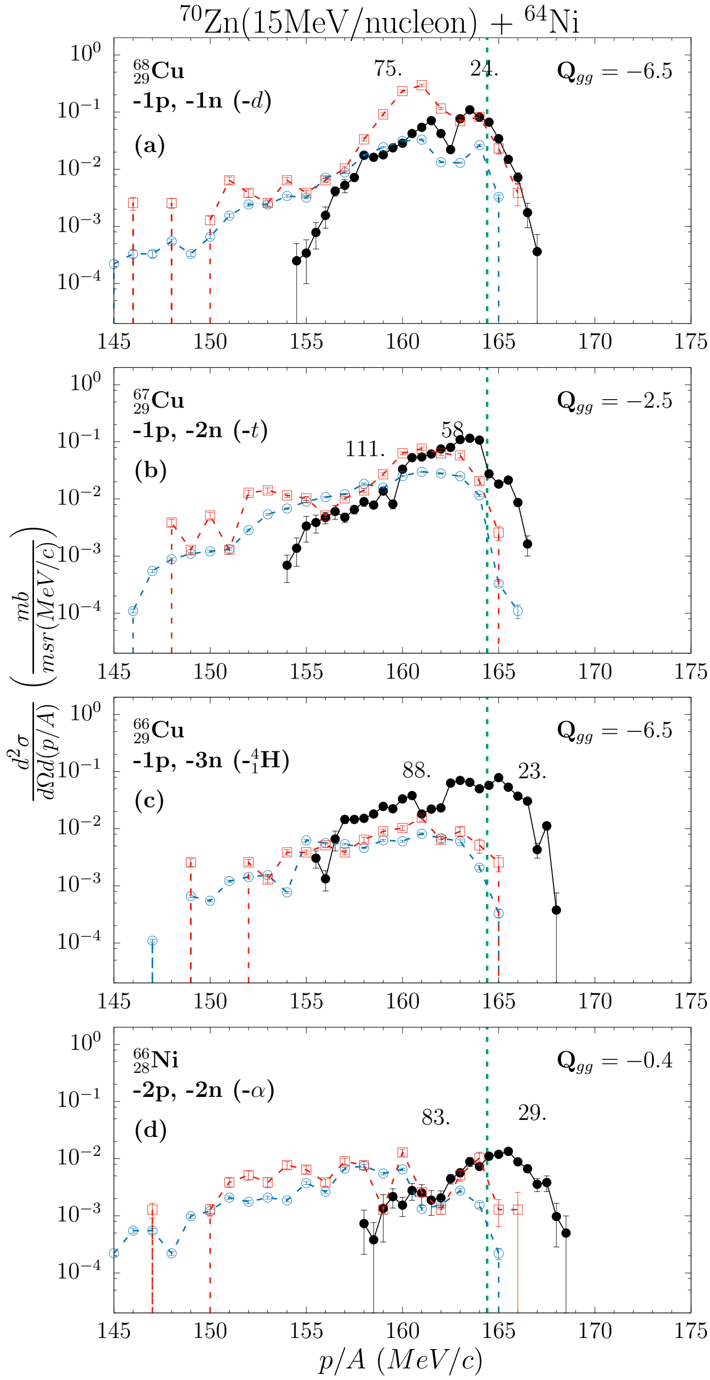

Figure 5.10: Momentum per nucleon distributions of ejectiles from "cluster" removal channels of the reaction ^{70}Zn (15 MeV/nucleon) + ^{64}Ni. The experimental data are shown by closed (black) circles. The vertical dashed (green) line is the p/A of the projectile. The calculations shown are: DIT by open (blue) circles, and CoMD by open (red) squares.

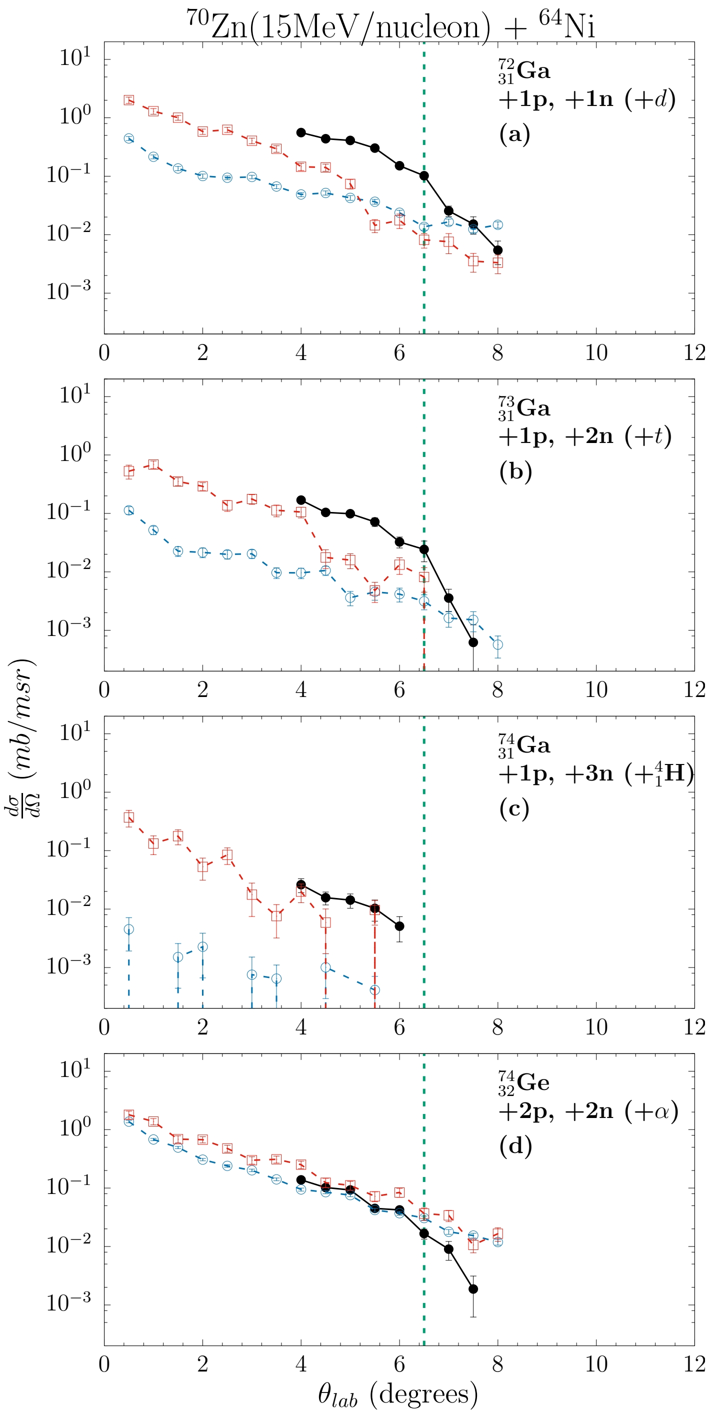

Figure 5.11: Angular distributions of ejectiles from ”cluster” removal channels of the reaction ^{70}Zn (15 MeV/nucleon) + ^{64}Ni. The experimental data are shown by closed (black) circles. The vertical dashed (green) line shows the grazing angle. The calculations shown are: DIT by open (blue) circles, and CoMD by open (red) squares.

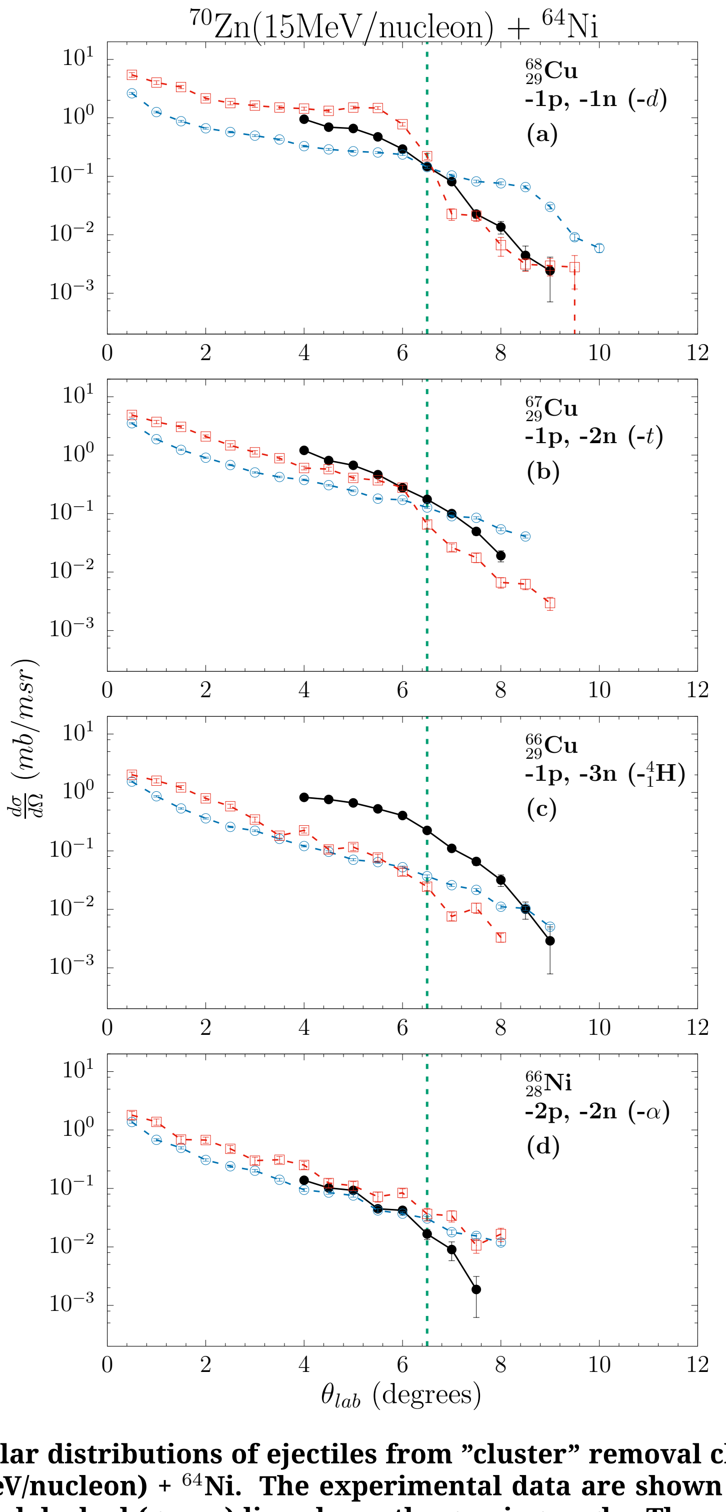

Figure 5.12: Angular distributions of ejectiles from "cluster" removal channels of the reaction ^{70}Zn (15 MeV/nucleon) + ^{64}Ni. The experimental data are shown by closed (black) circles. The vertical dashed (green) line shows the grazing angle. The calculations shown are: DIT by open (blue) circles, and CoMD by open (red) squares.

5.4 Excitation Energy Distributions

In this section, we show results of reconstructed excitation energy distributions from various reaction channels. This comprises a complementary approach to that of the momentum distributions to further elucidate the reaction mechanisms.

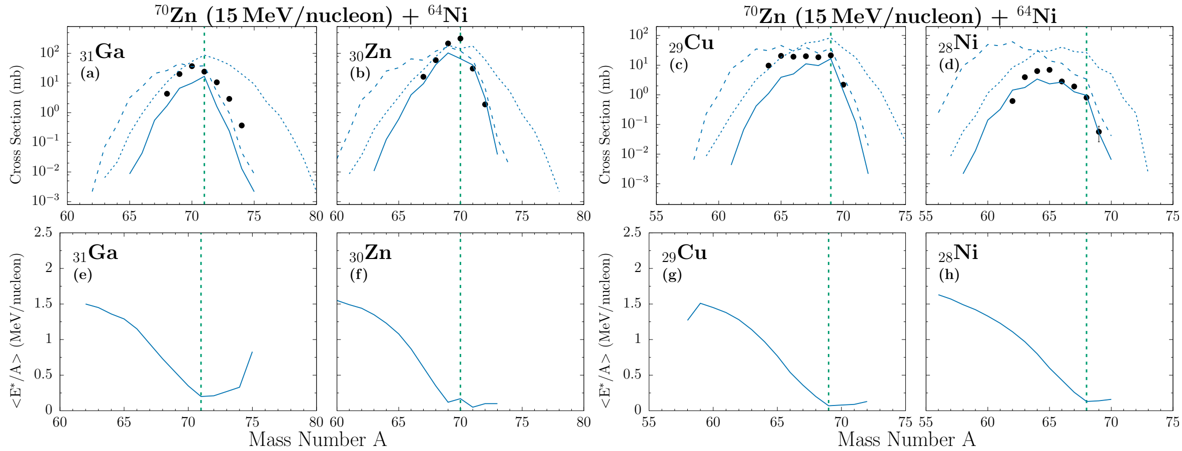

Figure 5.13: Panels (a)-(d): Production cross sections (mass distributions) of elements with Z=31-28 from the reaction ^{70}Zn (15 MeV/nucleon) + ^{64}Ni. Experimental Data: Closed (black) circles. DIT calculations are shown as follows: primary fragments with dotted (blue) line, final (cold) fragments with dashed (blue) line, and final fragments filtered for acceptance with the solid (blue) line. The vertical dashed (green) line indicates the initiation of neutron pickup. Panels (e)-(h): Calculated mean excitation energy per nucleon of primary projectile fragments that lead to observed (cold) fragments of given mass number A.

We begin our discussion by presenting again on panels (a)-(d) of Fig. 5.13, the mass distributions for the observed isotopes of the elements with Z = 28–31 from the reaction ^{70}Zn (15 MeV/nucleon) with ^{64}Ni. We remind that the experimental data are shown by the closed black circles, the vertical dashed (green) line is an indicator for the starting point of neutron pickup and the blue lines represent DIT calculations. Although these production cross section plots were shown in section 5.2, displaying them again in the top panels here serves as a useful guide to discuss the plots of the panels (e)-(h) and their respective behavior.

The panels (e)-(h) of Fig. 5.13 illustrate the calculated mean excitation energy distributions of primary projectile fragments with the use of DIT. This plot represents a correlation of the mean excitation energies per nucleon of the primary (hot) fragments with the mass number of the de-excited final fragments. The primary fragments undergo subsequent de-excitation, resulting in the various nuclides shown in each frame of the figure. It is worth noticing that with an increase in the number of neutrons in the secondary products, the corresponding progenitors from which they originated had progressively lower excitation energies, reaching almost zero values in the very neutron-rich isotopes. This is a justified behavior, as in order to detect such neutron-rich products, they must be quite 'cold', so that they can reach the detector without losing the captured neutrons. We conclude that the production of neutron rich products implies low excitation energies for the progenitors. In other words, surviving very neutron rich products have their origin in "cold" progenitors. And the challenge is how we can obtain experimentally "cold" progenitors.

In panel (a) of Fig. 5.14, excitation energy distributions of ejectiles from the inelastic channel of the reaction ^{70}Zn (15 MeV/nucleon) + ^{64}Ni are presented. A preliminary reconstruction of the total excitation energy of the quasiprojectile (QP)-quasitarget (QT) binary system was attempted, that resulted in the observed fragments based on binary kinematics on an event-by-event basis. The procedure of reconstruction follows the approach developed and reported in Ref.[52]. The reconstruction is performed under two different assumptions. The first assumption takes into account only neutron emission from the progenitor that produces this ejectile (closed black circles with full lines). The second assumption represents the limit of no evaporation (black crosses with dashed lines). That is, the observed ejectile comes from a progenitor with very low excitation energy (below the neutron evaporation threshold); thus the excitation energy is almost fully deposited in the target-like partner. The obtained experimental data are compared with the DIT calculations shown by open (blue) circles. We extended our efforts to further investigate the reaction mechanisms and the role of the primary fragments, by proceeding to a decomposition of the E^* distributions of the ejectiles predicted by DIT. We assumed that the cold (final) fragments originate from primary quasiprojectiles that have picked up no neutrons (green squares), one neutron (purple diamonds), and two neutrons (yellow triangles), respectively, and lost subsequently via evaporation an equal number of neutrons. These calculations are referred to as QP-λn, where λ = 0, 1, 2, meaning that the observed ejectile comes from a primary fragment (quasiprojectile, QP) which (after appropriate pickup) has evaporated no neutrons, one neutron, and

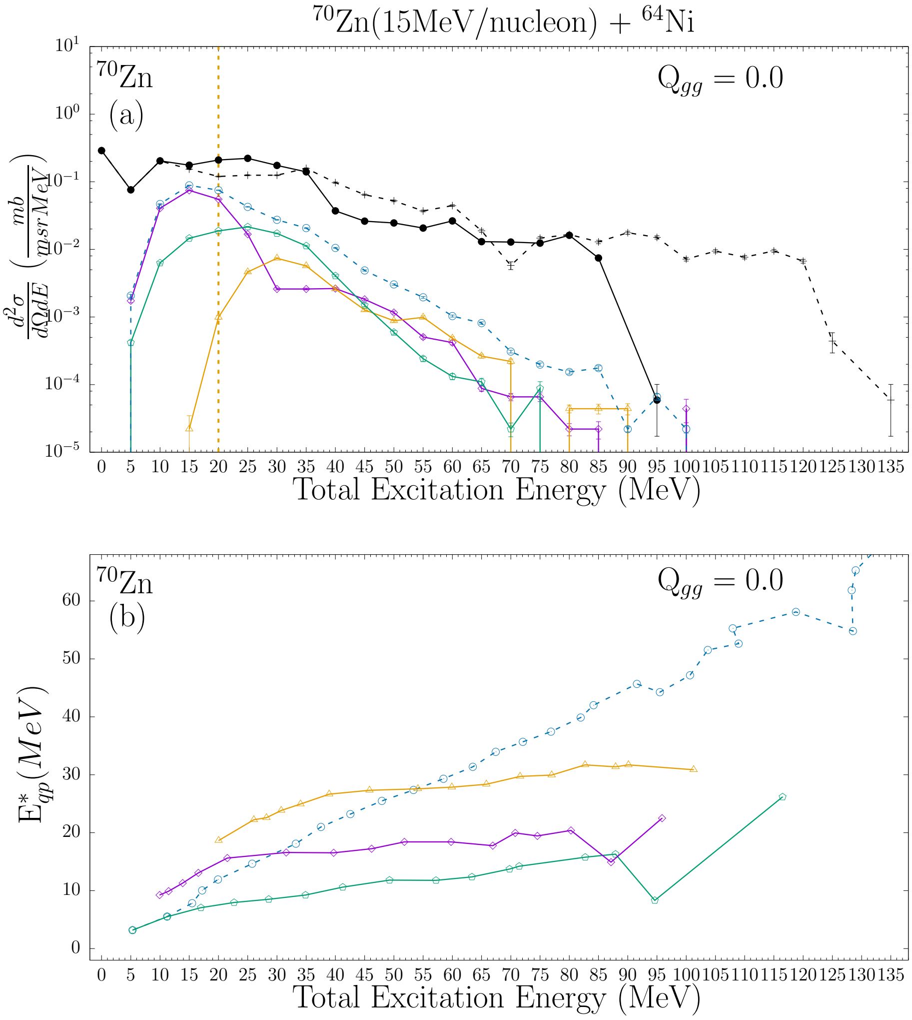

Figure 5.14: Panel (a): Reconstructed excitation energy distributions of ejectiles from the inelastic channel of the reaction ^{70}Zn (15 MeV/nucleon) + ^{64}Ni. Experimental Data: Neutron evaporation-only [closed (black) circles with full lines], no evaporation limit [(black) crosses with dashed lines]. Panel (b): Calculated excitation energy of primary quasiprojectiles leading to ^{70}Zn as a function of the total excitation energy of the primary quasiprojectile - quasitarget system. The DIT calculation is shown with open (blue) circles. Three further components of the DIT decomposition, QP-0n, QP-1n and QP-2n, are shown under the assumption that the primary fragment (the quasiprojectile, QP) undergoes pick up of no neutrons [open (green) squares], one neutron [open (purple) diamonds] and, two neutrons [open (yellow) triangles] and subsequent evaporation of them (see text).

two neutrons, respectively. The (orange) vertical dashed line at 20 MeV indicates an empirical threshold of quasielastic processes, defining the limit of no neutron emission from the QP. The vertical axis gives the double differential cross section with respect to solid angle and excitation energy $\frac{d^2\sigma}{d\Omega dE}$ in units of $[\frac{mb}{msr(MeV)}]$. All the excitation energy distributions discussed in this work (as the p/A distributions of our previous work [103, 104]) are obtained in the polar angular range of θ_{lab} = 4 - 6° (and the azimuthal range $\Delta\phi$ = 1.6°), thus corresponding to $\Delta\Omega$ = 1.0 msr. It has been verified that if the distributions are obtained in the full angular range θ_{lab} = 4 - 15°, the shape of the distributions does not change whereas the cross sections are slightly increased. The general behavior of the reconstructed excitation energy distributions indicates a progressive decrease of the cross section with respect to the increase of the total excitation energy of the primary binary system. The experimental distributions are compared with the components of the DIT calculation, with the following qualitative correspondence: the QP-0n calculation is in good agreement with the behaviour of the data in the quasielastic region (low excitation energy), the QP-1n calculation attempts to describe the middle area of the distribution, while the QP-2n calculation presents a tail toward the dissipative region (high total excitation energy). The following observations are in line: the experimental data obtained under the assumption of no evaporation extend to larger excitation energies compared to the data obtained assuming neutron evaporation only. Moreover, the experimental data are higher than the DIT calculations, possibly implying the existence of inelastic excitation mechanisms that cannot be described by the DIT model. This behaviour is in agreement with the conclusions obtained from our previous study of the p/A distributions in section 5.3.

In panel (b) of Fig. 5.14, the DIT calculated correlation of the mean excitation energy of primary quasiprojectiles leading to ^{70}Zn as a function of the total excitation energy of the QP-QT system is presented. The open (blue) circles are from the full DIT calculation and show that the QP obtains nearly half of the available total excitation energy, as expected from peripheral collisions involving nucleon exchange (see [52] and references therein). The open (green) squares indicate the QP-0n component of the DIT calculation indicating the limit of no neutron emission from the quasiprojectile. Furthermore, the open (purple) diamonds and the open (yellow) triangles present the QP-1n and QP-2n component of the DIT calculations. These three correlations are rather flat indicating the corresponding thresholds for 0n, 1n and 2n emission from the QP to give the ^{70}Zn ejectile.

In a fashion similar to Fig. 5.14(a), the reconstructed excitation energy distributions of ejectiles from one- and two- neutron pickup channels [panels (a)-(b)] and the single charge exchange channel [panel (c)] is shown in Fig. 5.15. Inter-

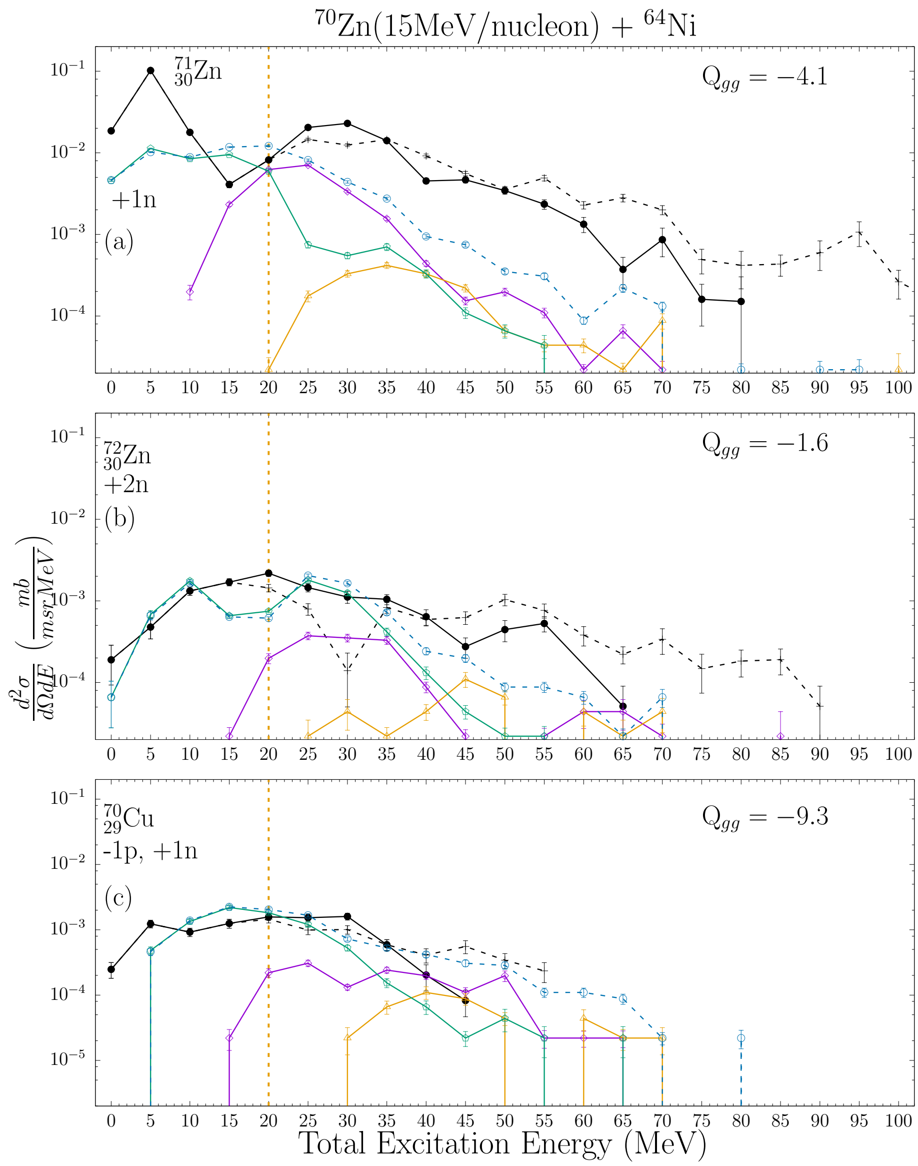

Figure 5.15: Reconstructed excitation energy distributions of ejectiles from nucleon pickup channels of the reaction ^{70}Zn (15 MeV/nucleon) + ^{64}Ni. Experimental Data: Neutron evaporation-only [closed (black) circles with full lines], no evaporation limit [(black) crosses with dashed lines]. The DIT calculation is shown with open (blue) circles. Three further components of the DIT decomposition, QP-0n, QP-1n and QP-2n, are shown under the assumption that the primary fragment (the quasiprojectile, QP) undergoes pick up of no neutrons [open (green) squares], one neutron [open (purple) diamonds] and, two neutrons [open (yellow) triangles] and subsequent evaporation of them.

estingly, in Fig. 5.15(a) a pronounced experimental peak at low excitation energy is observed, that corresponds to direct 1n pickup. This corresponds to the quasielastic peak in the p/A distribution seen in Fig. 5.7(b) and discussed in section 5.3.2.2. We clearly see that it cannot be described by the QP-0n calculation, as DIT describes only a stochastic exchange of nucleons. Also the data above 20 MeV are, as in the case of the inelastic channel, higher than the DIT calculation, hinting again at mechanisms of inelastic excitation followed by transfer that cannot, of course, be described by DIT. The (+2n) and (-1p+1n) channels appear to be described rather well by the DIT calculations except from the quasielastic part of the latter that (as discussed in conjuction with Fig.5.7(d)) may involve a direct charge exchange process mediated by pion exchange.

Finally in Fig. 5.16 we display the excitation energy distributions of nucleon stripping channels. Conclusions similar to Fig. 5.15 may be drawn. Specifically, in the (-1n) and (-2n) channels, the data are above the DIT calculations, possibly pointing at mechanisms beyond nucleon exchange. The QP-0n component of DIT roughly describes the regions below 20 MeV, whereas above 20 MeV the other two components QP-1n, QP-2n progressively take part (but as already mentioned, the calculations are lower than the data).

Looking specifically at the low excitation energy part of the (-2n) and (-2p) spectra (Fig. 5.15(c),(d)) we clearly observe that the data lie well above the DIT calculations suggesting the operation of a direct neutron or proton pair stripping in the data. Further explorations of these channels are in line by our group, motivated by very recent progress in multinucleon transfer studies above the Coulomb barrier [105].

Summarizing, in this chapter we provided a detailed presentation of the distributions for various reaction channels of the ZnNi run set. Additionally, we note that the results of the ZnAl and ZnPb run sets are included in the appendix. The ZnAl run set served as a valuable reconfirmation of the particle identification approach applied in the ZnNi run set. Meanwhile, the ZnPb run set was utilized exclusively for the analysis of Rutherford scattering and was employed in the absolute cross section normalization of the experimental data.

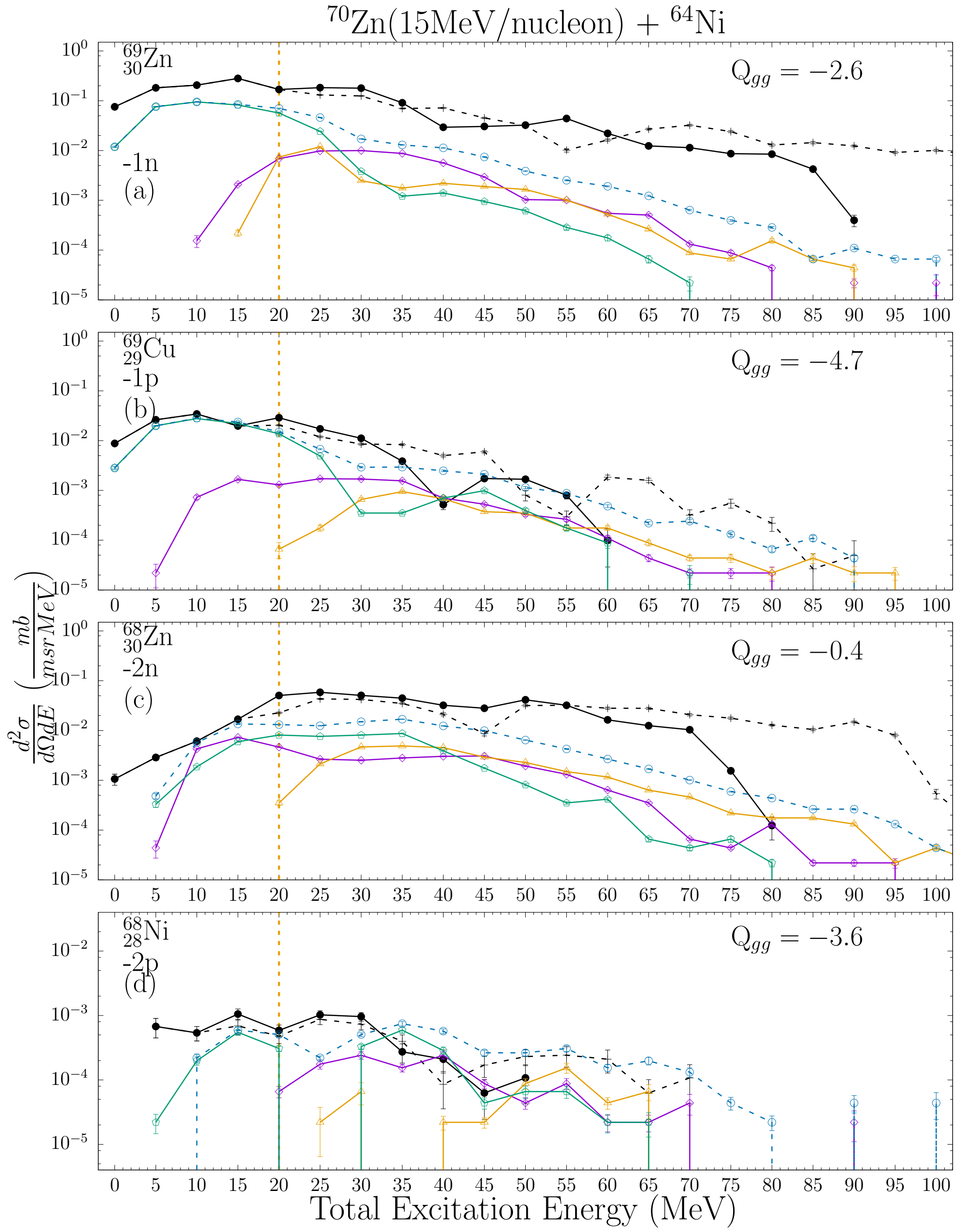

Figure 5.16: Reconstructed excitation energy distributions of ejectiles from stripping channels of the reaction ^{70}Zn (15 MeV/nucleon) + ^{64}Ni. Experimental Data: Neutron evaporation-only [closed (black) circles with full lines], no evaporation limit [(black) crosses with dashed lines]. The DIT calculation is shown with open (blue) circles. Three further components of the DIT decomposition, QP-0n, QP-1n and QP-2n, are shown under the assumption that the primary fragment (the quasiprojectile, QP) undergoes pick up of no neutrons [open (green) squares], one neutron [open (purple) diamonds] and, two neutrons [open (yellow) triangles] and subsequent evaporation of them.

Chapter 6
Conclusions

The results of this work concern the investigation of peripheral reactions of medium mass nuclei in the Fermi energy regime, specifically the study of the reaction ^{70}Zn + ^{64}Ni at 15 MeV/nucleon, utilizing the MAGNEX magnetic spectrometer. The experimental measurements of ejectiles have enabled high-resolution analyses of momentum and reaction angles, providing valuable insights into the underlying reaction mechanisms. The ejectiles were fully characterized in terms of atomic number Z, mass number A, momentum-per-nucleon p/A, and the reaction angle θ_{lab}.

Chapter 2 of this thesis provided a comprehensive overview of the experimental setup and measurements employed to investigate the feasibility of identifying medium-mass ejectiles in heavy-ion reactions at Fermi energies ($\sim$15–20 MeV/nucleon) using the large-acceptance spectrometer MAGNEX. The experiment focused on peripheral collisions of medium-mass nuclei, aiming to validate the identification methodology developed in this work and presented in Chapter 3, respectively. In this first experiment with MAGNEX, we achieved the production of several neutron-rich nuclides close to the projectile. MAGNEX, as one of the few large-acceptance magnetic spectrometers worldwide, utilizes advanced ray reconstruction techniques to overcome optical aberrations, enabling high-resolution measurements. In the present work, the MAGNEX facility offered the distinct advantage of the high-resolution measurement of the momentum and the reaction angle of the medium mass ejectiles in an extended region covering the quasielastic and deep-inelastic processes.

In this work, comparative analyses with the Deep Inelastic Transfer (DIT) and Constrained Molecular Dynamics (CoMD) models, along with the statistical deexcitation code GEMINI, provided insights into the reaction mechanisms. These theoretical models, were presented in Chapter 4.

The DIT model is a phenomenological model of multinucleon transfer, treating the nucleon exchange as a stochastic process where a ‘window’ opens in the nuclear potential, leading to gradual energy dissipation. This results in a broad distribution of fragments in mass, charge, spin, and excitation energy. This model assumes that energy dissipation occurs only through nucleon exchange, without taking into account for nucleon-nucleon collisions.

The CoMD model is a microscopic approach based on Quantum Molecular Dynamics (QMD). It treats nucleons as localized Gaussian wave packets interacting via an effective nucleon-nucleon interaction. A key feature of CoMD is the stochastic restoration of the Pauli principle at each time step, ensuring the correct fermionic behavior of nucleons throughout the reaction dynamics. This allows a more fundamental treatment of nucleon correlations compared to DIT.

Following the dynamical evolution of the system, the GEMINI de-excitation code was used to model the decay of the excited primary fragments through sequential binary decays.

While both DIT and CoMD contributed valuable perspectives on reaction mechanisms, continued development of these models will hopefully ehnance our understanding of the reaction mechanisms in this energy regime.

From a reaction mechanism perspective, the results of this work as presented in Chapter 5, illustrated a range of reaction mechanisms, primarily characterized by two processes: a quasielastic process at low excitation energy, dominated by nucleon stripping, and/or a region of lower velocities (i.e. higher excitation energies) indicating substantial nucleon exchange. The deconvolution of quasielastic and deep-inelastic contributions was successfully attempted, allowing for a more detailed understanding of the reaction dynamics involved. The study revealed also a dominance of direct reaction mechanisms at low excitation energies (below approximately 20 MeV) and identified more complex processes at higher excitation energies. The correlation between the observed ejectiles and the excitation energy of their progenitors, reconstructed through kinematic analysis and DIT calculations, indicated that the survival of very neutron-rich products originates from ”cold” progenitors, with quasiprojectiles carrying, on average, about half of the total excitation energy. This finding paves the way for future research, particularly in understanding the excitation energy sharing between the participants in binary collisions, and the conditions that allow one of them to remain relatively ”cold,” thereby minimizing neutron evaporation.

The present work marks our first step toward detailed studies of peripheral reactions in medium-mass nuclei within the Fermi energy regime with the use of a high-resolution high-acceptance magnetic spectrometer. This regime is characterized by velocities of the reaction partners comparable to the nucleon Fermi velocities and, thus, shorter interaction times, compared to the Coulomb barrier reactions. The reaction mechanism evolves toward favoring faster and/or more dissipated dynamical processes. As examples of fast processes, that were hinted by our experimental data in comparison with our models, we report (a) the high-energy inelastic excitation in the region of giant resonances, possibly involving multiphonon excitations, (b) the direct transfer of nucleon (neutron or proton) pairs, (c) the meson-mediated single charge exchange and, (d) the direct transfer of clusters between the reaction partners. Each of these interesting processes is a nuclear dynamics topic by itself and shows the exciting possibilities for subsequent near-term investigations inspired by the present work along with future experimental and theoretical studies.

Although this study achieved the production of several neutron-rich nuclides close to the projectile, limitations in beam current during the experiment restricted the production of even more neutron-rich nuclides. Future enhancements to the MAGNEX focal plane detector will facilitate high-rate measurements and extend further studies of the group towards this direction. Furthermore, the planned coupling of the upgraded MAGNEX spectrometer with the G-NUMEN array will enable simultaneous studies of γ rays in coincidence with fully identified ejectiles, further exploring the dynamics of the reactions and the spectroscopy of the produced nuclides.

In conclusion, this work lays the groundwork for further studies of peripheral reactions of medium-mass nuclei in the Fermi energy regime. The insights gained will help bridge the understanding of multinucleon transfer reactions near the Coulomb barrier with high-energy fragmentation reactions, shedding light on the evolution of various facets of nuclear dynamics. Moving forward, we envision that ensuing studies in this energy and mass regime will play a pivotal role in linking these different reaction mechanisms while providing essential guidance for the efficient production of exotic neutron-rich nuclei. These efforts will be particularly relevant to explore the r-process path and the neutron drip line, further advancing our understanding of nuclear structure and astrophysical nucleosynthesis.

Appendix A
Analysis of the Ejectile Distributions of the ^{70}Zn (15 MeV/nucleon) + ^{27}Al Reaction

A.1 Introduction

In this appendix, we present the results of the data analysis for the ZnAl run set, corresponding to the reaction of ^{70}Zn with ^{27}Al at 15 MeV/nucleon. Unlike the primary ZnNi run set discussed in the main results chapter, the ZnAl run set consisted of a single experimental run (i.e., run 39) conducted with a magnetic rigidity setting of 1.2880 Tm, similar to runs 22-34, 41–61 of the ZnNi run set. The target used in this run set was aluminum (^{27}Al) with a thickness of 810 $\mu g/cm^2$.

Although limited in scope of the data collected, the ZnAl data provide valuable supplementary insights. In particular, the results offer an interesting perspective and serve as an effective verification indicator for the particle identification (PID) approach introduced and predominantly applied to the ZnNi run set. The detailed distributions of various reaction channels derived from this run are summarized and analyzed in the following sections.

Before proceeding to the analysis of the ejectile distributions from the ^{70}Zn (15 MeV/nucleon) + ^{27}Al reaction, we first present Wilczynski plots of representative reaction channels, following the same line of presentation as in Chapter 5. We remind that in the plots of Fig. A.1, the horizontal lines represent the projectile p/A=164.4 MeV/c and the vertical lines indicate the grazing angle θ_{gr} $\simeq$3.5° of the ejectiles of the reaction. The various channels are marked by the number of neutrons or protons added or removed from the projectile. For orientation, the channel of ^{70}Zn, corresponding to no net nucleon transfer, called the ”inelastic” channel, is displayed in the middle panel.

As observed and discussed in detail in Chapter 5, the general features of the Wilczynski plots for the ^{70}Zn + ^{27}Al reaction channels follow the same behaviour. Specifically, a quasielastic peak is evident near the beam velocity, followed by a more dissipative region at lower velocities. The characteristic valleys along the θ_{lab} coordinate, resulting from software gates applied to remove elastic scattering, are also present. Furthermore, nucleon pickup products exhibit lower p/A values due to momentum conservation. Finally, for several channels (e.g. -1n, -2n, +1p-2n) a third region of lower p/A is present, as we will explain in the following section A.2.2.4, that possibly corresponds to a incomplete fusion mechanism.

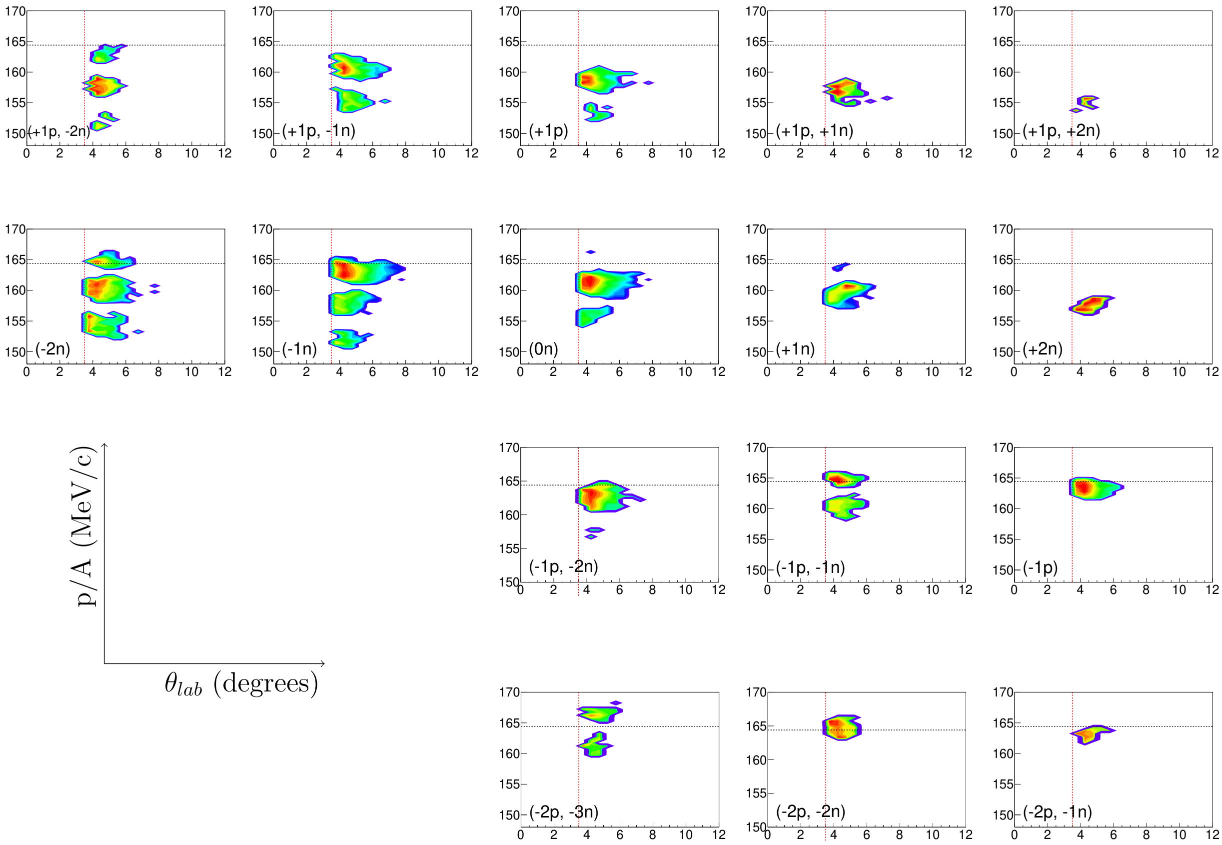

Figure A.1: Wilczynski plots of ejectiles from representative channels of the reaction ^{70}Zn (15 MeV/nucleon) + ^{27}Al. The horizontal lines represent the p/A of the projectile and the vertical lines the grazing angle. Channels are marked by the number of neutrons or protons added or removed from the projectile. The inelastic channel, denoted as "0n" (corresponding to no net nucleon transfer) is also displayed.

A.2 Results

A.2.1 Production Cross Sections

Following the same line of presentation as the run set ZnNi, we present in Fig. A.2 the production cross sections for the observed isotopes of the elements with Z = 28–31 from the reaction ^{70}Zn (15 MeV/nucleon) with ^{27}Al. The experimental data are shown by the full black points. Despite the limited extent of this work, we achieved the identification of several neutron-rich nuclides corresponding to the pickup of 1–2 neutrons from the target, as can be seen in the case of the experimental data for Zn and Ga. The vertical dashed (green) line indicates the starting point of neutron pickup, that is, to the right of this line lie nuclei with a net neutron pickup from the target.

The experimental cross sections are also compared with DIT calculations, in the same fashion as presented in Fig. 5.2 of Chapter 5 of this work. Wide and nearly symmetric distributions can be observed in terms of the calculated yield distributions of the primary projectile-like fragments (quasiprojectiles) presented by the dotted (blue) lines, extending significantly towards the neutron-rich side. The deexcitation of these excited primary products with the GEMINI code leads to the (cold) nuclides with cross sections depicted by the dashed (blue) lines.

These distributions exhibit significant changes compared to those of the primary nuclides, particularly on their neutron-rich side, and show some alignment with the experimental data. Furthermore, in Fig. A.2, the cross sections are presented with solid (blue) lines after filtering the theoretical distributions for the angular acceptance of MAGNEX ($\Delta\theta_{lab}$ = 4° – 15°) and the magnetic rigidity interval 1.260–1.425 T m covered in the experiment, as already mentioned in Chapter 5. Interestingly, the filtered DIT calculations lead to cross sections that generally align well with the experimental data. The neutron-rich sides of the distributions are accurately represented, particularly for Ga (Z=31) and Zn (Z=30), though the agreement is less satisfactory for Cu and Ni. An interesting observation can be made on the neutron-deficient side of the distributions. Specifically, we noticed the presence of ”bumps” in all the distributions, such as in the cases of ^{68}Ga, ^{66}Zn, ^{63}Cu and ^{61}Ni. After careful consideration, we believe that these anomalies sug-

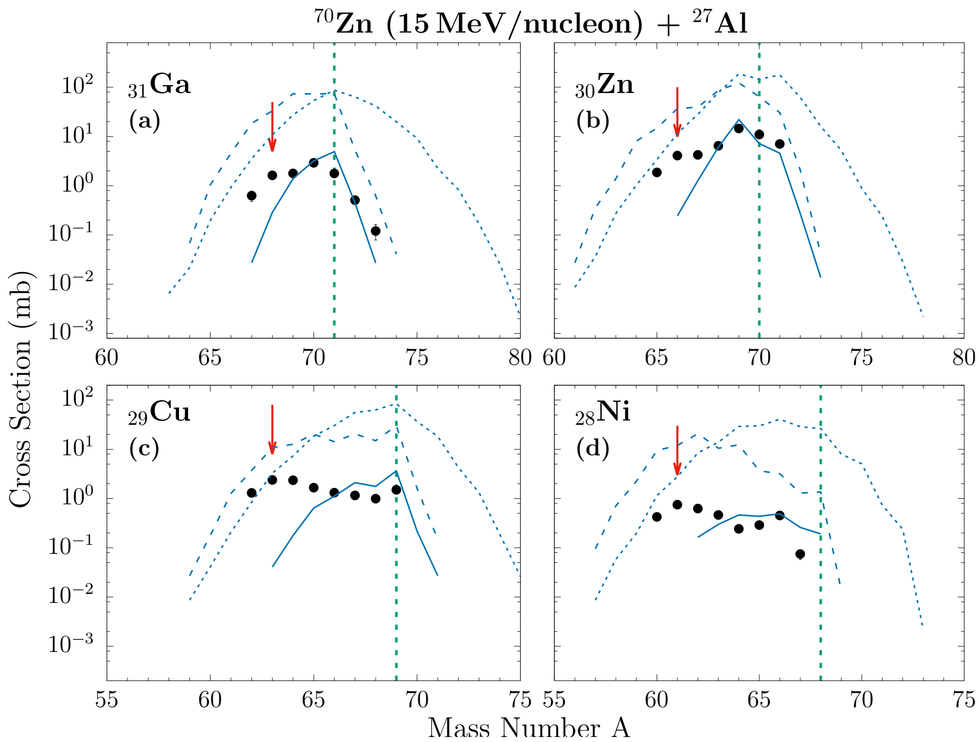

Figure A.2: Mass distributions (cross sections) of elements with Z = 28–31 from the reaction ^{70}Zn(15 MeV/nucleon) + ^{27}Al. The experimental data are shown by closed (black) circles. The DIT calculations are shown as follows: primary fragments with dotted (blue) line, final (cold) fragments with dashed (blue) line, and final fragments filtered for acceptance with the solid (blue) line (see text). The vertical dashed (green) line indicates the initiation of neutron pickup. Finally, the red arrows indicate isotopes in the peaks of the left side of the yield distributions (analyzed in Figs. A.10 and A.11).

gest the involvement of an incomplete fusion reaction mechanism, likely due to the use of a light target like ^{27}Al, which may have contributed to the production of these nuclides. Based on this observation, we will proceed to present the angular and p/A distributions of these ejectiles, along with other reaction channels such as nucleon pickup and removal channels and the inelastic channel.

A.2.2 Angular and Momentum Distributions

A.2.2.1 Inelastic Channel

In Fig. A.3, the angular and momentum distributions of ^{70}Zn ejectiles are presented. This channel is once again referred to as the ”inelastic” channel, including possible complicated processes of nucleon pickup, breakup and evaporation which end up with no net nucleon transfer from the target to the projectile.

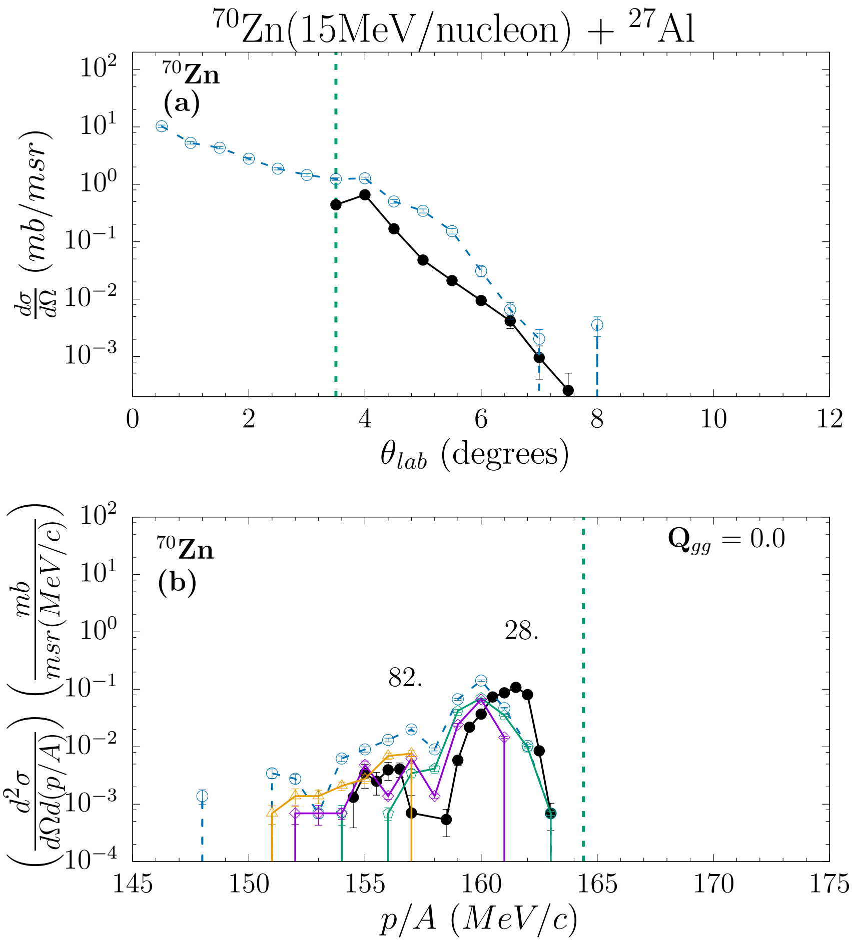

Figure A.3: (a): Angular distribution of ejectiles from the inelastic channel of the reaction ^{70}Zn (15 MeV/nucleon) + ^{27}Al. The experimental data are shown by closed (black) circles. The vertical dashed (green) line indicates the grazing angle. The DIT calculations are shown by open (blue) circles.
(b) Momentum per nucleon distribution of ejectiles from the inelastic channel. The experimental data are shown by closed (black) circles. The vertical dashed (green) line represents the p/A of the projectile. The numbers above some peaks give the total excitation energy (in MeV) obtained from binary kinematics using the corresponding p/A values. The DIT calculation is shown with open (blue) circles. Three components of the DIT distribution, called QP-0n, QP-1n and QP-2n, are shown under the assumption that the primary fragment (the quasiprojectile, QP) undergoes pick up of no neutrons [open (green) squares], one neutron [open (purple) diamonds] and, two neutrons [open (yellow) triangles] and subsequent evaporation of them.

In Fig. A.3a, the angular distribution of the inelastic channel is presented. The experimental data are shown by the closed points. The vertical dashed line indicates the grazing angle θ_{gr} = 3.5° of this system. The elastically scattered projectiles have been removed by software gates, as in the case of run set ZnNi, and thus do not contribute. The experimental distribution is also compared with the results from the DIT calculations shown by open (blue) circles.

In Fig. A.3b, the p/A distribution for the same reaction channel is depicted. The experimental data are represented by closed points, while the vertical dashed line marks the p/A value of the projectile (164.4 MeV/c). The horizontal axis is scaled in increments of 0.5 MeV/c. Additionally, the standard DIT calculation is shown with open (blue) circles. Alongside the standard calculation, the QP-λn analysis of the DIT results is also included, as presented in Chapter 5. The QP-λn decomposition of the DIT calculation will be employed also for the rest of the reaction channels presented for this run set. We remind that, the numbers above some of the peaks give the total excitation energy of the binary quasiprojectile-quasitarget system obtained using the indicated p/A values and employing binary kinematics. The excitation energy is connected to the reaction Q-value as $E^*_{tot} = Q_{gg} - Q$, where Q_{gg} is the ground-state to ground-state Q-value of the channel, reported on the right side of each p/A figure.

A.2.2.2 Nucleon Removal and Nucleon Pickup Channels

In this section, the p/A distributions of some of the most important transfer channels are shown, and later on the corresponding angular distributions are presented.

In Fig. A.4, the p/A distributions of several nucleon removal products are shown. Specifically, the products obtained from the removal of one neutron (^{69}Zn), one proton (^{69}Cu), two neutrons (^{68}Zn) are presented. In general, the QP–0n component of the calculation effectively reproduces the shape of the quasielastic peaks observed in the –1n and –1p channels. The QP–1n and QP–2n components provide a reasonable description of the lower parts of the distributions. Notably, the QP–1n calculation predicts a tail in the dissipative region of the distribution, corresponding to high E^*_{tot}. However, within the extent of this work, it was not possible to collect sufficient data to observe this feature experimentally.

In Fig. A.6, the p/A distributions of ejectiles with pickup of one proton (^{71}Ga) and one neutron (^{71}Zn) from the target are presented. As in the case of nucleon

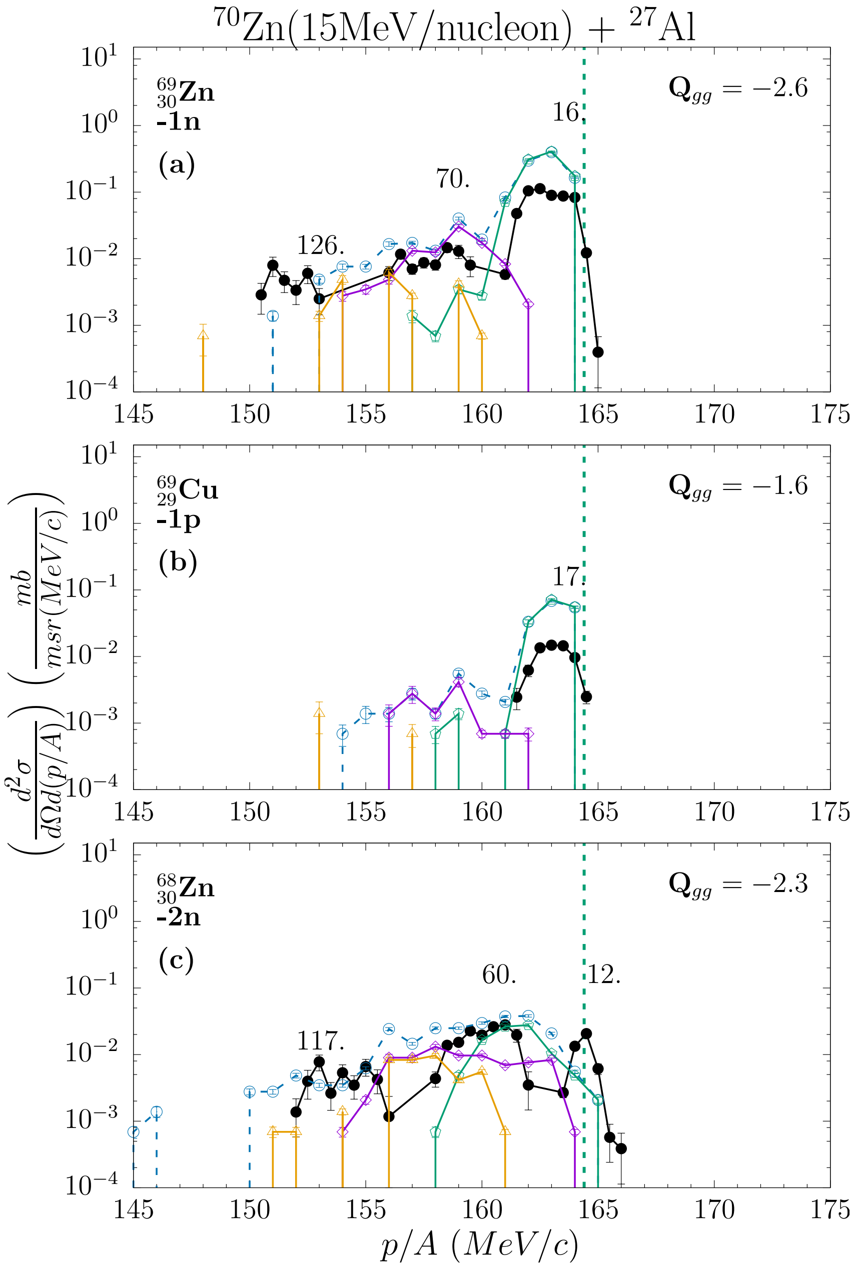

Figure A.4: Momentum per nucleon distributions of ejectiles from stripping channels of the reaction ^{70}Zn (15 MeV/nucleon) + ^{27}Al. The experimental data are shown by closed (black) circles. The vertical dashed (green) line is the p/A of the projectile. The DIT calculation is shown by open (blue) circles. The three components of the DIT distribution, namely QP-0n, QP-1n and QP-2n, are also shown with open (green) squares, open (purple) diamonds and, open (yellow) triangles, respectively, as in Fig. A.3b.

removal channels, the spectra of the pickup products are characterized by a quasielastic peak and an extended part at lower velocities. For completeness of the current presentation, the corresponding angular distributions of these reaction channels are presented in Figs. A.5, A.7, respectively.

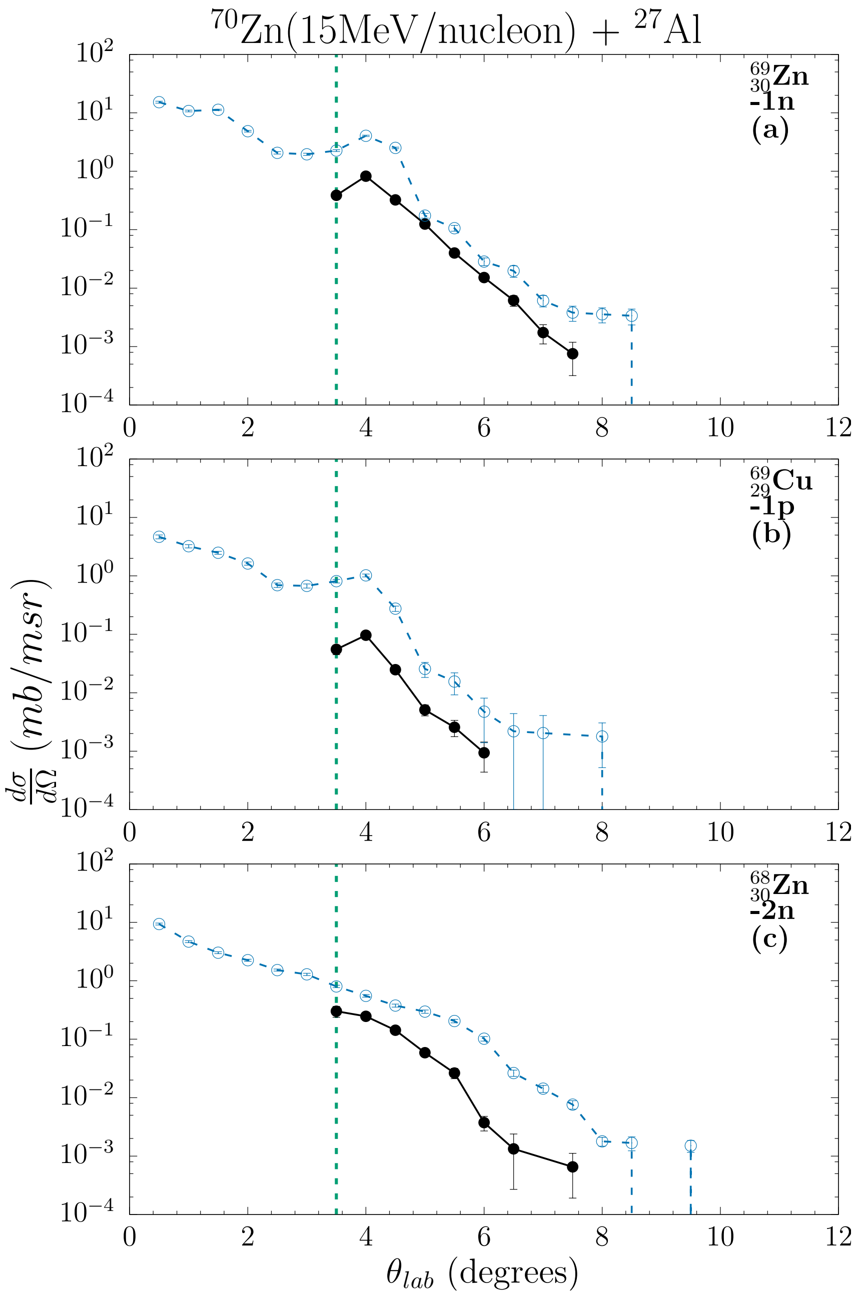

Figure A.5: Angular distributions of ejectiles from stripping channels of the reaction ^{70}Zn (15 MeV/nucleon) + ^{27}Al. The experimental data are shown by closed (black) circles. The vertical dashed (green) line shows the grazing angle. The DIT calculations are shown by open (blue) circles.

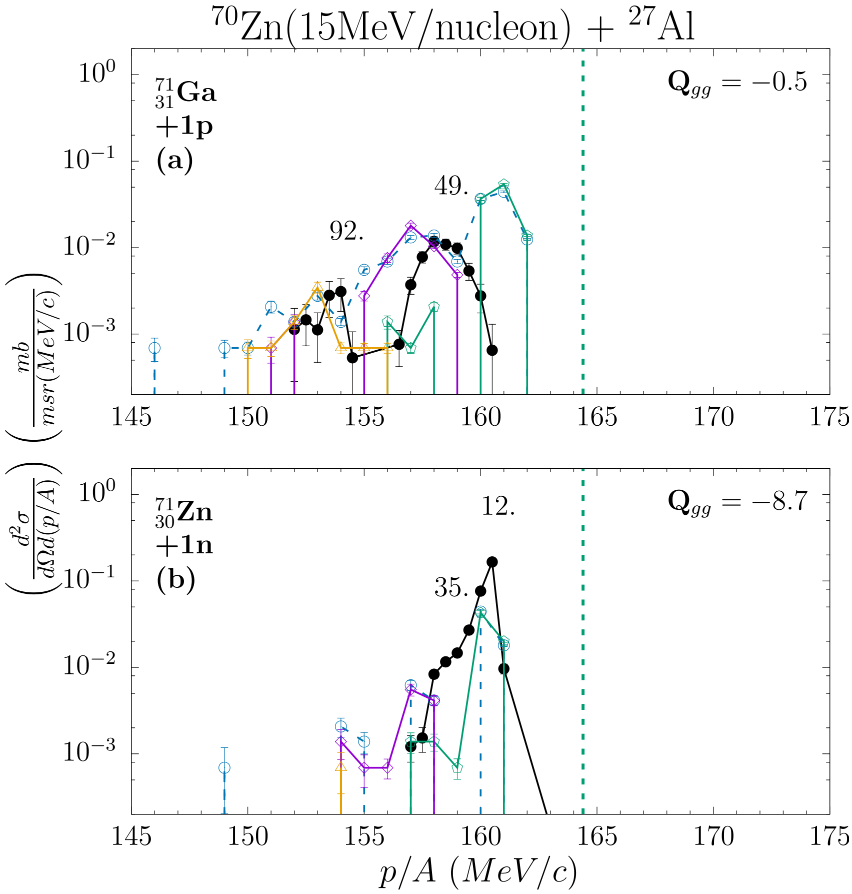

Figure A.6: Momentum per nucleon distributions of ejectiles from nucleon pickup channels of the reaction ^{70}Zn (15 MeV/nucleon) + ^{27}Al. The experimental data are shown by closed (black) circles. The vertical dashed (green) line is the p/A of the projectile. The DIT calculation is shown by open (blue) circles. The three components of the DIT distribution, namely QP-0n, QP-1n and QP-2n, are also shown with open (green) squares, open (purple) diamonds and, open (yellow) triangles, respectively, as in Fig. A.3b.

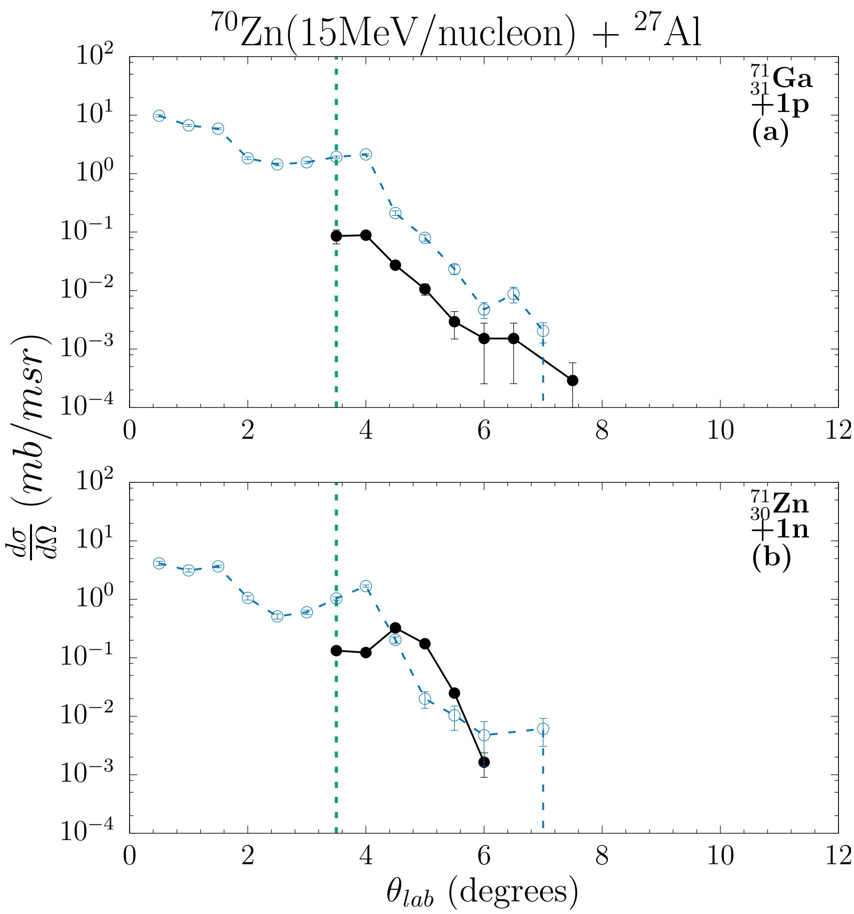

Figure A.7: Angular distributions of ejectiles from nucleon pickup channels of the reaction ^{70}Zn (15 MeV/nucleon) + ^{27}Al. The experimental data are shown by closed (black) circles. The vertical dashed (green) line shows the grazing angle. The DIT calculations are shown by open (blue) circles.

A.2.2.3 Cluster Transfer Channels

In this section, we present in Fig. A.8 and Fig. A.9, the p/A distributions and the respective angular distributions for representative cluster transfer (pickup) reaction channels, specifically the $+1p, +1n$ (^{72}Ga) and $+1p, +2n$ (^{73}Ga) channels.

A notable observation in the p/A distributions is that the experimental data exhibit a significant shift toward lower values of p/A relative to the beam velocity, as indicated by the vertical dashed green line. This shift could be an indication that non-direct, more dissipative processes contribute to the production of these reaction products. Furthermore, along with the standard DIT calculation, only the QP-0n and QP-1n contributions attempt to describe the data.

Regarding the angular distributions, the standard DIT calculations appear to provide a reasonable description of the overall shape of the distribution. However, the calculated cross sections systematically overestimate the experimental data, indicating that additional refinements in the theoretical modeling of these cluster transfer channels may be necessary.

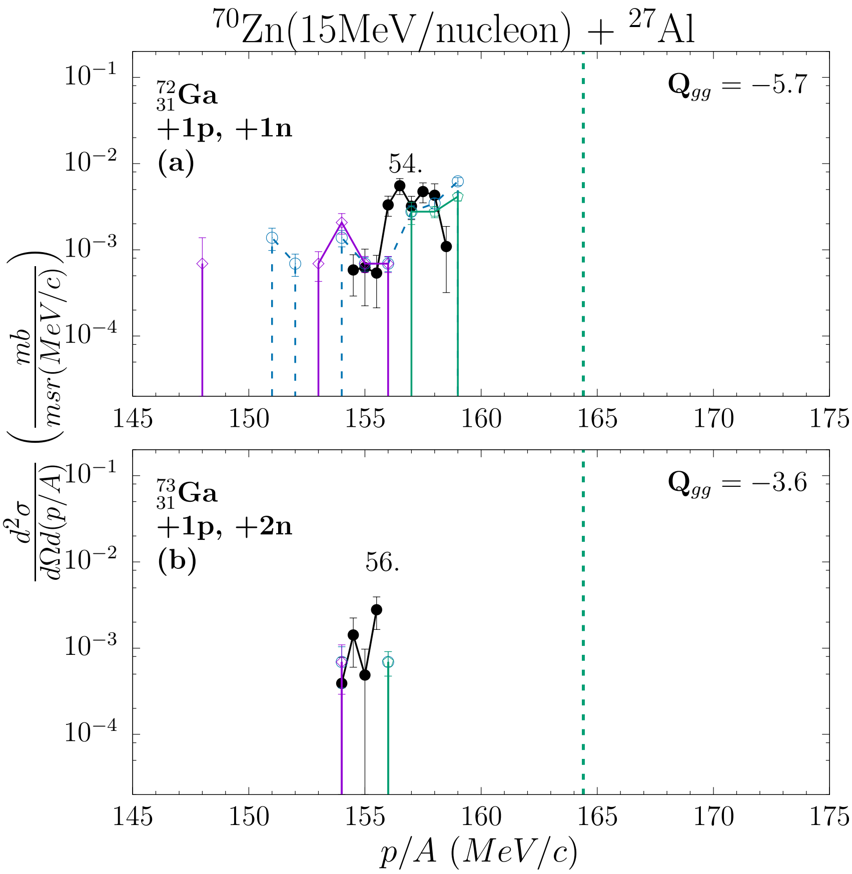

Figure A.8: Momentum per nucleon distributions of ejectiles from cluster channels of the reaction ^{70}Zn (15 MeV/nucleon) + ^{27}Al. The experimental data are shown by closed (black) circles. The vertical dashed (green) line is the p/A of the projectile. The DIT calculation is shown by open (blue) circles. The three components of the DIT distribution, namely QP-0n, QP-1n and QP-2n, are also shown with open (green) squares, open (purple) diamonds and, open (yellow) triangles, respectively, as in Fig. A.3b.

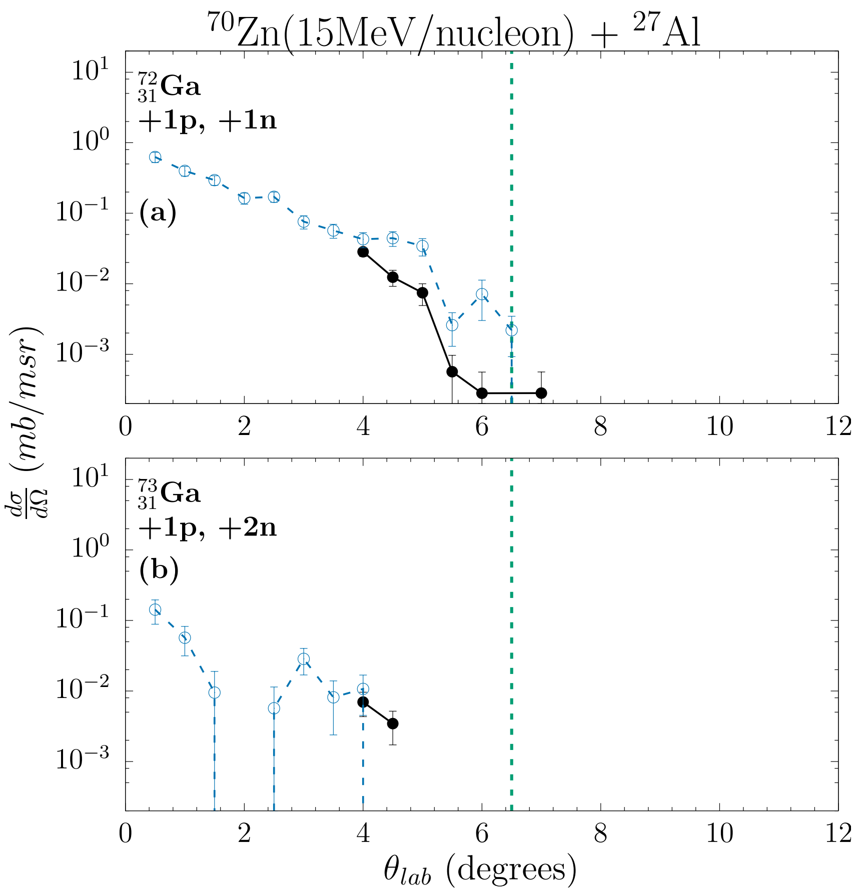

Figure A.9: Angular distributions of ejectiles from cluster transfer channels of the reaction ^{70}Zn (15 MeV/nucleon) + ^{27}Al. The experimental data are shown by closed (black) circles. The vertical dashed (green) line shows the grazing angle. The DIT calculations are shown by open (blue) circles.

A.2.2.4 Incomplete Fusion Ejectiles

In the final set of figures, Fig. A.10 and Fig. A.11, we present the momentum distribution and the respective angular distribution of products that are expected to arise from incomplete fusion.

Overall, it is evident that these channels exhibit a similar pattern in their p/A spectra, characterized by a quasielastic peak and also a distinct secondary peak at lower p/A values. Notably, the DIT calculations fail to adequately reproduce the experimental data, as the DIT model lacks an inherent mechanism to account for the incomplete fusion process.

Standing on the angular distributions, it can be observed that the experimental data, represented by closed black circles, were derived from the integration of the entire p/A distribution.

Additionally, for the case of ^{68}Ga, ^{66}Zn, ^{63}Cu, distinct integrations of the quasi-elastic (QE) and deep-inelastic (DI) peaks were also performed to generate their respective angular distributions, providing insights into their contributions to the total cross section. The experimental data for the DI-only integration are represented by closed black triangles, while those for the QE-only integration are depicted using closed black squares. Notably, the DI contribution closely overlaps with the total distribution in all cases. A table is presented that includes the percentage contribution of each peak, along with the corresponding cross-section values for each integration for ^{68}Ga, as representative of the isotopes discussed in this section.

Integration Type	**Diff. Cross Section (mb/msr)**	**Contribution (%)**
Total	0.0451	-
QE	0.0126	28%
DI	0.0325	72%

Table A.1: Contributions of different integration types to the differential cross section for the ^{68}Ga isotope.

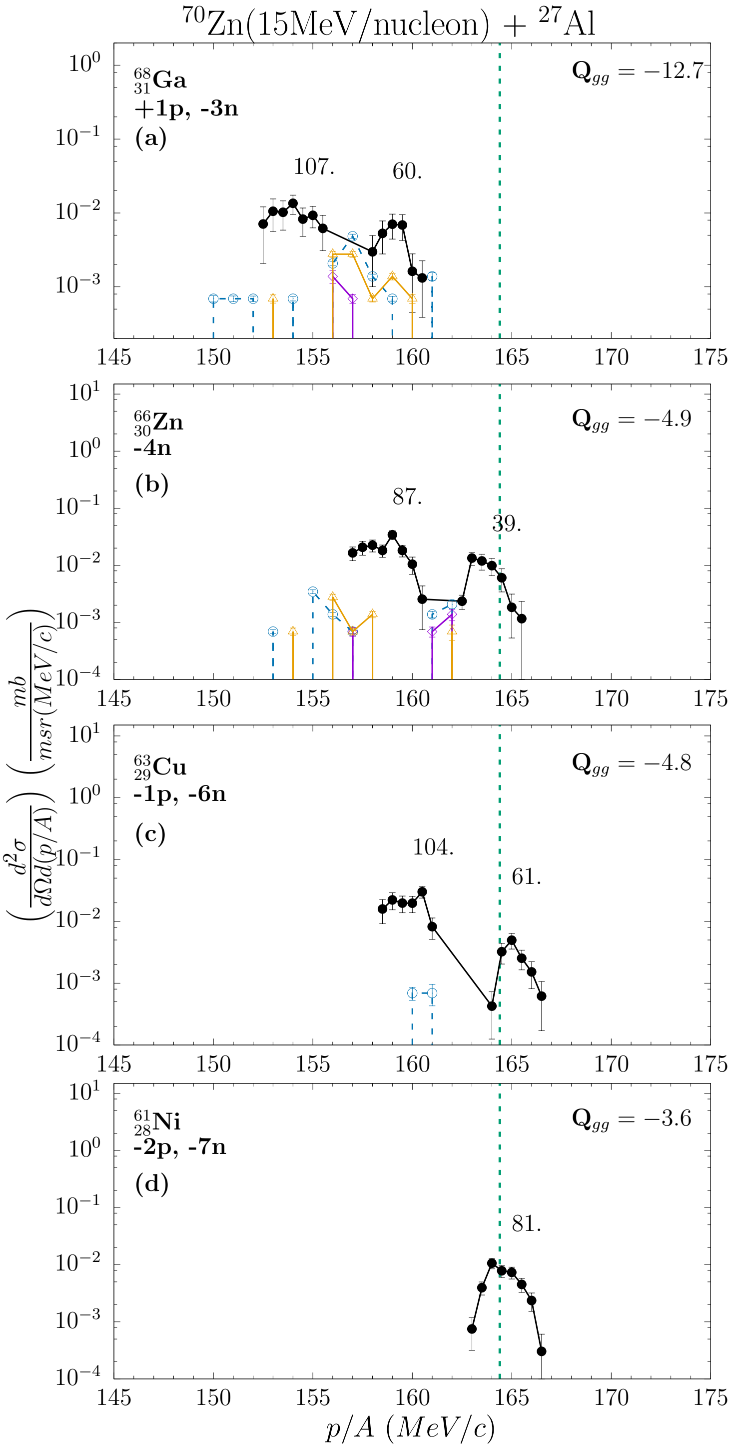

Figure A.10: Momentum per nucleon distributions of ejectiles corresponding to the "left" peaks of the yield distrubutions of Fig. A.2 (indicated by red arrows) of the reaction ^{70}Zn (15 MeV/nucleon) + ^{27}Al. The experimental data are shown by closed (black) circles. The vertical dashed (green) line is the p/A of the projectile. The DIT calculation is shown by open (blue) circles. The three components of the DIT distribution, namely QP-0n, QP-1n and QP-2n, are also shown with open (green) squares, open (purple) diamonds and, open (yellow) triangles, respectively, as in Fig. A.3b.

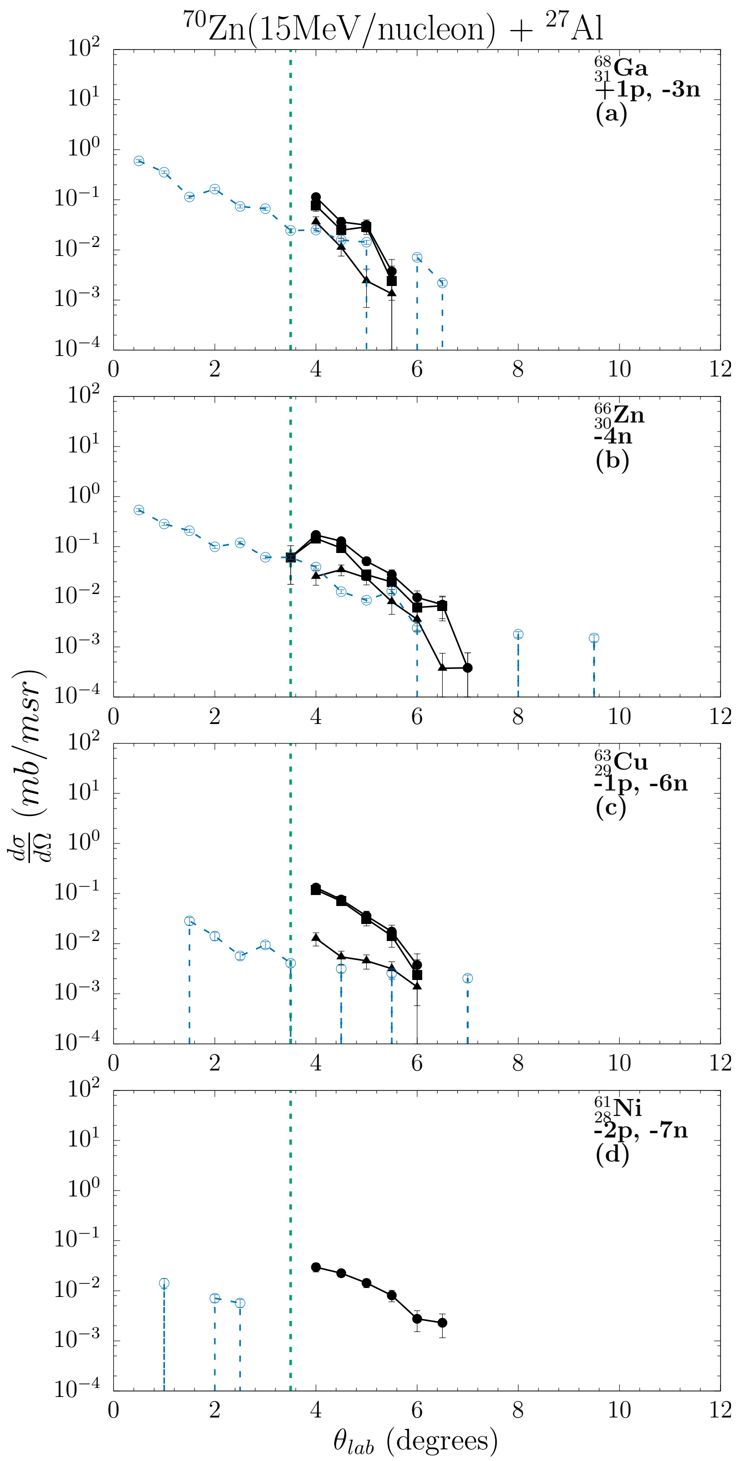

Figure A.11: Angular distributions of ejectiles corresponding to the "left" peaks of the yield distrubutions of Fig. A.2 (indicated by red arrows) of the reaction ^{70}Zn (15 MeV/nucleon) + ^{27}Al. The total experimental data are shown by closed (black) circles, with the DI-only and QE-only integrations represented by closed black triangles and squares, respectively. The vertical dashed (green) line indicates the grazing angle. The DIT calculations are shown by open (blue) circles. The relative contributions of QE and DI to the total cross-section are shown in Table A.1.

A.3 Conclusions

The results from this run provide a valuable reaffirmation of the particle identification approach and analysis employed in this work. This outcome gives confidence that the analysis represents an advancement in the study of peripheral reactions involving medium-mass nuclei in the Fermi energy regime. Looking ahead, conducting more extensive experimental runs with a light target, similar to the one used in this run, could offer deeper insights into the reaction mechanisms at play in this energy regime. Such studies may further clarify the role of incomplete fusion in the reaction mechanism and in the production of neutron-deficient ejectiles.

Furthermore, the present data provide motivation for the use of the CoMD code to describe the incomplete/complete fusion component of the reaction mechanism at this energy regime and its possible dependence on the compressibility and the symmetry energy parameters of the effective interaction implemented in the CoMD code. These studies lie outside the scope of the present work but constitute an interesting project to be undertaken for the near future.

Appendix B
Supplementary Material for the Ejectile Distributions of the ^{70}Zn (15 MeV/nucleon) + ^{64}Ni Reaction

B.1 Introduction

In this appendix, we present supplementary material for the ZnNi run set, corresponding to the reaction of ^{70}Zn with ^{64}Ni at 15 MeV/nucleon. This extra material provides additional context and a broader overview of the main results discussed in the thesis. First, in Fig. B.1, we show the mass distributions of elements with Z = 26–32. This figure represents the totality of the identified isotopes in this work for the specific run set. Compared to the mass distributions that were shown in Chapter 5 of this work, this figure also includes the isotopes of the elements Co (Z = 27) and Fe (Z = 26), presenting only the experimental data. In the case of Co and Fe in this experimental run, we observe a lack of collection of neutron-rich isotopes. Additionally, the Co data deviates from the typical bell-shaped pattern seen in most elements' distributions. This anomaly may be attributed to potential issues with the software gating of these isotopes during the data analysis process.

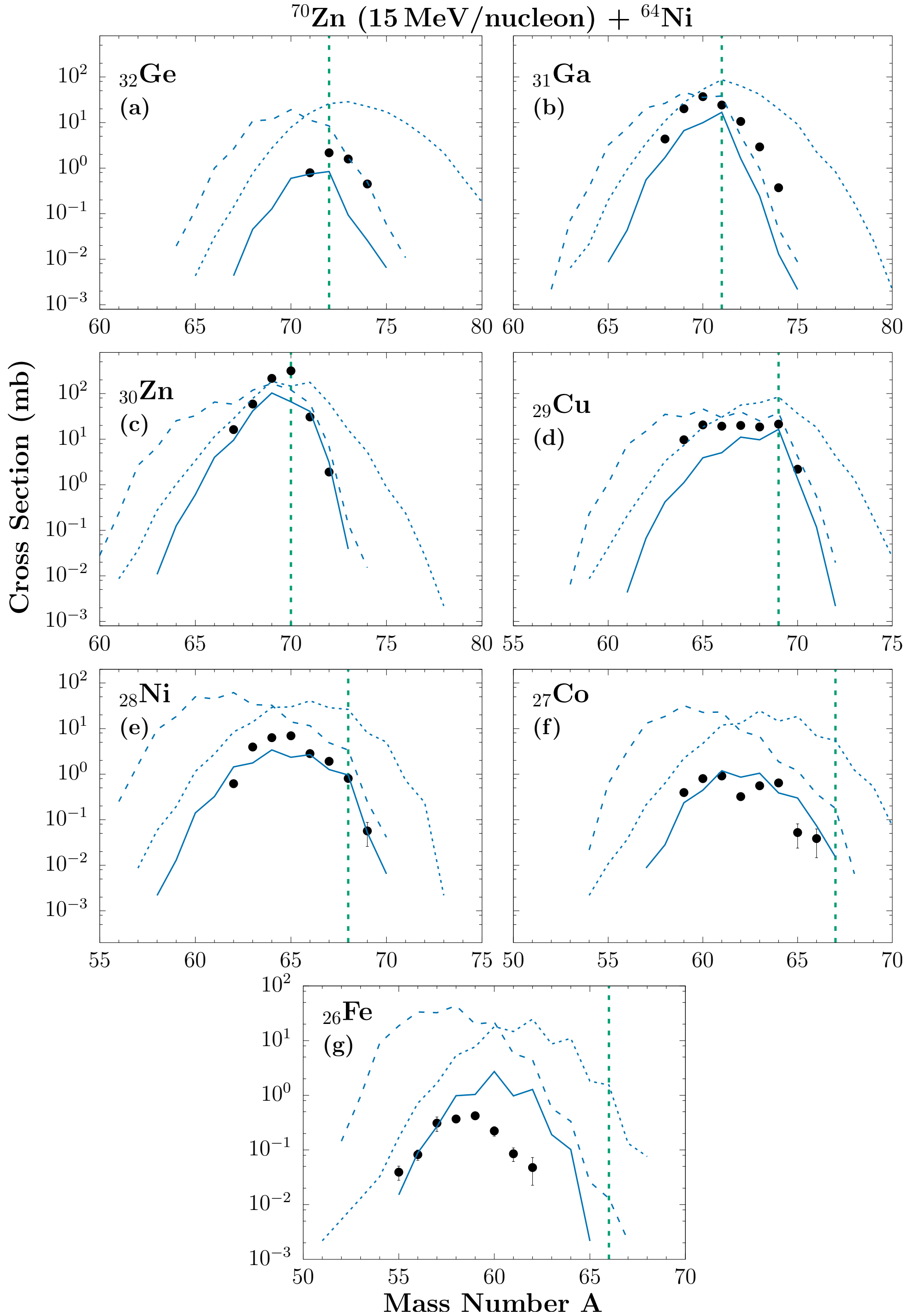

Figure B.1: Mass distributions (cross sections) of elements with Z = 26-32 from the reaction ^{70}Zn (15 MeV/nucleon) + ^{64}Ni. The experimental data are shown by closed (black) circles. The vertical dashed (green) line indicates the initiation of neutron pickup. The DIT calculations are shown as follows: primary fragments with dotted (blue) line, final (cold) fragments with dashed (blue) line, and final fragments filtered for acceptance with the solid (blue) line (as presented in Chapter 5 of this thesis).

B.2 Momentum and Angular Distribution Overview by Element

In this section of the appendix, we have proceeded to present the momentum distributions of the identified isotopes of this work for all observed elements, along with their respective angular distributions for completeness. While some of these reaction channels have already been discussed in the results chapter of the thesis, this comprehensive presentation serves as a 'repository' to showcase the ejectile distributions for all observed reaction channels. It is worth noting that, only a selected subset of channels is included, as the results—particularly for Co (see Fig. B.1)—did not warrant further detailed analysis.

The ejectile distributions for the isotopes of elements with Z ranging from 32 to 26 are presented in the following figures of this appendix, from Fig. B.2 to Fig. B.15, in the respective order. The method of presentation, is similar to that already seen in as presented in Chapter 5, as well as in Appendix A. For the p/A distributions, the experimental data are represented by closed points, while the vertical dashed line marks the p/A value of the projectile (164.4 MeV/c). The horizontal axis is scaled in increments of 0.5 MeV/c. We need to remind here that, the numbers above some of the peaks yield the total excitation energy of the binary quasiprojectile-quasitarget system obtained using the indicated p/A values and employing binary kinematics. The excitation energy is connected to the reaction Q-value as $E^*_{tot} = Q_{gg} - Q$, where Q_{gg} is the ground-state to ground-state Q-value of the channel, reported on the right side of each p/A figure.

In the angular distributions, the experimental data are represented by closed points, while the vertical dashed line indicates the grazing angle θ_{gr} = 6.5°.

Along with the experimental data, theoretical calculations are also presented. The standard DIT calculation is shown with open (blue) circles, while the CoMD calculation is represented by open (red) squares. In addition to the standard DIT calculation, the QP-$\lambda\, n$ analysis of the DIT results is also included.

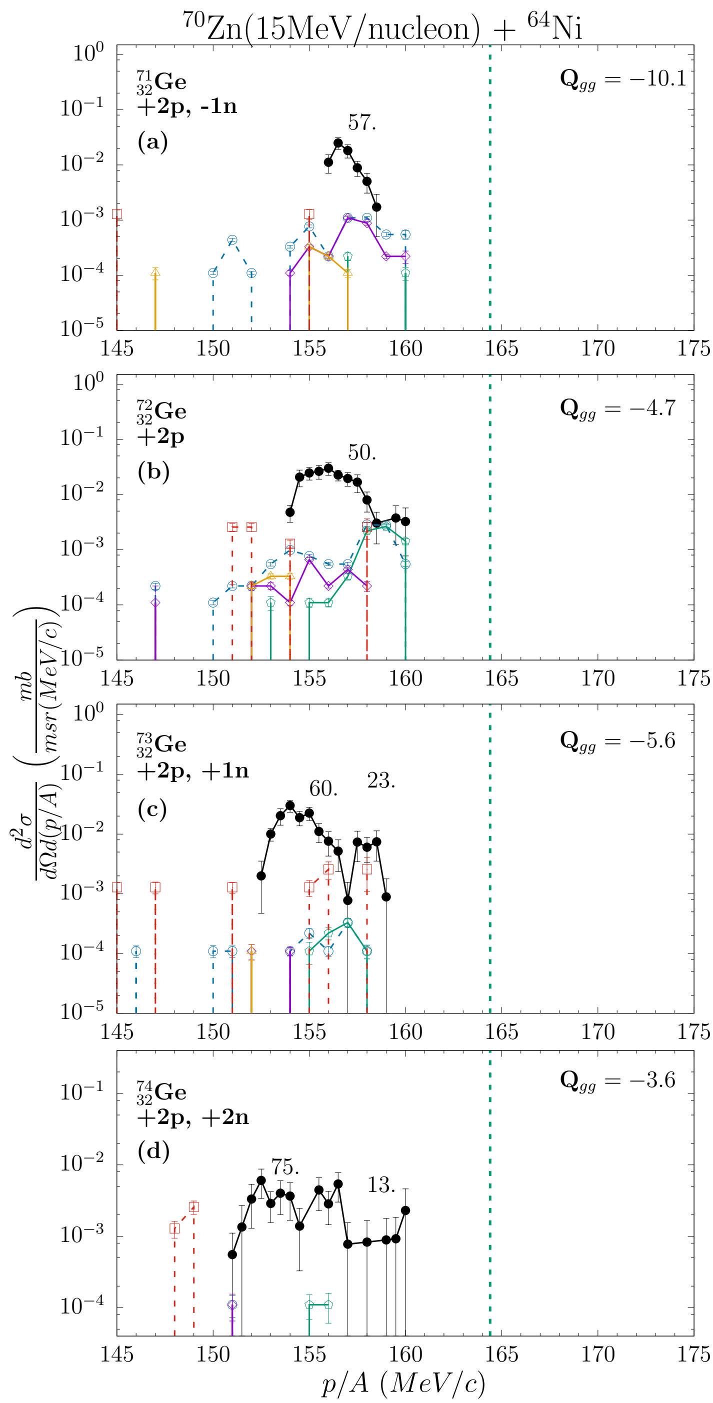

Figure B.2: Momentum per nucleon distributions of various identified isotopes of Ge (Z=32). The experimental data are shown by closed (black) circles. The vertical dashed (green) line represents the p/A of the projectile. The numbers above some peaks give the total excitation energy (in MeV) obtained from binary kinematics using the corresponding p/A values. The CoMD calculation is shown by open (red) squares, while the DIT calculation is shown by open (blue) circles. The three components of the DIT distribution, namely QP-0n, QP-1n and QP-2n, are also shown with open (green) squares, open (purple) diamonds and, open (yellow) triangles, respectively, as in Chapter 5 of this thesis.

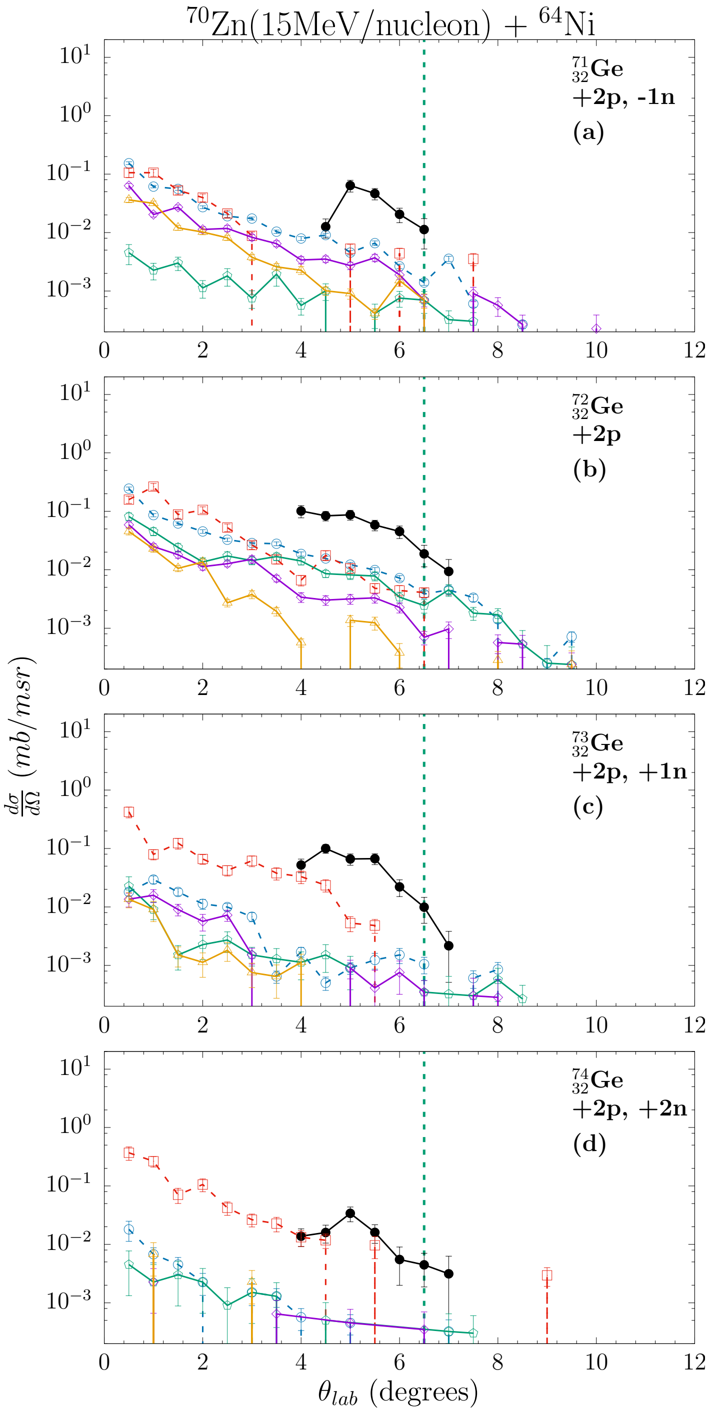

Figure B.3: Angular distributions of various identified isotopes of Ge (Z=32). The experimental data are shown by closed (black) circles. The vertical dashed (green) line shows the grazing angle. The CoMD calculation is shown by open (red) squares, while the DIT calculation is shown by open (blue) circles. The three components of the DIT distribution, namely QP-0n, QP-1n and QP-2n, are also shown with open (green) squares, open (purple) diamonds and, open (yellow) triangles, respectively, as in Chapter 5 of this thesis.

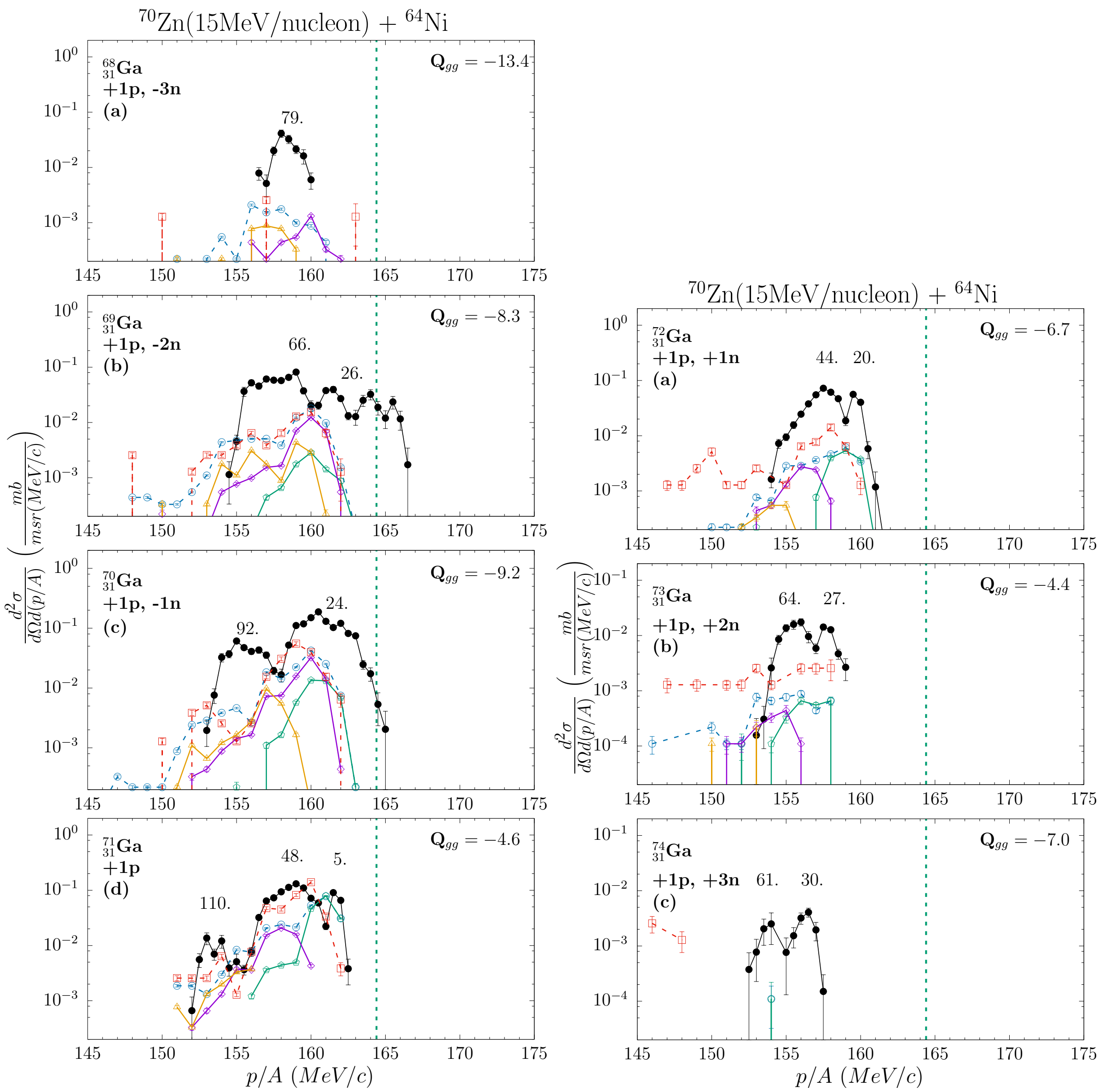

Figure B.4: Momentum per nucleon distributions of various identified isotopes of Ga (Z=31). The experimental data are shown by closed (black) circles. The vertical dashed (green) line represents the p/A of the projectile. The numbers above some peaks give the total excitation energy (in MeV) obtained from binary kinematics using the corresponding p/A values. The CoMD calculation is shown by open (red) squares, while the DIT calculation is shown by open (blue) circles. The three components of the DIT distribution, namely QP-0n, QP-1n and QP-2n, are also shown with open (green) squares, open (purple) diamonds and, open (yellow) triangles, respectively, as in Chapter 5 of this thesis.

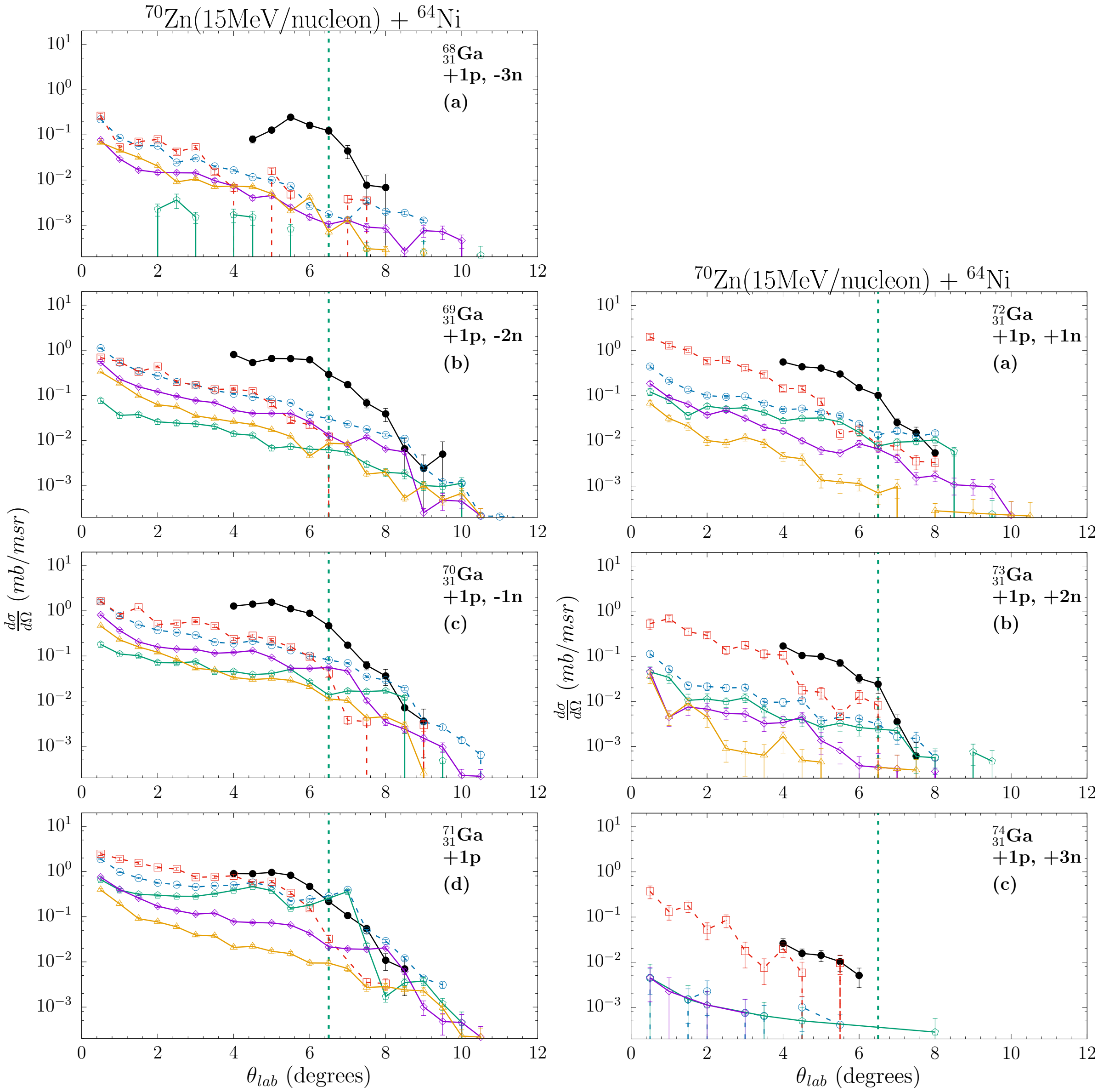

Figure B.5: Angular distributions of various identified isotopes of Ga (Z=31). The experimental data are shown by closed (black) circles. The vertical dashed (green) line shows the grazing angle. The CoMD calculation is shown by open (red) squares, while the DIT calculation is shown by open (blue) circles. The three components of the DIT distribution, namely QP-0n, QP-1n and QP-2n, are also shown with open (green) squares, open (purple) diamonds and, open (yellow) triangles, respectively, as in Chapter 5 of this thesis.

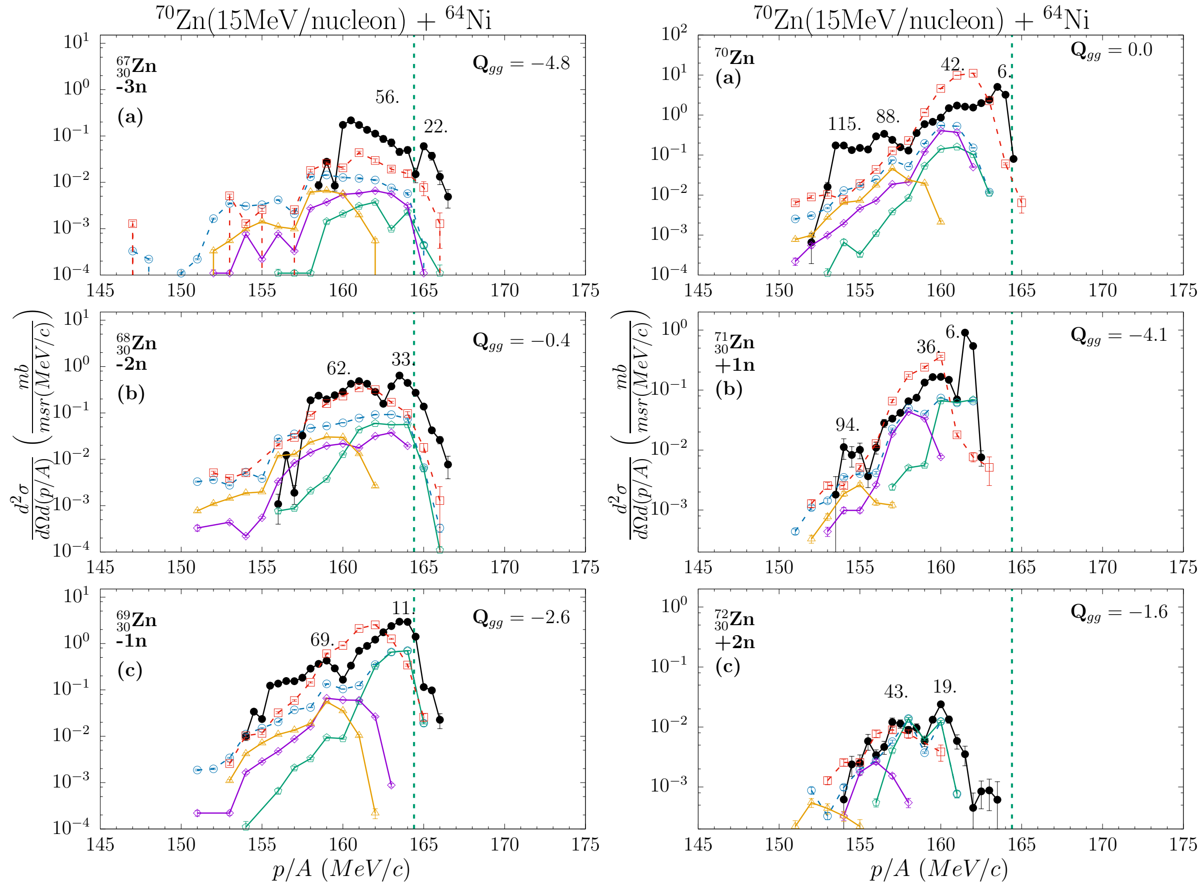

Figure B.6: Momentum per nucleon distributions of various identified isotopes of Zn (Z=30). The experimental data are shown by closed (black) circles. The vertical dashed (green) line represents the p/A of the projectile. The numbers above some peaks give the total excitation energy (in MeV) obtained from binary kinematics using the corresponding p/A values. The CoMD calculation is shown by open (red) squares, while the DIT calculation is shown by open (blue) circles. The three components of the DIT distribution, namely QP-0n, QP-1n and QP-2n, are also shown with open (green) squares, open (purple) diamonds and, open (yellow) triangles, respectively, as in Chapter 5 of this thesis.

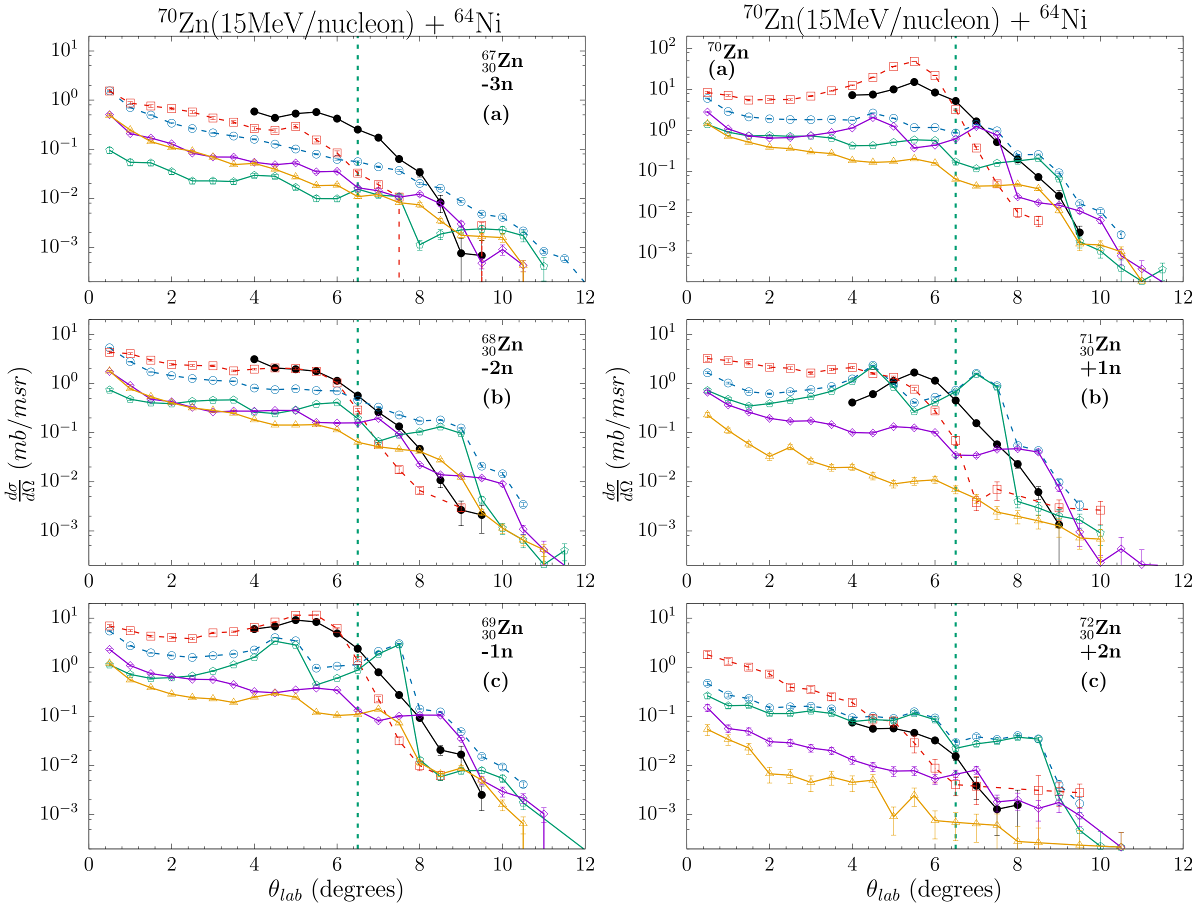

Figure B.7: Angular distributions of various identified isotopes of Zn (Z=30). The experimental data are shown by closed (black) circles. The vertical dashed (green) line shows the grazing angle. The CoMD calculation is shown by open (red) squares, while the DIT calculation is shown by open (blue) circles. The three components of the DIT distribution, namely QP-0n, QP-1n and QP-2n, are also shown with open (green) squares, open (purple) diamonds and, open (yellow) triangles, respectively, as in Chapter 5 of this thesis.

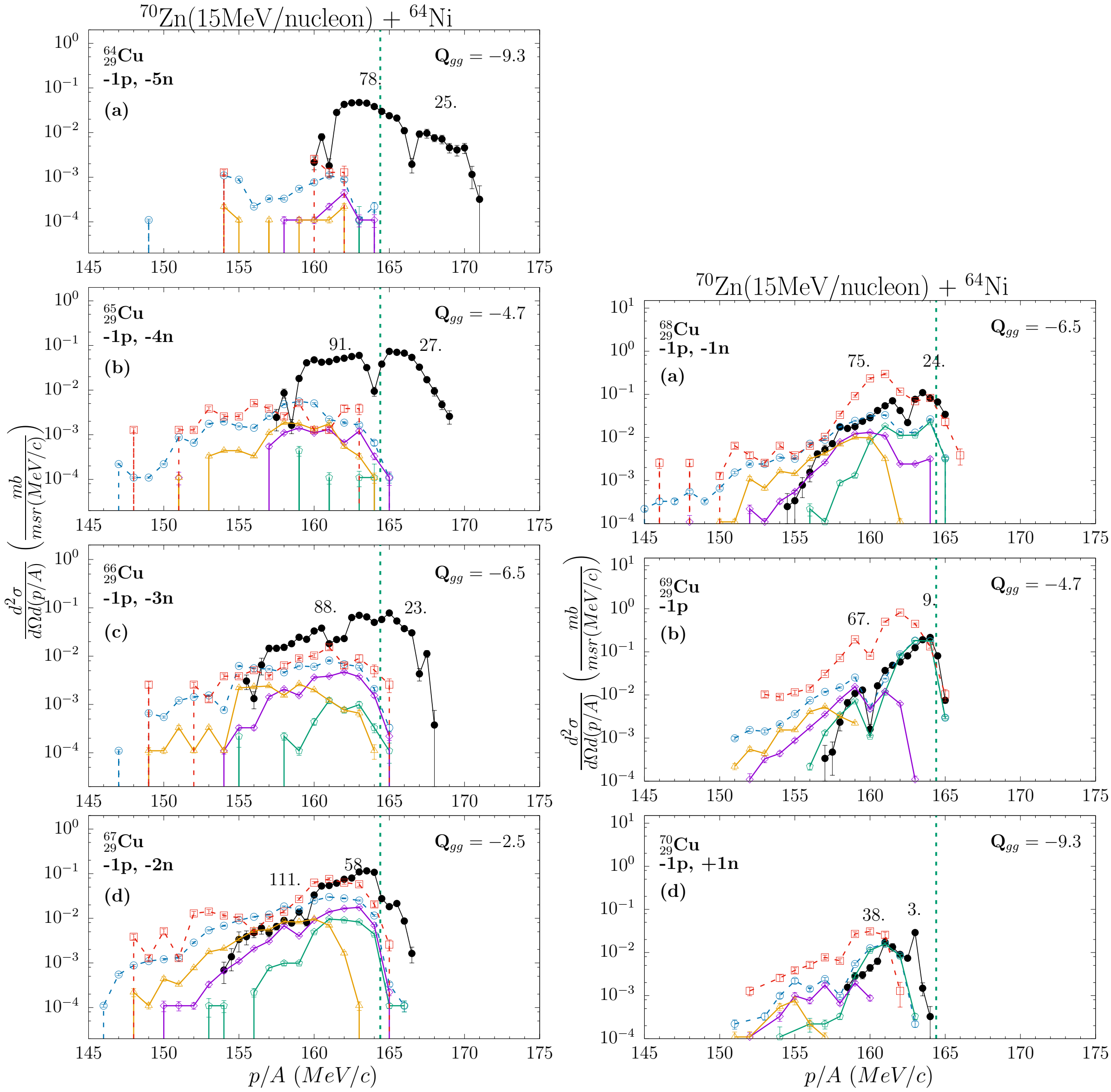

Figure B.8: Momentum per nucleon distributions of various identified isotopes of Cu (Z=29). The experimental data are shown by closed (black) circles. The vertical dashed (green) line represents the p/A of the projectile. The numbers above some peaks give the total excitation energy (in MeV) obtained from binary kinematics using the corresponding p/A values. The CoMD calculation is shown by open (red) squares, while the DIT calculation is shown by open (blue) circles. The three components of the DIT distribution, namely QP-0n, QP-1n and QP-2n, are also shown with open (green) squares, open (purple) diamonds and, open (yellow) triangles, respectively, as in Chapter 5 of this thesis.

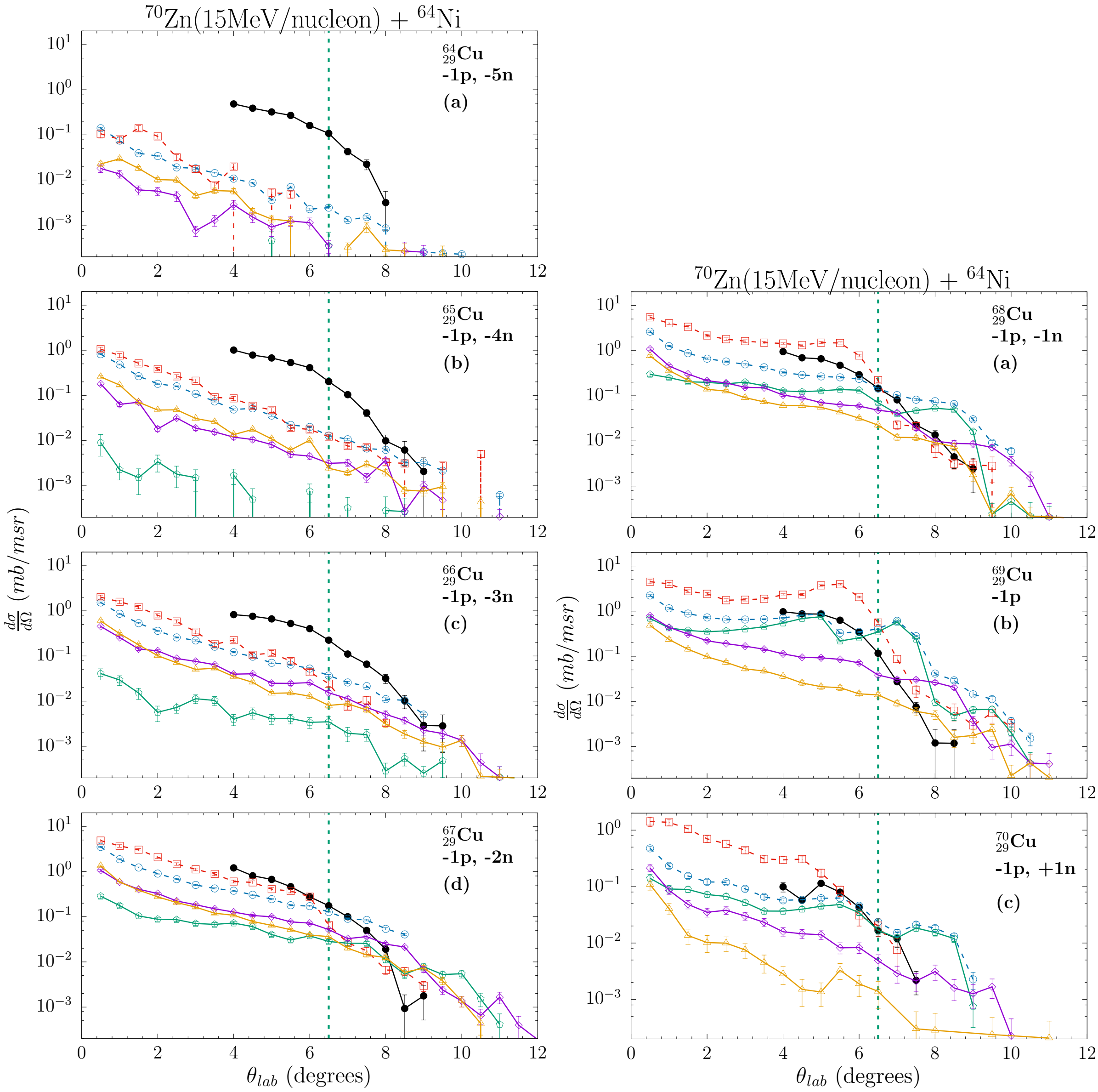

Figure B.9: Angular distributions of various identified isotopes of Cu (Z=29). The experimental data are shown by closed (black) circles. The vertical dashed (green) line shows the grazing angle. The CoMD calculation is shown by open (red) squares, while the DIT calculation is shown by open (blue) circles. The three components of the DIT distribution, namely QP-0n, QP-1n and QP-2n, are also shown with open (green) squares, open (purple) diamonds and, open (yellow) triangles, respectively, as in Chapter 5 of this thesis.

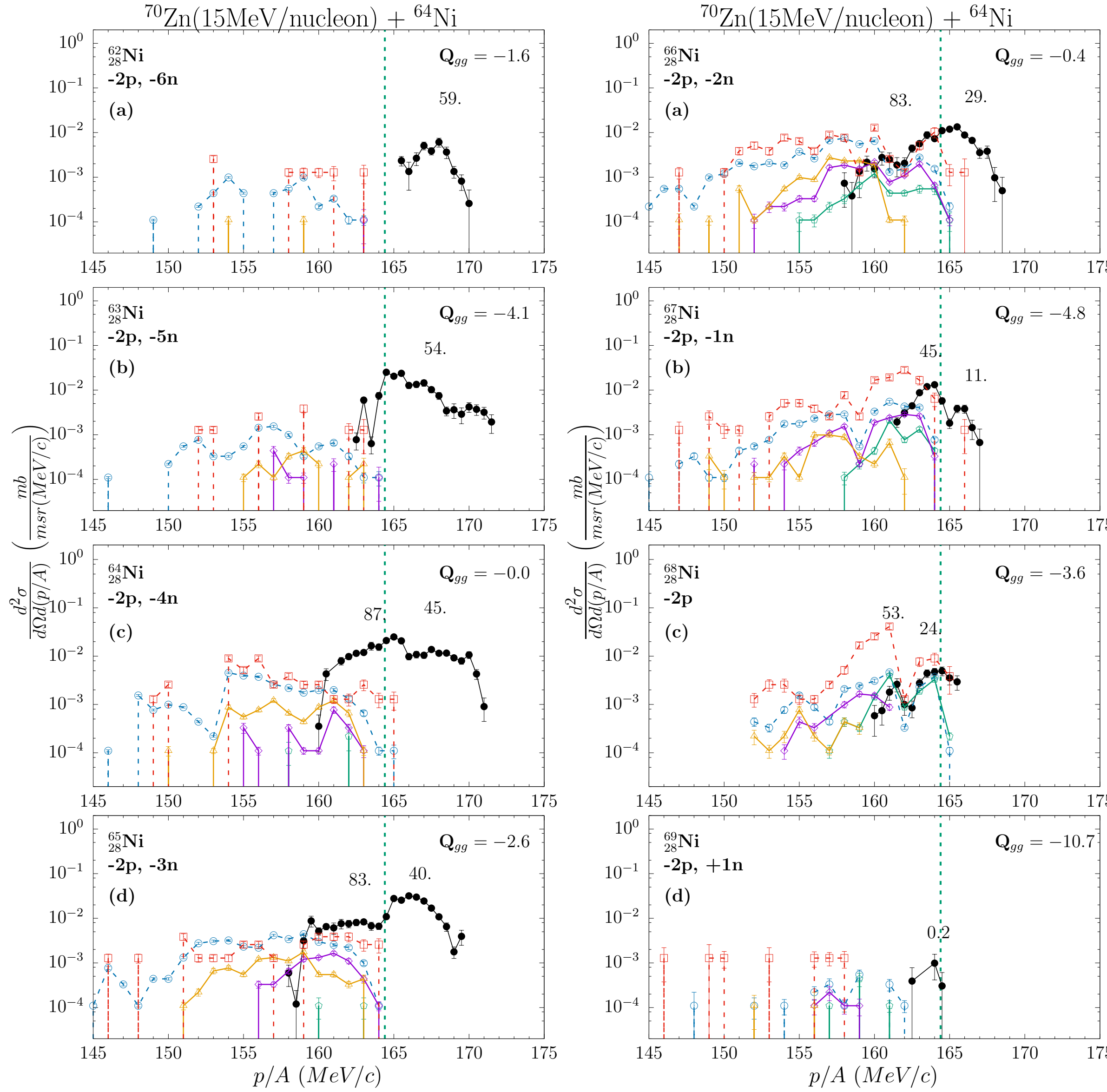

Figure B.10: Momentum per nucleon distributions of various identified isotopes of Ni (Z=28). The experimental data are shown by closed (black) circles. The vertical dashed (green) line represents the p/A of the projectile. The numbers above some peaks give the total excitation energy (in MeV) obtained from binary kinematics using the corresponding p/A values. The CoMD calculation is shown by open (red) squares, while the DIT calculation is shown by open (blue) circles. The three components of the DIT distribution, namely QP-0n, QP-1n and QP-2n, are also shown with open (green) squares, open (purple) diamonds and, open (yellow) triangles, respectively, as in Chapter 5 of this thesis.

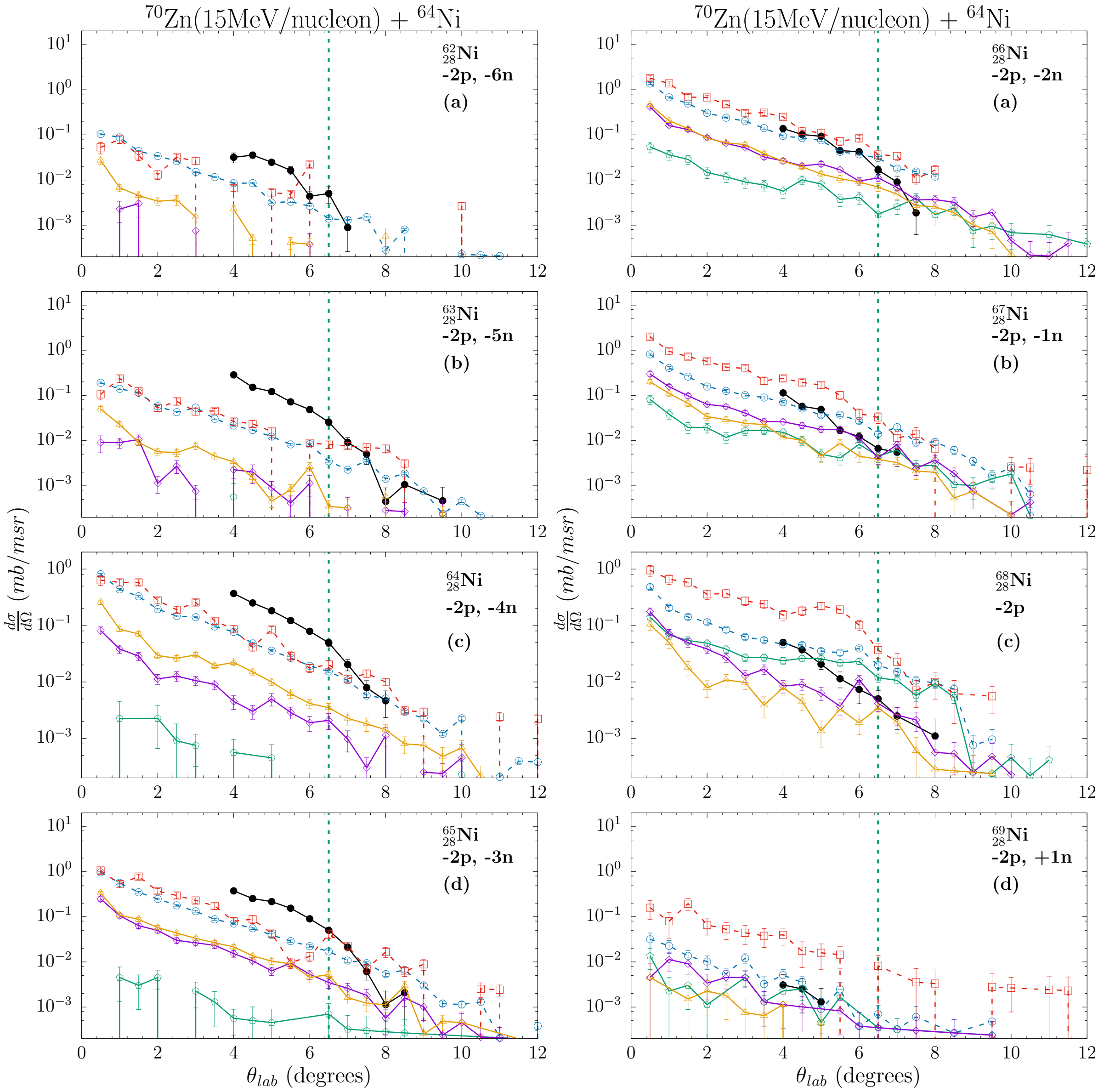

Figure B.11: Angular distributions of various identified isotopes of Ni (Z=28). The experimental data are shown by closed (black) circles. The vertical dashed (green) line shows the grazing angle. The CoMD calculation is shown by open (red) squares, while the DIT calculation is shown by open (blue) circles. The three components of the DIT distribution, namely QP-0n, QP-1n and QP-2n, are also shown with open (green) squares, open (purple) diamonds and, open (yellow) triangles, respectively, as in Chapter 5 of this thesis.

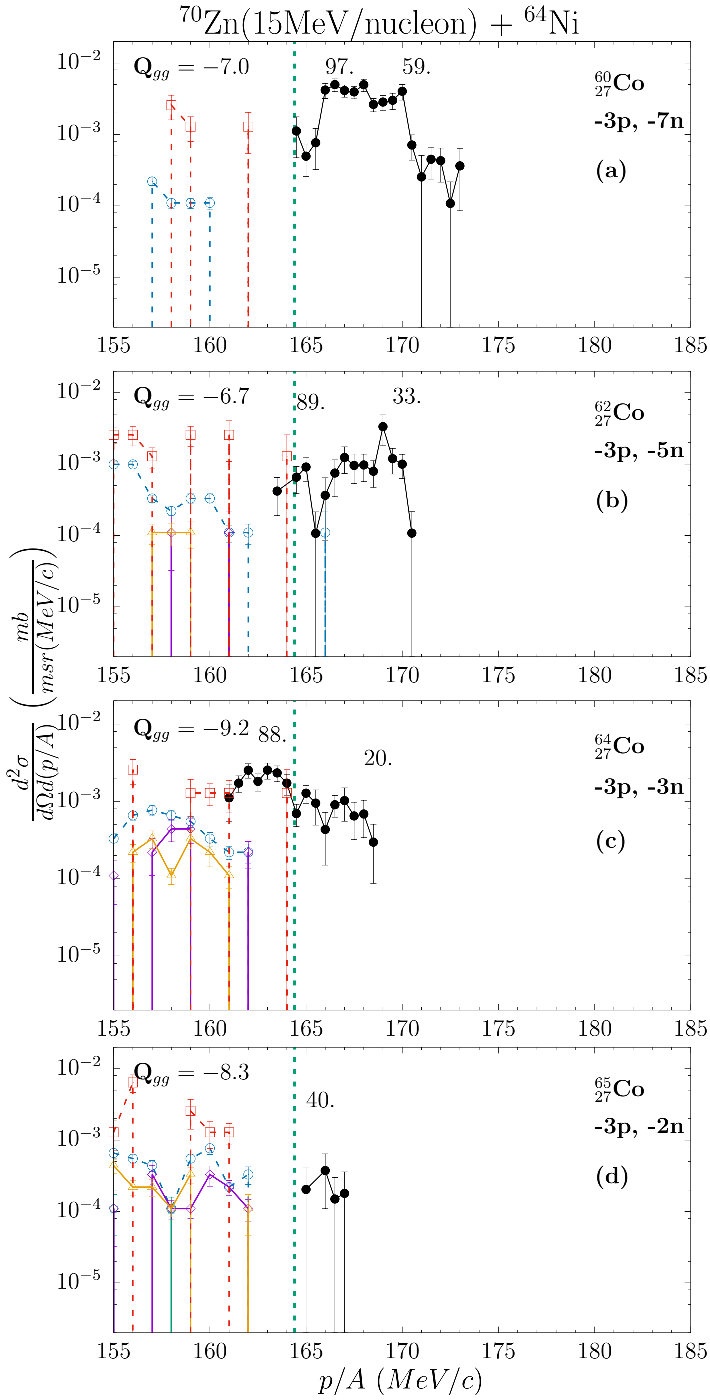

Figure B.12: Momentum per nucleon distributions of various identified isotopes of Co (Z=27). The experimental data are shown by closed (black) circles. The vertical dashed (green) line represents the p/A of the projectile. The numbers above some peaks give the total excitation energy (in MeV) obtained from binary kinematics using the corresponding p/A values. The CoMD calculation is shown by open (red) squares, while the DIT calculation is shown by open (blue) circles. The three components of the DIT distribution, namely QP-0n, QP-1n and QP-2n, are also shown with open (green) squares, open (purple) diamonds and, open (yellow) triangles, respectively, as in Chapter 5 of this thesis.

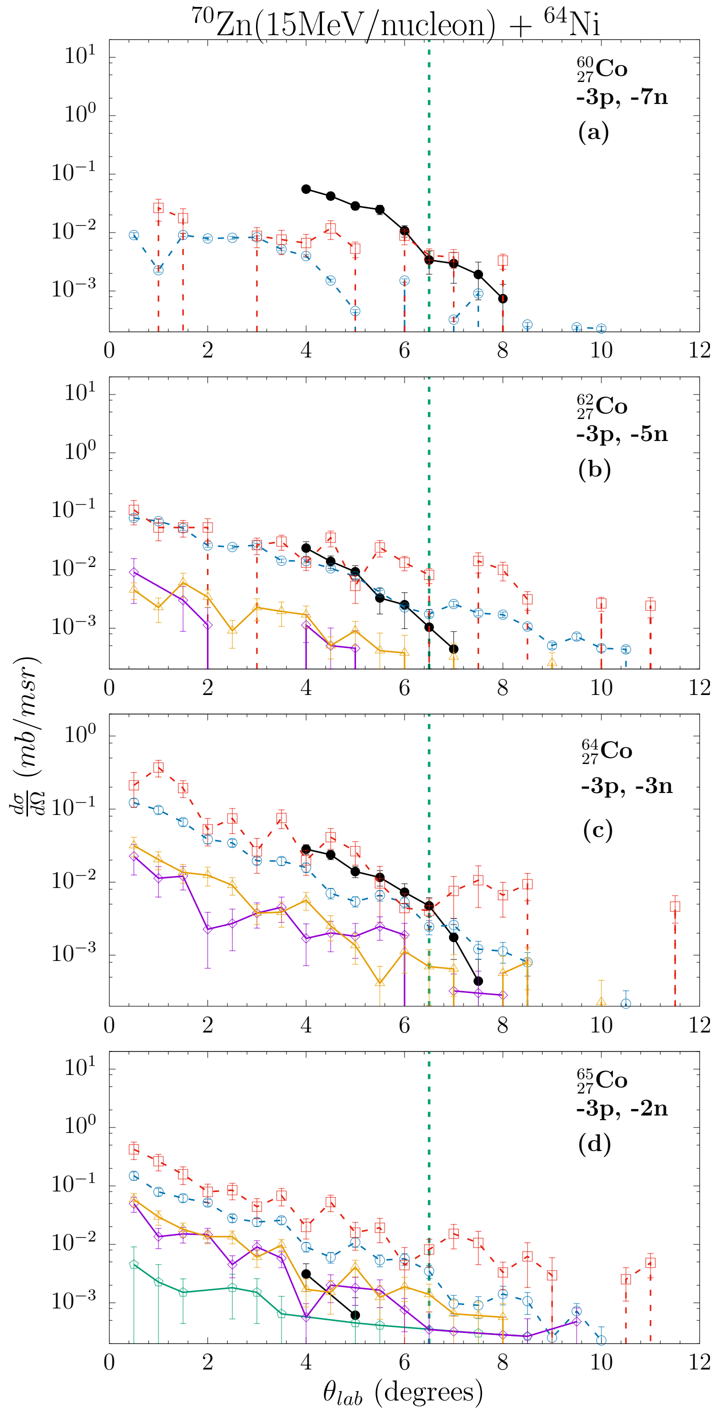

Figure B.13: Angular distributions of various identified isotopes of Co (Z=27). The experimental data are shown by closed (black) circles. The vertical dashed (green) line shows the grazing angle. The CoMD calculation is shown by open (red) squares, while the DIT calculation is shown by open (blue) circles. The three components of the DIT distribution, namely QP-0n, QP-1n and QP-2n, are also shown with open (green) squares, open (purple) diamonds and, open (yellow) triangles, respectively, as in Chapter 5 of this thesis.

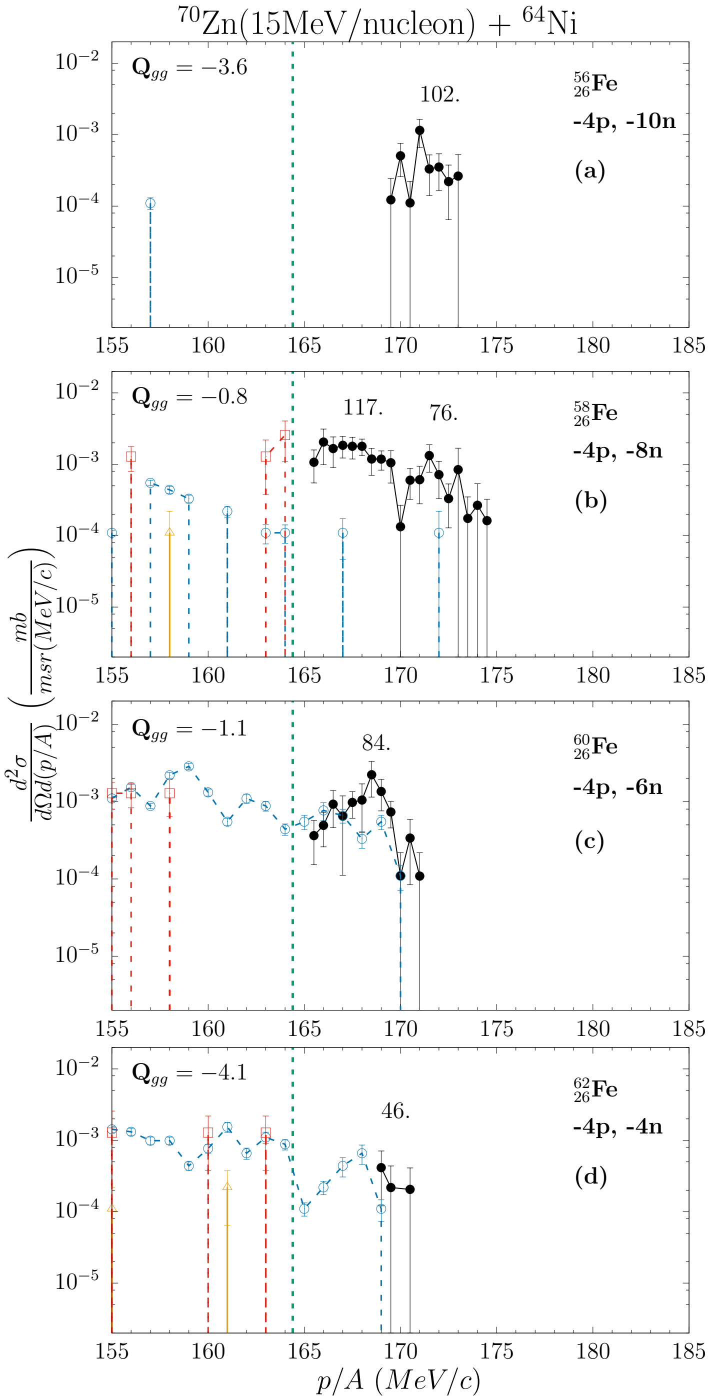

Figure B.14: Momentum per nucleon distributions of various identified isotopes of Fe (Z=26). The experimental data are shown by closed (black) circles. The vertical dashed (green) line represents the p/A of the projectile. The numbers above some peaks give the total excitation energy (in MeV) obtained from binary kinematics using the corresponding p/A values. The CoMD calculation is shown by open (red) squares, while the DIT calculation is shown by open (blue) circles. The three components of the DIT distribution, namely QP-0n, QP-1n and QP-2n, are also shown with open (green) squares, open (purple) diamonds and, open (yellow) triangles, respectively, as in Chapter 5 of this thesis.

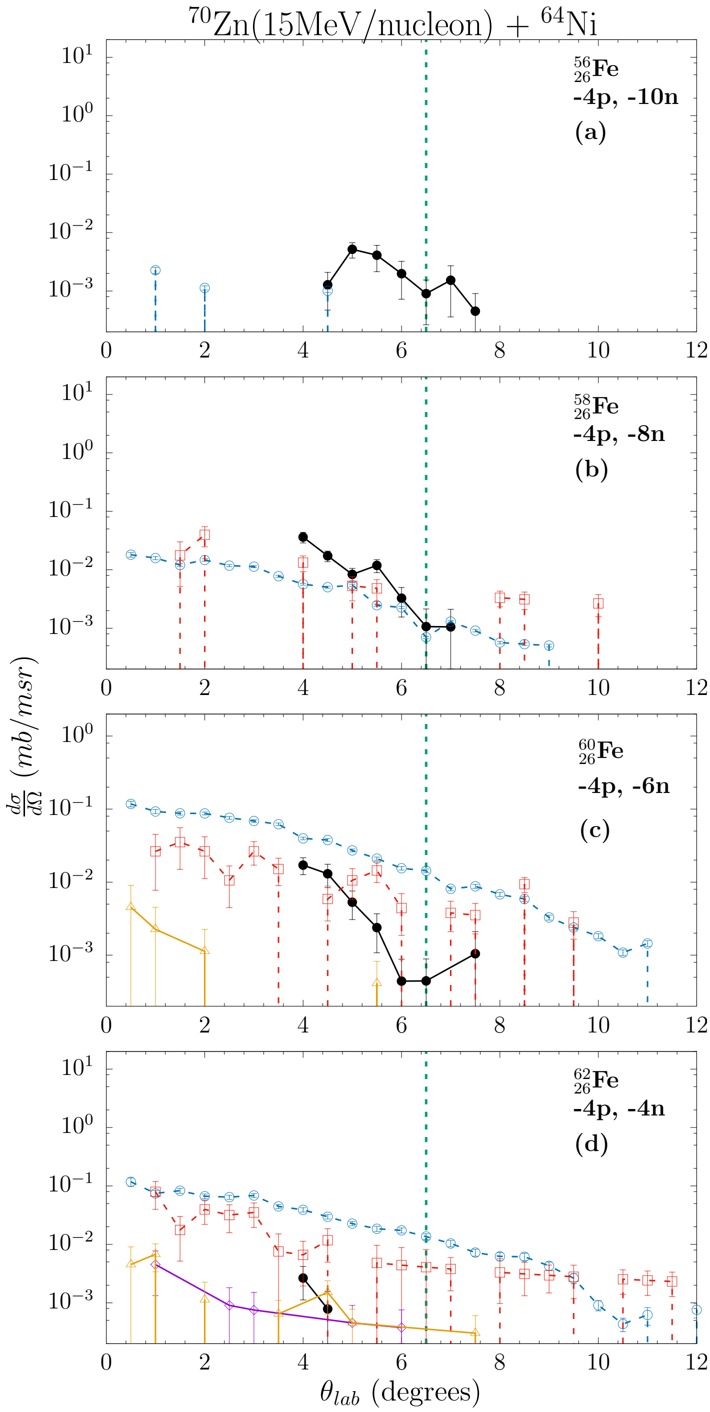

Figure B.15: Angular distributions of various identified isotopes of Fe (Z=26). The experimental data are shown by closed (black) circles. The vertical dashed (green) line shows the grazing angle. The CoMD calculation is shown by open (red) squares, while the DIT calculation is shown by open (blue) circles. The three components of the DIT distribution, namely QP-0n, QP-1n and QP-2n, are also shown with open (green) squares, open (purple) diamonds and, open (yellow) triangles, respectively, as in Chapter 5 of this thesis.

Appendix C
Analysis of Individual Run Contributions to the Experimental Distributions of the ^{70}Zn (15 MeV/nucleon) + ^{64}Ni Reaction

C.1 Introduction

In this appendix, we analyze the decomposition of the ZnNi run set into its individual runs to evaluate their respective contributions to the total distributions. As described in Chapter 2, this run set comprises three distinct runs, each conducted under the same general experimental conditions. However, variations in magnetic rigidity ($B\rho$) settings among these runs introduce differences in the obtained distributions.

Based on Table 2.1, the difference between these runs is the $B\rho$ setting of the spectrometer. Specifically, runs 64–69 were conducted at $B\rho = 1.3594$ Tm to enhance the detection of neutron-rich nuclides, while runs 22–34 and 41–61 had a lower setting of $B\rho = 1.2880$ Tm. This difference influences the range of momenta accepted by the spectrometer, thus affecting the recorded distributions.

The purpose of this analysis is to examine how the individual runs contribute to the momentum and angular distributions of the specific reaction channels most relevant to the scope of this work. By comparing the total distribution (which is the sum of all runs) with the distributions obtained from each run separately, we aim to verify the consistency of the data and evaluate any possible run-dependent effects.

In the following section, we present the momentum and angular distributions for each individual run along with a comparison with the total distribution.

C.1.1 Angular and Momentum Distributions

C.1.1.1 Inelastic Channel

In Fig. C.1, the angular and momentum distributions of ^{70}Zn ejectiles are presented. In Fig. C.1a, the angular distribution of the inelastic channel is presented. The experimental data are shown by the closed points. The vertical dashed line indicates the grazing angle θ_{gr} = 6.5° of this system. The elastically scattered projectiles have been removed by software gates.

In Fig. C.1b, the p/A distribution for the same reaction channel is depicted. The experimental data are represented by closed points, while the vertical dashed line marks the p/A value of the projectile (164.4 MeV/c). The horizontal axis is scaled in increments of 0.5 MeV/c. We remind that, the numbers above some of the peaks give the total excitation energy of the binary quasiprojectile-quasitarget system obtained using the indicated p/A values and employing binary kinematics. The excitation energy is connected to the reaction Q-value as $E^{*}_{tot} = Q_{gg} - Q$, where Q$_{gg}$ is the ground-state to ground-state Q-value of the channel, reported on the right side of each p/A figure.

This channel is once again referred to as the ”inelastic” channel, including possible complicated processes of nucleon pickup, breakup, and evaporation, which end up with no net nucleon transfer from the target to the projectile.

The experimental data, representing the combined contribution of all runs in the run set, are shown as full black points. The data corresponding to runs 22-34 are highlighted in full orange points, while runs 41-61 are depicted with full green points. Additionally, the ”neutron-rich” runs 64-69 are distinguished by full red points. This approach of data representation will be applied to all reaction channels examined in this section of the appendix.

In the inelastic channel, the most dissipative region of the total p/A distribution, below 155 MeV/c, is primarily described by Runs 22-34 and 41-61, while Runs 64-69 do not provide significant contributions in this region. Additionally, a distinct peak in the angular distribution near the grazing angle for Runs 64-69 can be attributed to the pronounced QE peak observed in the p/A spectrum.

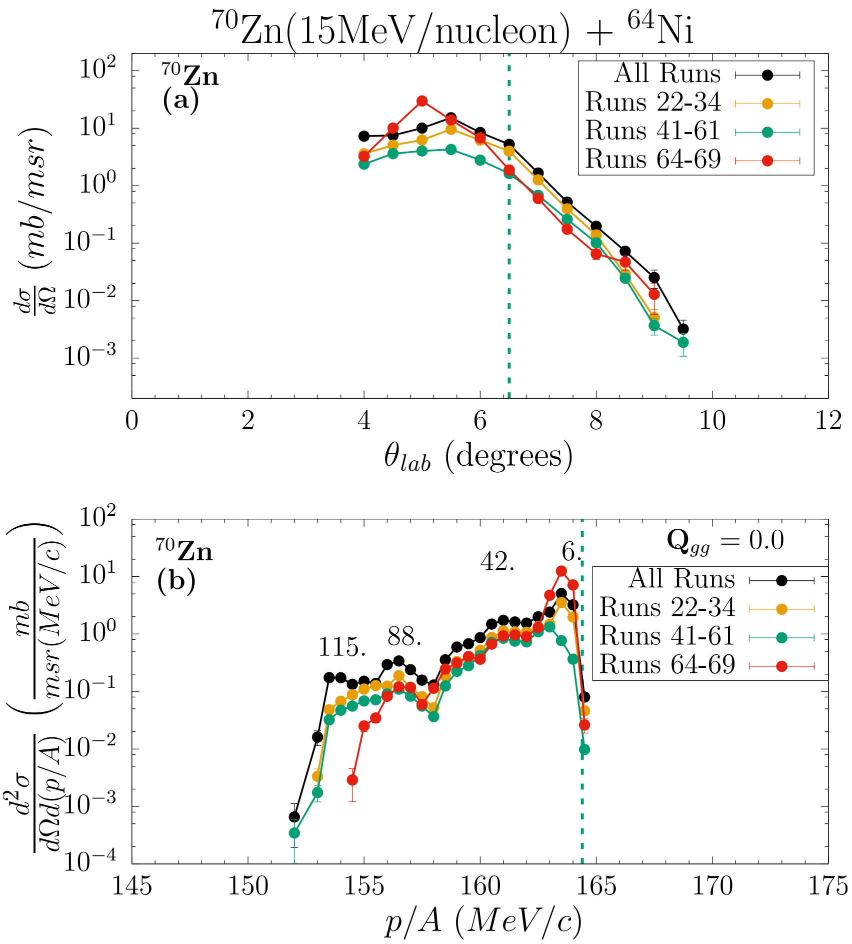

Figure C.1: (a): Angular distribution of ejectiles from the inelastic channel of the reaction ^{70}Zn (15 MeV/nucleon) + ^{64}Ni. The vertical dashed (green) line indicates the grazing angle. (b) Momentum per nucleon distribution of ejectiles from the inelastic channel. The vertical dashed (green) line represents the p/A of the projectile. The numbers above some peaks give the total excitation energy (in MeV) obtained from binary kinematics using the corresponding p/A values. In both panels, the total experimental data set is shown by full black points, while runs 22-34, 41-61, and 64-69 are represented by full orange, green, and red points, respectively.

C.1.1.2 Proton Removal and Neutron Pickup Channels

In this section, the p/A and angular distributions of important neutron-rich reaction channels are shown. In Fig. C.2, the p/A distributions of proton removal products are presented. Specifically, the products obtained from the removal of one proton (^{69}Cu) and two protons (^{68}Ni) are presented.

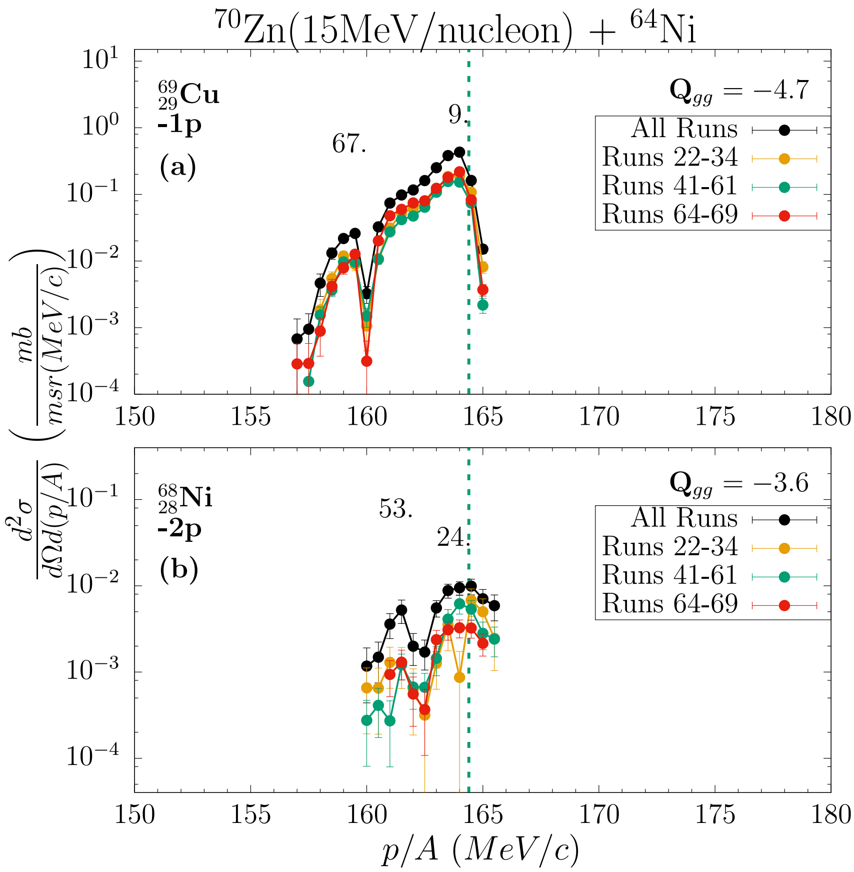

Figure C.2: Momentum per nucleon distributions of ejectiles from proton stripping channels of the reaction ^{70}Zn (15 MeV/nucleon) + ^{Ni}64. The total experimental data set is shown by full black points, while runs 22-34, 41-61, and 64-69 are represented by full orange, green, and red points, respectively. The vertical dashed (green) line is the p/A of the projectile.

In these proton removal reaction channels, the total distribution is well represented by the combined contributions of all respective runs. Similarly, the corresponding angular distributions for these channels are presented in Fig. C.3.

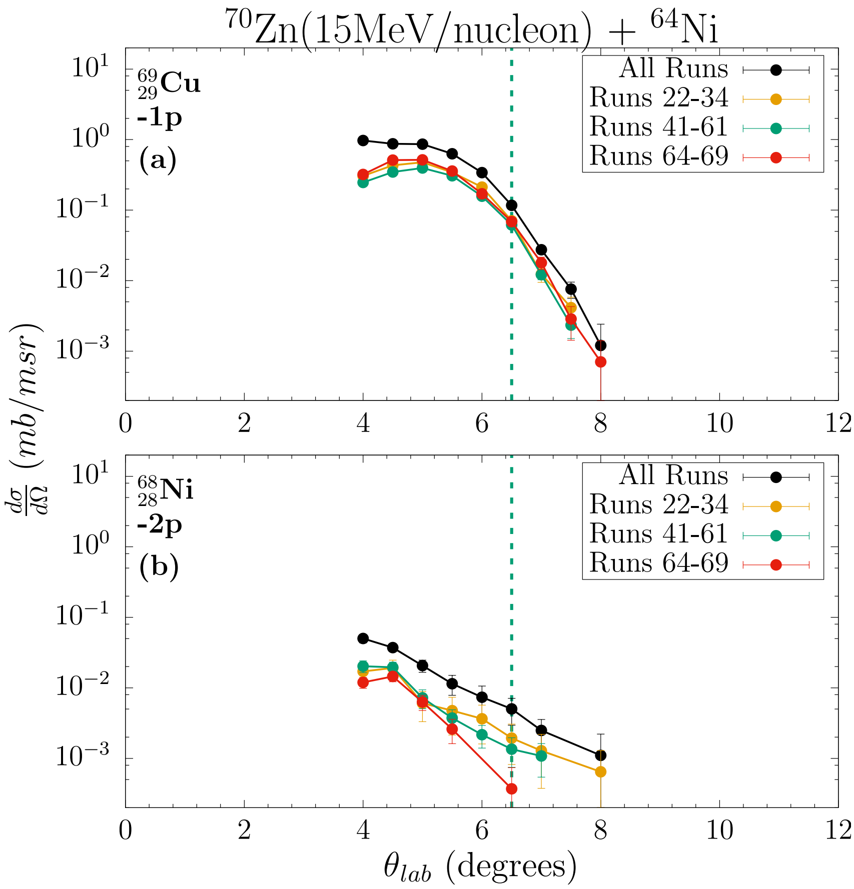

Figure C.3: Angular distributions of ejectiles from proton stripping channels of the reaction ^{70}Zn (15 MeV/nucleon) + ^{64}Ni. The total experimental data set is shown by full black points, while runs 22-34, 41-61, and 64-69 are represented by full orange, green, and red points, respectively. The vertical dashed (green) line shows the grazing angle.

In Fig. C.4, the p/A distributions of ejectiles resulting from the pickup of one (^{71}Zn) and two (^{72}Zn) neutrons from the target are presented. Notably, in the +2n channel, a distinct peak appears in the quasielastic region of the p/A spectrum from Runs 64-69. This suggests that these runs capture the direct reaction mechanism part of the distribution that contributes to the production of this neutron-rich isotope. This characteristic trend is further reflected in the angular distribution, as can be seen in Fig. C.5b, particularly in the forward-angle region below the grazing angle.

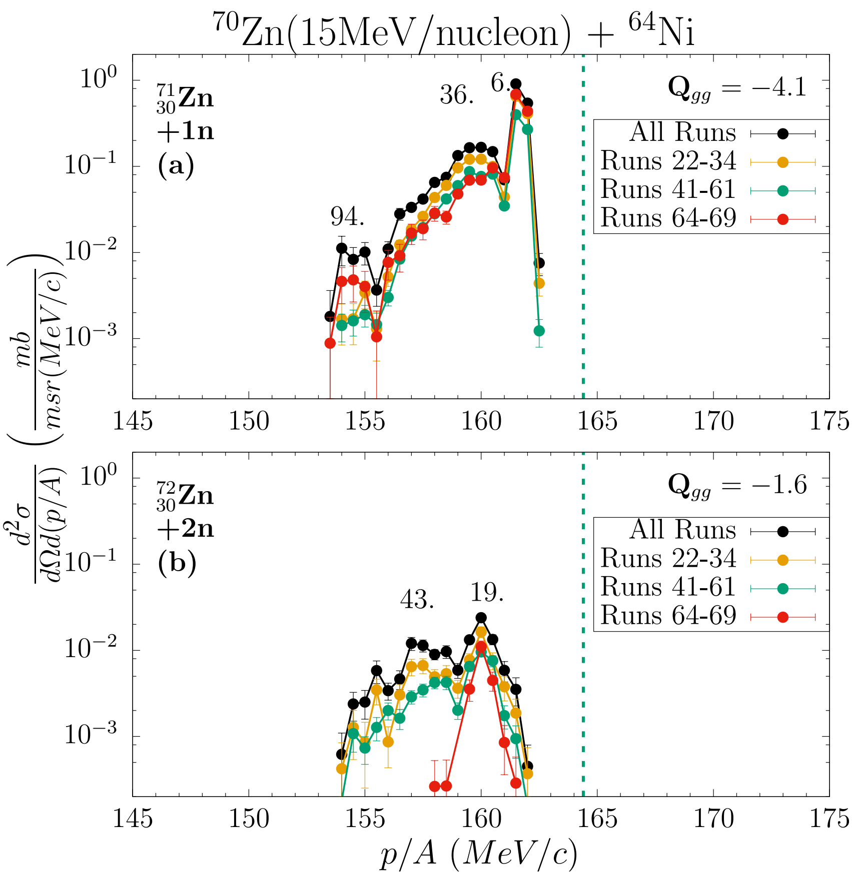

Figure C.4: Momentum per nucleon distributions of ejectiles from neutron pickup channels of the reaction ^{70}Zn (15 MeV/nucleon) + ^{64}Ni. The total experimental data set is shown by full black points, while runs 22-34, 41-61, and 64-69 are represented by full orange, green, and red points, respectively. The vertical dashed (green) line is the p/A of the projectile.

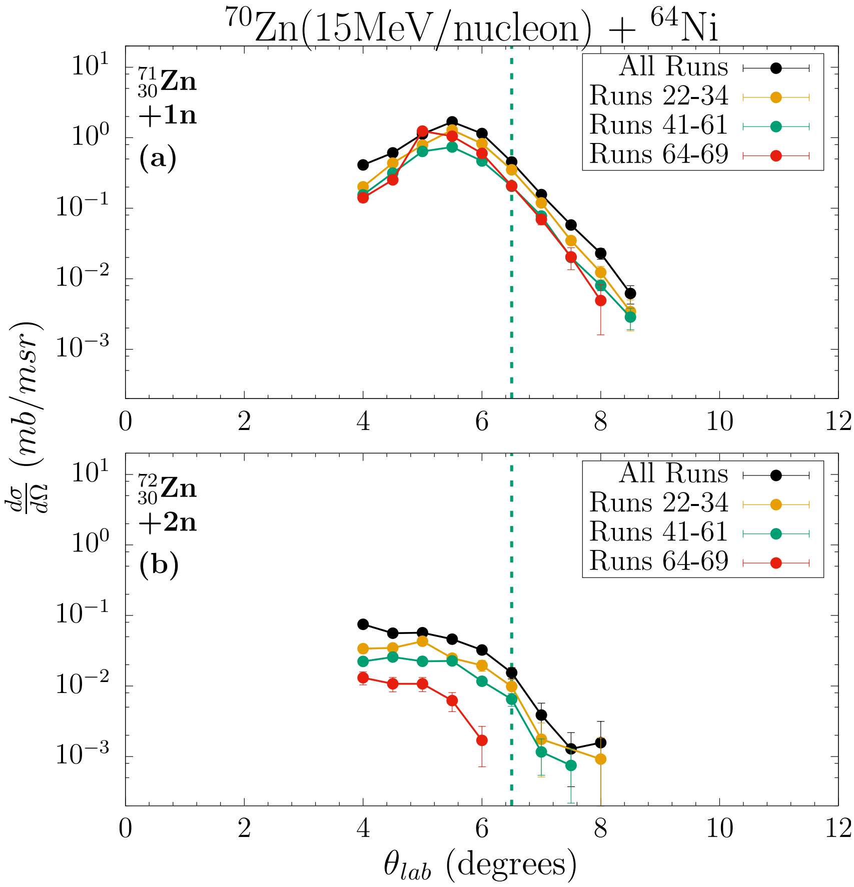

Figure C.5: Angular distributions of ejectiles from nucleon pickup channels of the reaction ^{70}Zn (15 MeV/nucleon) + ^{64}Ni. The total experimental data set is shown by full black points, while runs 22-34, 41-61, and 64-69 are represented by full orange, green, and red points, respectively. The vertical dashed (green) line shows the grazing angle.

C.1.1.3 Charge Exchange Channels

In Fig. C.6, the p/A distributions of charge exchange channels, specifically -1p,+1n (^{70}Cu) and +1p,-1n (^{70}Ga), are presented. Some key observations can be made in both cases. In panel (a), representing ^{70}Cu, Runs 22-34 and 41-61 exclusively account for the dissipative region, while the QE peak is described only by Runs 64-69. On the other hand, in panel (b), corresponding to ^{70}Ga, Runs 22-34 and 41-61 contribute to the totality of the distribution, whereas Runs 64-69 are again confined to the QE peak. The angular distributions in Fig. C.7 follow the same general trend observed in the previous cases.

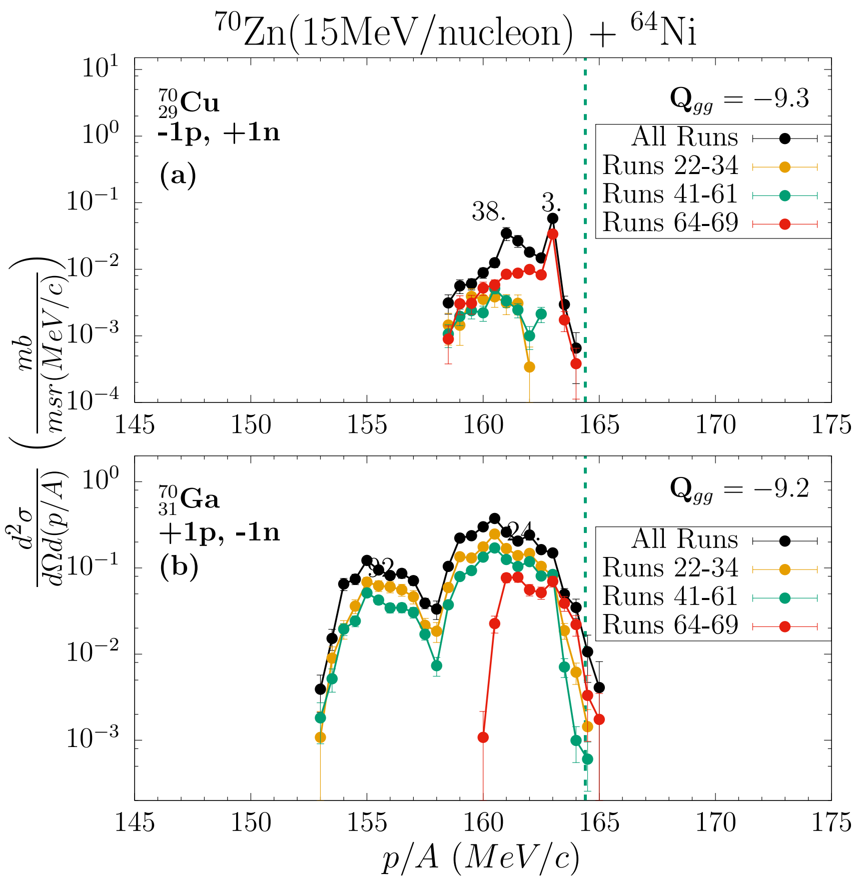

Figure C.6: Momentum per nucleon distributions of ejectiles from charge exchange channels of the reaction ^{70}Zn (15 MeV/nucleon) + ^{64}Ni. The total experimental data set is shown by full black points, while runs 22-34, 41-61, and 64-69 are represented by full orange, green, and red points, respectively. The vertical dashed (green) line is the p/A of the projectile.

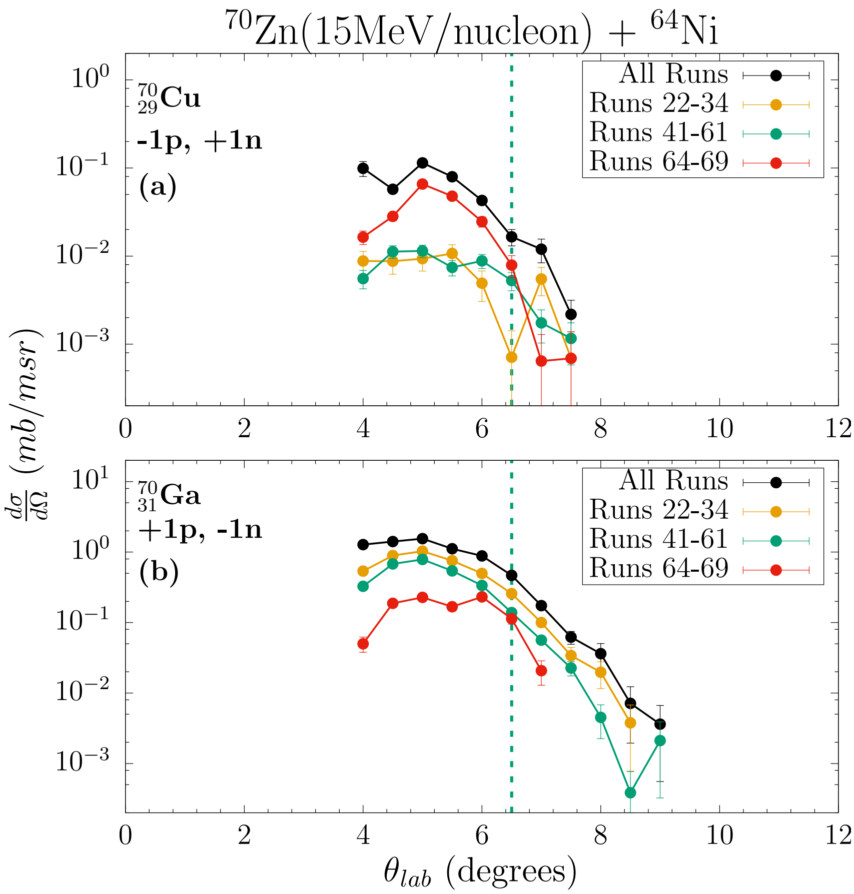

Figure C.7: Angular distributions of ejectiles from charge exchange channels of the reaction ^{70}Zn (15 MeV/nucleon) + ^{64}Ni. The total experimental data set is shown by full black points, while runs 22-34, 41-61, and 64-69 are represented by full orange, green, and red points, respectively. The vertical dashed (green) line shows the grazing angle.

C.2 Summary

In this appendix, we studied the contribution of individual runs in the p/A and angular distributions of several representative channels. We noted that runs 64-69 in the run set played a crucial role in enhancing the quasielastic (QE) peak of the p/A distributions. This contribution is particularly significant, as it can provide valuable information for the direct reaction mechanisms as discussed in Chapter 5 of this thesis.

References

[1] M. Thoennessen, *2023 update of the discoveries of nuclides* , Int. J. Mod. Phys. E **33**, 03n04 (2024).

[2] S. Heinz, H.M. Devaraja, *Nucleosynthesis in multinucleon transfer reactions,* Eur. Phys. J. A **58**:114 (2022).

[3] G. G. Adamian, N. V. Antonenko, A. Diaz-Torees, S.Heinz, *How to extend the chart of nuclides?*, Eur. Phys. J. A **56**:47 (2020).

[4] Chun-Wang Ma, Hui-Ling Wei, Xing-Quan Liu, Jun Su, Hua Zheng, Wei-Ping Lin et al., *Nuclear fragments in projectile fragmentation reactions*, Progress in Particle and Nuclear Physics **121**, 103911 (2021).

[5] Y. Blumenfeld, T. Nilsson, P.V. Duppen, *Facilities and methods for radioactive ion beam production*, Phys. Scr. T **152**, 014203 (2013).

[6] J. Erler, N. Birge, M. Kortelainen, W. Nazarewicz, E. Olsen, A. M. Perhac et al., *The limits of nuclear landscape*, Nature **486**, 509 (2011).

[7] S. R. Stroberg, J. D. Holt, A. Schwenk, J. Simonis, *Ab Initio Limits of Atomic Nuclei*, Phys. Rev. Lett. **126**, 022501 (2021).

[8] J. J. Cowan, C. Sneden, J. E. Lawler, A. Aprahamian, M. Wiescher, K. Langanke, G. Martinez-Pinedo, and F. K. Thielemann, Origin of the heaviest elements: The rapid neutron-capture process. Rev. Mod. Phys. **93**, 015002 (2021).

[9] P. Seeger, W. Fowler, D. Clayton, *Nucleosynthesis of Heavy Elements by Neutron Capture*, The Astrophysical Journal Supplement Series **11**, 121 (1965).

[10] M. Arnould, S. Goriely, *Astronuclear Physics: A Tale of the Atomic Nuclei in the Skies*, Prog. Part. Nucl. Phys. **112**, 103766 (2020).

[11] K. Langanke, M. Wiescher, *Nuclear Reactions and Stellar Processes*, Rep. Prog. Phys. **64**, 1657 (2001).

[12] M.M. Kasliwal, E. Nakar, L.P. Singer, D.L. Kaplan, D.O. Cook, A. Van Sistine et al., *Illuminating gravitational waves: A concordant picture of photons from a neutron star merger*, Science **358**, 1559–1565 (2017).

[13] M.W. Coughlin, T. Dietrich, Z. Doctor, D. Kasen, S. Coughlin, A. Jerkstrand et al., *Constraints on the neutron star equation of state from AT2017gfo using radiative transfer simulations* Mon. Not. R. Astron. Soc. **480**, 3871–3878 (2018).

[14] E. Margaret Burbidge, G. R. Burbidge, William A. Fowler, and F. Hoyle, *Synthesis of the Elements in Stars*, Rev. Mod. Phys. **29**, 547 (1957).

[15] K. Langanke, *Nuclear data - an essential tool in nuclear astrophysics*, EPJ Web Conf. **284**, 03001 (2023).

[16] D. Montanari, E. Farnea, S. Leoni, G. Pollarolo, L. Corradi, G. Benzoni et al., *Response function of the magnetic spectrometer PRISMA*, Eur. Phys. J. A **47**, 4 (2011).

[17] T. Mijatovic, S. Szilner, L. Corradi, D. Montanari, G. Pollarolo, E. Fioretto et al., *Study of the cross section determination with the PRISMA spectrometer: The* ^{40}*Ar* + ^{208}*Pb case*, Eur. Phys. J. A **52**, 113 (2016).

[18] H. Savajols, *VAMOS : a VAriable MOde high acceptance Spectrometer for identifying reaction products induced by SPIRAL beams*, Nucl. Instrum. Methods B **204**, 146 (2003).

[19] S. Pullanhiotan, M. Rejmund, A. Navin, W. Mittig, S. Bhattacharyya, *Performance of VAMOS for reactions near the Coulomb barrier*, Nucl. Instrum. Methods A **593**, 343 (2008).

[20] M. Rejmund, B. Lecornu, A. Navin, C. Schmitt, S. Damoy, O. Delaune et al., *Performance of the improved larger acceptance spectrometer: VAMOS++*, Nucl. Instrum. Methods A **646**, 184 (2011).

[21] F. Cappuzzello, C. Agodi, D. Carbone, M. Cavallaro, *The MAGNEX spectrometer: Results and perspectives*, Eur. Phys. J. A **52**, 167 (2016).

[22] F. Cappuzzello, C. Agodi, M. Cavallaro, D. Carbone, S. Tudisco, D. Lo Presti et al., *The NUMEN project: NUclear Matrix Elements for Neutrinoless double beta decay*, Eur. Phys. J. A **54**, 72 (2018).

[23] F. Cappuzzello, H. Lenske, M. Cavallaro, C. Agodi, N. Auerbach, J. I. Bellone et al., *Shedding light on nuclear aspects of neutrinoless double beta decay by heavy-ion double charge exchange reactions,* Prog. Part. Nucl. Phys. 128, 103999 (2023).

[24] F. Nowacki, A. Obertelli, A. Poves, *The neutron-rich edge of the nuclear landscape: Experiment and theory*, Prog. Part. Nucl. Phys. **120**, 103866 (2021).

[25] L. Corradi, G. Pollarolo, and S. Szilner, *Multinucleon transfer processes in heavy-ion reactions* J. Phys. G: Nucl. Part. Phys. **36**, 113101 (2009).

[26] L. Corradi, S. Szilner, G. Pollarolo, D. Montanari, E. Fioretto, A. M. Stefanini et al., *Multinucleon transfer reactions: Present status and perspectives*, Nucl. Instrum. Methods B **317**, 743 (2013).

[27] J. Diklic, S. Szilner, L. Corradi, T. Mijatovic, G. Pollarolo, P. Colovic et al., *Transfer reactions in ^{206}Pb+^{118}Sn: From quasielastic to deep-inelastic processes*, Phys. Rev. C **107**, 014619 (2023).

[28] R. M. Perez-Vidal, F. Galtarossa, T. Mijatovic, S. Szilner, I. Zanon, D. Brugnara et al., *Nuclear structure advancements with multinucleon transfer reactions*, Eur. Phys. J. A **59**, 114 (2023).

[29] V. V. Saiko and V. Karpov, *Production of neutron-enriched isotopes along magic number $N = 126$ by multinucleon transfer reactions with radioactive-ion beams*, Phys. Rev. C **109**, 064607 (2024).

[30] Y. Shimizu, T. Kubo, T. Sumikama, N. Fukuda, H. Takeda, H. Suzuki et al., *Production of new neutron-rich isotopes near the $N = 60$ isotones ^{92}Ge and ^{93}As by in-flight fission of a 345 MeV/nucleon ^{238}U beam*, Phys. Rev. C **109**, 044313 (2024).

[31] Yu-Hai Zhang, Jing-Jing Li, Cheng Li, Ming-Hao Zhang, Ying Zou, and Feng-Shou Zhang, *Microscopic study of the production of neutron-rich isotopes near*

N = 126 in the multinucleon transfer reactions ^{78,82,86}*Kr* + ^{208}*Pb*, Phys. Rev. C **109**, 064617 (2024).

[32] T. Mijatovic, S. Szilner, L. Corradi, D. Montanari, G. Pollarolo, E. Fioretto et al., *Multinucleon transfer reactions in the* ^{40}*Ar*+^{208}*Pb system*, Phys. Rev. C **94**, 064616 (2016).

[33] F. Galtarossa, L. Corradi, S. Szilner, E. Fioretto, G. Pollarolo, T. Mijatovic et al., *Mass correlation between light and heavy reaction products in multinucleon transfer* ^{197}*Au*+^{130}*Te collisions*, Phys. Rev. C **97**, 054606 (2018).

[34] D. Montanari, L. Corradi, S. Szilner, G. Pollarolo, E. Fioretto, G. Montagnoli et al., *Neutron Pair Transfer in* ^{60}*Ni*+^{116}*Sn Far below the Coulomb Barrier*, Phys Rev. Lett. **113**, 052501 (2014).

[35] L. Corradi, S. Szilner, G. Pollarolo, T. Mijatovic, D. Montanari, E. Fioretto et al., *Evidence of proton-proton correlations in the* ^{116}*Sn*+^{60}*Ni transfer reactions*, Phys. Lett. B **834**, 137477 (2022).

[36] W. Loveland, D.J. Morrissey, G.T. Seaborg, *Modern Nuclear Chemistry*, Wiley & Sons (2006).

[37] G.A Souliotis, *Study of Projectile Fragmentation Reactions at Intermediate Energies*, PhD Thesis, Department of Chemistry, Michigan State University (1992).

[38] V.V. Volkov, *Deep inelastic transfer reactions — The new type of reactions between complex nuclei*, Phys. Rep. **44**, 93 (1978).

[39] R. Bass, *Nuclear Reactions with Heavy Ions*, (Springer, Berlin, 1980).

[40] J. Wilczynski, *Nuclear molecules and nuclear friction* Phys. Lett. B **47**, 484 (1973).

[41] G. A. Souliotis, M. Veselsky, G. Chubarian, L. Trache, A. Keksis, E. Martin, A. Ruangma, E. Winchester, S.J. Yennello, *Enhanced Production of Neutron Rich Rare Isotopes in the reaction of 25 MeV/nucleon* ^{86}*Kr on* ^{64}*Ni*, Phys. Lett. B **543**, 163 (2002).

[42] G. A. Souliotis, M. Veselsky, G. Chubarian, L. Trache, A. Keksis, E. Martin, D. V. Shetty, S. J. Yennello, *Enhanced Production of Neutron-Rich Rare Isotopes in Peripheral Collisions at Fermi Energies*, Phys. Rev. Lett. **91**, 022701 (2003).

[43] G. A. Souliotis, M. Veselsky, G. Chubarian, S. J. Yennello, *Production and separation of neutron-rich rare isotopes around and below the Fermi energy*, Nucl. Instrum. Methods B **204**, 166 (2003).

[44] G. A. Souliotis, A. L. Keksis, B. C. Stein, M. Veselsky, M. Jandel, D. V. Shetty, S. N. Soisson, S. Wuenschel, S. J. Yennello, *Neutron-rich rare isotope production in the Fermi energy domain and application to the Texas A&M radioactive beam upgrade*, Nucl. Instrum. Methods B **266**, 4692 (2008).

[45] G. A. Souliotis, M. Veselsky, S. Galanopoulos, M. Jandel, Z. Kohley, L. W. May, D. V. Shetty, B. C. Stein, S. J. Yennello, *Approaching neutron-rich nuclei toward the r-process path in peripheral heavy-ion collisions at 15 MeV/nucleon*, Phys. Rev. C **84**, 064607 (2011).

[46] P. N. Fountas, G. A. Souliotis, M. Veselsky, A. Bonasera, *Systematic study of neutron-rich rare isotope production in peripheral heavy-ion collisions below the Fermi energy*, Phys. Rev. C **90**, 064613 (2014).

[47] O. Fasoula. G. A. Souliotis, S. Koulouris, K. Palli, M. Veselsky, S. Yennello, A. Bonasera, *Study of Multinucleon Transfer Mechanisms in ^{86}Kr-Induced Peripheral Reactions at 15 and 25 MeV/nucleon*, HNPS Advances in Nuclear Physics **28**, 47 (2022).

[48] A. Papageorgiou, G. A. Souliotis, K. Tshoo, S. C. Jeong, B. H. Kang, Y. K. Kwon, M. Veselsky, S. J. Yennello, A. Bonasera, *Neutron-rich rare isotope production with stable and radioactive beams in the mass range A $\sim$ 40–60 at beam energy around 15 MeV/nucleon*, J. Phys. G **45**, 095105 (2018).

[49] K. Palli, G. A. Souliotis, I. Dimitropoulos, T. Depastas, O. Fasoula, S. Koulouris, M. Veselsky, S. J. Yennello, A. Bonasera, *Microscopic Description of Multinucleon Transfer in ^{40}Ar + ^{64}Ni collisions at 15 MeV/nucleon*, EPJ Web of Conferences **252**, 07002 (2021).

[50] R. E. Tribble, R. H. Burch and C. A. Gagliardi *MARS: A momentum achromat recoil spectrometer*, Nucl. Instr. and Meth. A **285**, 441 (1989).

[51] B. Borderie, M. F. Rivet and L. Tassan-Got, *Heavy-ion peripheral collisions in the Fermi energy domain: Fragmentation processes or dissipative collisions?*, Ann. Phys. Fr., **15**, 287 (1990).

[52] G. A. Souliotis, P. N. Fountas, M. Veselsky, S. Galanopoulos, Z. Kohley, A. McIntosh, S. J. Yennello, A. Bonasera, *Isoscaling of heavy projectile residues and N/Z equilibration in peripheral heavy-ion collisions below the Fermi energy*, Phys. Rev. C **90**, 064612 (2014).

[53] G. A. Souliotis, S. Koulouris, F. Cappuzzello, D. Carbone, A. Pakou, C. Agodi et al., *Identification of medium mass (A=60-80) ejectiles from 15 MeV/nucleon peripheral heavy-ion collisions with the MAGNEX large-acceptance spectrometer*, Nucl. Instr. and Meth. A **1031**, 166588 (2022).

[54] H. Sohlbach, H. Freiesleben, W. F. W. Schneider, D. Schull, B. Kohlmeyer, M. Marinescu et al., *Inelastic excitation and nucleon transfer in quasielastic reactions between ^{86}Kr and ^{208}Pb at 18.2 MeV/u beam energy*, Z. Phys. A **328**, 205 (1987).

[55] H. Sohlbach, H. Freiesleben, W. F. W. Schneider, D. Schull, P. Braun-Munzinger, B. Kohlmeyer et al., *Excitation energy sharing in ^{86}Kr-induced quasielastic reactions on ^{197}Au and ^{208}Pb between 10 and 18.2 MeV/u*, Nucl. Phys. A **467**, 349 (1987).

[56] H. Sohlbach, H. Freiesleben, P. Braun-Munzinger, W. F. W. Schneider, D. Schull, B. Kohlmeyer et al., *Channel-dependent sharing of the excitation energy in quasielastic reactions between ^{208}Pb + ^{86}Kr*, Phys. Lett. B **153**, 386 (1985).

[57] G. Charpak, F. Sauli, *Multiwire proportional chambers and drift chambers*, Nucl. Instrum. Methods **62**, 235 (1968).

[58] K. Makino, M. Berz, *COSY INFINITY Version 9*, Nucl. Instrum. Methods A **558**, 346 (2006).

[59] D.C. Carey, *The Optics of Charged Particle Beams*, Harwood Academic Publishers (1987).

[60] A. Lazzaro, F. Cappuzzello, A. Cunsolo, M. Cavallaro, A. Foti, S.E.A. Orrigo, M.R.D. Rodrigues, J.S. Winfield, M. Berz, *Field reconstruction in large aperture quadrupole magnets*, Nucl. Instrum. Methods A **602**, 494 (2009).

[61] R. Degenhardt, M. Bertz, *High-accuracy field description of particle spectrographs*, Nucl. Instrum. Methods A **427**, 151 (1999).

[62] M. Cavallaro, F. Cappuzzello, D. Carbone, A. Cunsolo, A. Foti, R. Linares, *Transport efficiency in large acceptance spectrometers*, Nucl. Instrum. Methods A **637**, 77-87 (2011).

[63] F.Cappuzzello, L. Acosta, C. Agodi, I. Bostozun, G.A. Brischetto, S. Calabrese et al., *The NUMEN Project: An Update of the Facility Toward the Future Experimental Campaigns*, Front. Astron. Space Sci. **8**, 668587 (2021).

[64] A. Cunsolo, F. Cappuzzello, A. Foti, A. Lazzaro, A. L. Melita, C. Nociforo et al., *Technique for 1^{st} order design of a large-acceptance magnetic spectrometer*, Nucl. Instrum. Methods A **481**, 48 (2002).

[65] A. Cunsolo, F. Cappuzzello, A. Foti, A. Lazzaro, A. L. Melita, C. Nociforo et al., *Ion optics for large-acceptance magnetic spectrometers: application to the MAGNEX spectrometer*, Nucl. Instrum. Methods A **484**, 56 (2002).

[66] F. Cappuzzello, M. Cavallaro, A. Cunsolo, A. Foti, D. Carbone, S. E. A. Orrigo, et al., *A particle identification technique for large acceptance spectrometers*, Nucl. Instrum. Methods A **621**, 419 (2010).

[67] F. Cappuzzello, D. Carbone, M. Cavallaro, *Measuring the ions momentum vector with a large acceptance magnetic spectrometer*, Nucl. Instrum. Methods A **638**, 74 (2011).

[68] D. Torresi, O. Sgouros, V. Soukeras, M. Cavallaro, F. Cappuzzello, D. Carbone et al., *An upgraded focal plane detector for the MAGNEX spectrometer*, Nucl. Instrum. Methods A **989**, 164918 (2021).

[69] D. Carbone, F. Cappuzzello, M. Cavallaro, *Universal algorithm for the analysis of charge distributions in segmented electrodes of gas detectors*, Eur. Phys. J. A **48**:60 (2020).

[70] E. Gatti, G. Padovini, V. Radeka, *Signal evaluation in multielectrode radiation detectors by means of a time dependent weighting vector*, Nucl. Instrum. Methods in Physics Research **989**, 651-653 (1982).

[71] C. Agodi, A.D. Russo, L. Calabretta, G. D'Agostino, F. Cappuzzello, M. Cavallaro et al., *The NUMEN Project: Toward New Experiments with High-Intensity Beams*, Universe **7**, 72 (2021).

[72] M. Cavallaro, C. Agodi, G. A. Brischetto, S. Calabrese, F. Cappuzzello, D. Carbone et al., *The MAGNEX magnetic spectrometer for double charge exchange reactions*, Nucl. Instr. and Meth. B **463**, 334 (2020).

[73] F. Hubert, R. Bimbot, H. Gauvin, *RANGE AND STOPPING-POWER TABLES FOR 2.5-500 MeV/NUCLEON HEAVY IONS IN SOLIDS* At. Data Nucl. Data Tables **46** 1 (1990).

[74] A. Leon, S. Melki, D. Lisfi, J.P. Grandin, P Jardin, M.G. Suraud, A. Cassimi, *Charge State Distributions of Swift Heavy Ions Behind Various Solid Targets (36 $\leq Zp \leq$ 92, 18 MeV/u $\leq E \leq$ 44 MeV/u)*, At. Data Nucl. Data Tables **69**, 217 (1998).

[75] E. Baron, M. Bajard, and Ch. Ricaud, *Charge exchange of very heavy ions in carbon foils and in the residual gas of GANIL cyclotrons*, Nucl. Instr. and Meth. A **328**, 177-182 (1993).

[76] L. Tassan-Got and C. Stephan, *Deep inelastic transfers: a way to dissipate energy and angular momentum for reactions in the Fermi energy domain*, Nucl. Phys. A **524**, 121 (1991).

[77] M. Veselsky, G.A. Souliotis, *Production of Exotic Nuclei in Peripheral Nucleus-Nucleus Collisions below 10 AMeV*, Nucl. Phys. A **872**, 1-12 (2011).

[78] H. Hofmann, P. Siemens, *On the dynamics of statistical fluctuations in heavy ion collisions*, Nucl. Phys. A **275**, 464-486 (1977).

[79] P.J. Johansen, P.J. Siemens, A.S. Jensen, H. Hofmann, *Forces between heavy nuclei in the independent-particle model*, Nucl. Phys. A **288**, 152-188 (1977).

[80] F. Fucito, *A proposal for Monte Carlo simulations of fermionic systems*, Nucl. Phys. B **130**, 269-377 (1981).

[81] J. Randrup, R. Vandenbosch *Pre-equilibrium Neutron Emission in the Nucleon Exchange Transport Model*, Nucl. Phys. A **474**, 371-405 (1987).

[82] M. Papa, T. Maruyama, A. Bonasera, *Constraint molecular dynamics approach to fermionic systems*, Phys. Rev. C **64**, 024612 (2001).

[83] M. Papa, G. Giuliani, A. Bonasera, *Constrained molecular dynamics II: A N-body approach to nuclear systems*, J. Comput. Phys. **208**, 403 (2005).

[84] J. Aichelin, *“Quantum” molecular dynamics—a dynamical microscopic n-body approach to investigate fragment formation and the nuclear equation of state in heavy ion collisions,* Phys. Rep. **202**, 233 (1991).

[85] T. Depastas, G.A. Souliotis , K. Palli, A. Bonasera, H. Zheng, *A Constrained Molecular Dynamics (CoMD) study of nuclear near-ground-state properties*, EPJ Web of Conferences **252**, 07003 (2021).

[86] R. J. Charity, M. A. McMahan, G. J. Wozniak, R. J. McDonald, L. G. Moretto, D. G. Sarantites et al., *Systematics of complex fragment emission in niobium-induced reactions*, Nucl. Phys. A **483**, 371 (1988).

[87] R. J. Charity, *N-Z distributions of secondary fragments and the evaporation attractor line,* Phys. Rev. C **58**, 1073 (1998).

[88] V. Zagrebaev, W. Greiner, *Unified consideration of deep inelastic, quasi-fission and fusion–fission phenomena,* J. Phys. G: Nucl. Part. Phys. **31**, 825 (2005).

[89] V. Zagrebaev, W. Greiner, *Low-energy collisions of heavy nuclei: dynamics of sticking, mass transfer and fusion*, J. Phys. G: Nucl. Part. Phys. **34**, 1 (2007).

[90] J.A. Scarpaci, *Multiphonon states built with giant resonances*, Nucl. Phys. A **731**, 175 (2004).

[91] M. Papa, A. Bonanno, F. Amorini, A. Bonasera, G. Cardella, A. Di Pietro et al., *Coherent and incoherent giant dipole resonance γ-ray emission induced by heavy ion collisions: Study of the ^{40}Ca+^{48}Ca system by means of the constrained molecular dynamics model*, Phys. Rev. C **68**, 034606 (2003).

[92] C. Parascandolo D. Pierroutsakou, R. Alba, A. Del Zoppo, C. Maiolino, D. Santonocito, C. Agodi, V. Baran, A. Boiano et al., *Evidence of dynamical dipole excitation in the fusion-evaporation of the ^{40}Ca + ^{152}Sm heavy system*, Phys. Rev. C **93**, 044619 (2016).

[93] S. Burrello, M. Colonna, H. Zheng, *The Symmetry Energy of the Nuclear EoS: A Study of Collective Motion and Low-Energy Reaction Dynamics in Semiclassical Approaches*, Frontiers in Physics **7**, 53 (2019).

[94] P. Finocchiaro, L. Acosta, C. Agodi, C. Altana, P. Amador-Valenzuela, I. Bostozun et al., *The NUMEN Heavy Ion Multidetector for a Complementary Approach to the Neutrinoless Double Beta Decay*, Universe **6**, 129 (2020).

[95] D. Calvo, I. Ciraldo, C. Agodi, F. Cappuzzello, M. Cavallaro et al, *Present outcome from the NUMEN R&D phase*, Nucl. Inst. and Methods in Phys. Res. A **1041**, 167336 (2022).

[96] W.W. Wilcke, J.R. Birkelund, H.J. Wollersheim, A.D. Hoover, J.R. Huizenga, W.U. Schröder, and L.E. Tubb, *Reaction Parameters for heavy-ion collisions*, At. Data Nucl. Data Tables **25**, 389 (1980).

[97] G.A. Souliotis, D.J. Morrissey, N.A. Orr, B.M. Sherrill, J.A. Winger, *0° measurements of momentum distributions of projectile-like fragments*, Phys. Rev. C **46**, 1383 (1992).

[98] R. Pfaff, D.J. Morrissey, M. Fauerbach, M. Hellström, J.H. Kelley, R.A. Kryger, B.M. Sherrill, M. Steiner, J.S. Winfield et al., *Projectilelike fragment momentum distributions from ^{86}Kr+Al at 70 MeV/nucleon*, Phys. Rev. C **51**, 1348 (1995).

[99] H. Lenske, F. Cappuzzello, M. Cavallaro, M. Colonna, *Heavy ion charge exchange reactions as probes for nuclear β-decay*, Progress in Particle and Nuclear Physics **109**, 103716 (2019).

[100] M.T. Magda, A. Pop, A. Sandulescu, *A model for large cluster transfer in reactions leading to heavy actinides*, J. Phys. G Nucl. Phys. **13**, 127 (1987).

[101] C. Agodi, G. Giuliani, F. Cappuzzello, A. Bonasera, D. Carbone, M. Cavallaro, A. Foti, R. Linares, and G. Santagati, *Analysis of pairing correlations in neutron transfer reactions and comparison to the constrained molecular dynamics model*, Phys. Rev. C **97**, 034616 (2018).

[102] A. Bonaccorso, *Direct reaction theories for exotic nuclei: An introduction via semi-classical methods*, Progress in Particle and Nuclear Physics **101**, 1 (2018).

[103] S. Koulouris, G. A. Souliotis, F. Cappuzzello, D. Carbone, A. Pakou, C. Agodi et al., *Measurements of projectile fragments from ^{70}Zn + ^{64}Ni collisions with the MAGNEX spectrometer at INFN-LNS*, HNPS Adv. Nucl. Phys. **28**, 42 (2022).

[104] S. Koulouris, G. A. Souliotis, F. Cappuzzello, D. Carbone, A. Pakou, C. Agodi et al., *Multinucleon transfer channels from* ^{70}*Zn (15 MeV/nucleon)* + ^{64}*Ni collisions*, Phys. Rev. C **108**, 044612 (2023).

[105] S. Szilner, L. Corradi, J. Diklić, T. Mijatović, F. Galtarossa, G. Pollarolo, E. Fioretto, A. Goasduff, G. Montagnoli et al., *Quest for Cooper Pair Transfer in Heavy-Ion Reactions: The* ^{206}*Pb*+^{118}*Sn Case*, Phys. Rev. Lett. **133**, 202501 (2024).

[106] I. J. Thompson, *Coupled reaction channels calculations in nuclear physics*, Comput. Phys. Rep. **7**, 167 (1988).

[107] M.H. MacFarlane, S.C. Pieper, *Ptolemy: a program for heavy-ion direct-reaction calculations*, Argonne National Laboratory report no. ANL-76-11 (1978).